# —5—

# *Doubly Rotated Thickness Mode*

# *Plate Vibrators*

ARTHUR BALLATO

*U.S. Army Electronics Technology & Devices Laboratory*
*Fort Monmouth, New Jersey 07703*

## I. Introduction

This chapter deals with the properties of piezoelectric plate vibrators having
laterally unbounded, parallel faces that have arbitrary inclinations to the

natural axes of the crystals from which they are fashioned. The plate motions under discussion are the simple thickness modes; these do not depend on lateral coordinates, making the situation inherently one-dimensional. With the thickness coordinate the only direction of interest, plate orientation is specified uniquely by two angles, so the crystal cuts are spoken of as being "doubly rotated."

The use of such cuts is not new, nor is any practical problem, strictly speaking, one-dimensional. Why, then, an article on the topic at this time? There are two major reasons. Recent discovery of compensation of nonlinear effects in quartz offers the promise of new advances in the area of high precision frequency control, while the advent of new, high coupling, zero temperature coefficient materials is seen as providing exciting prospects for bulk wave filter and transducer technology as well as important applications in surface acoustic wave devices. In both cases, doubly rotated cuts are expected to be widely utilized in the future. Moreover, several aspects of the problems associated with this more general type of vibrator, such as the simultaneous excitation of two or three modes and their interaction have meanwhile been clarified. These have made possible a coherent account of the properties of these cuts, better approximations, and an indication of areas for further investigation and improvement, so that a survey of the situation now is particularly pertinent. As for the limitation to thickness modes, this case has the estimable virtue of possessing an exact solution, even for plates devoid of crystal symmetry, while retaining those features most relevant to the characterization of practical devices.

Singly and doubly rotated plates are shown in Fig. 1 in relation to the crystallographic axes $X$, $Y$, $Z$. In standard notation (Anonymous, 1949) the
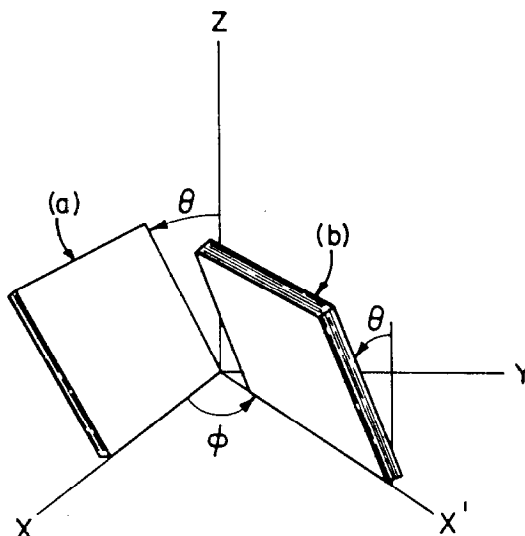


FIG. 1. Conventions for specifying plate orientations with respect to crystal axes $X$, $Y$, $Z$. (a) Singly rotated plate. (b) Doubly rotated plate.

singly rotated Y cut shown is described as $(YXl)\theta$; the AT and BT cuts of quartz are representative (Mason, 1964). Doubly rotated quartz cuts $(YXwl)\varphi/\theta$ were investigated by Bokovoy and Baldwin (1935) starting from the singly rotated X cut, and this led to their discovery of the V-cut family. Improvements in frequency–temperature behavior motivated this early work on quartz plates, and remains a continued concern for most modern applications. Having two orientation angles available permits satisfaction of additional requirements simultaneously with temperature coefficient constraints, as will become apparent in Sections IV and V. We shall lead up to these considerations by describing first the propagation of acoustic plane waves in piezoelectric crystals and the solution to the general unbounded plate problem.

## II. Waves and Vibrations in Piezoelectric Media

One hundred years ago, Elwin Christoffel (1877) gave a formalism for treating acoustic plane wave propagation in arbitrarily anisotropic, linear media. Lawson (1941) extended it to include piezoelectricity, finding correct expressions for the three stiffened phase velocities. Subsequent applications of the theory to thickness vibrations of plates proved rigorous only for particular cases involving excitation of a single mode until Tiersten (1963) produced the exact solution that showed the three modes to be piezoelectrically coupled by the plate surfaces. The exact analysis also disclosed in retrospect that various quantities required for discussing plate vibrations, such as the correct piezoelectric coupling factor driving each mode, could be obtained easily without considering any boundaries.

This section outlines the Christoffel method and its application to simple thickness modes of plates. In keeping with the convention seen in Fig. 1, a right-handed orthogonal coordinate system is taken to undergo two successive rotations from the crystallographic axes $X_i$ ($= X, Y, Z$): a first rotation about $X_3$ by angle $\varphi$, followed by a rotation about $X'_1$ by angle $\theta$. Plane waves are then taken to propagate along $X''_2$, which will subsequently become the thickness axis of our plate.

### A. Plane Acoustic Waves in Piezoelectric Crystals

In the following a subscripted index preceded by a comma denotes differentiation with respect to the coordinate having that subscript, and twice-repeated indices denote summation. A time harmonic dependence $\exp(+j\omega t)$ is assumed. The pertinent sets of equations, referred to the crystallographic axes $X_i$, that are to be solved consist of the stress equations of motion

$$T_{ij,i} = -\rho\omega^2 u_j;\tag{1}$$

the definition of mechanical strain

$$S_{kl} = \tfrac{1}{2}(u_{k,l} + u_{l,k});$$

(2)

the Maxwell divergence relation

$$D_{i,i} = 0;$$

(3)

the quasi-static electric field–potential equation

$$E_n = -\Phi_{,n};$$

(4)

and the linear piezoelectric constitutive relations characterizing the medium

$$T_{ij} = c^E_{ijkl}S_{kl} - e_{nij}E_n,$$

(5)

$$D_i = e_{ikl}S_{kl} + \varepsilon^S_{in}E_n.$$

(6)

In these equations $T_{ij}$, $u_j$, $S_{kl}$, $D_i$, and $E_n$ are the components of mechanical stress, displacement and strain, electric displacement and field, respectively; $\rho$ and $\Phi$ are the mass density and electric potential. The material parameters $c^E_{ijkl}$, $e_{nij}$, and $\varepsilon^S_{in}$ are the elastic stiffnesses at constant electric field, the piezoelectric stress constants, and the dielectric permittivities at constant strain. All indices have the range 1, 2, 3.

Equations (2) and (4) are used in Eqs. (5) and (6) to eliminate $S_{kl}$ and $E_n$. The resulting relations are substituted into Eqs. (1) and (3) to yield four equations in the displacements $u_j$ and the potential. These are referred to the direction of propagation $X''_2$ by making use of the transformation

$$X''_i = \alpha_{ij}X_j.$$

(7)

With the abbreviations $\zeta$ for $X''_2$ and $\alpha_i$ for $\alpha_{2i}$ the resulting equations reduce to

$$\Gamma^E_{jk}u_{k,\zeta\zeta} + \Xi_j\Phi_{,\zeta\zeta} = -\rho\omega^2 u_j$$

(8)

$$\Xi_k u_{k,\zeta\zeta} - \varepsilon^S_\zeta\Phi_{,\zeta\zeta} = 0,$$

(9)

where

$$\Gamma^E_{jk} = c^E_{ijkl}\alpha_i\alpha_l$$

(10)

$$\Xi_k = e_{nkl}\alpha_n\alpha_l$$

(11)

$$\varepsilon^S_\zeta = \varepsilon^S_{in}\alpha_i\alpha_n.$$

(12)

Equations (8) and (9) yield

$$\bar{\Gamma}_{jk}u_{k,\zeta\zeta} = -\rho\omega^2 u_j$$

(13)

with

$$\bar{\Gamma}_{jk} = \bar{c}_{ijkl}\alpha_i\alpha_l = \Gamma^E_{jk} + \Xi_j\Xi_k/\varepsilon^S_\zeta,$$

(14)

and an equation in the potential that integrates to

$$\Phi = \Xi_k u_k/\varepsilon_\zeta^S + \mathscr{A}\zeta + \mathscr{B}. \tag{15}$$

In order that Eq. (13) be compatible with the wave equation

$$\bar{c}u_{j,\zeta\zeta} + \rho\omega^2 u_j = 0 \tag{16}$$

requires that

$$(\bar{\Gamma}_{jk} - \bar{c}\delta_{jk})u_{k,\zeta\zeta} = 0. \tag{17}$$

The solution to the eigenvalue equation yields three real roots $\bar{c}_m$, ordered according to the relations

$$\bar{c}_a > \bar{c}_b \geq \bar{c}_c, \tag{18}$$

which determine the piezoelectrically stiffened phase velocities $v_m$:

$$v_m = (\bar{c}_m/\rho)^{1/2}. \tag{19}$$

Corresponding to the roots $\bar{c}_m$ are the orthonormal eigenvectors $\bar{\gamma}_m$ which determine the direction cosines of particle displacement for each mode $m$ with respect to the crystal axes $X_i$.

One may include the phenomenological effects of small loss by considering the viscosity as the imaginary part of the elastic stiffness (Lamb and Richter, 1966):

$$\hat{c}_{ijkl} = c_{ijkl}^E + j\omega\eta_{ijkl}. \tag{20}$$

As long as $\omega\eta_{ijkl} \ll c_{ijkl}^E$ one may avoid the complex eigenvalue problem and compute the effective viscosity for each mode as

$$\eta_m = H_{jk}\bar{\gamma}_{mj}\bar{\gamma}_{mk} \tag{21}$$

using the lossless eigenvectors $\bar{\gamma}_m$ and the analog of Eq. (10)

$$H_{jk} = \eta_{ijkl}\alpha_i\alpha_l. \tag{22}$$

For quartz and other high purity dielectric crystals at room temperature, $\eta_m/\bar{c}_m$ is typically $10^{-14}$ sec, so that Eq. (21) is an excellent approximation into the microwave region.

Applications involving the use of crystal plates as acoustic transducers or as devices for beam steering require a knowledge of the direction of energy flux for an assumed direction of phase progression. The power flow associated with each mode $m$ consists of two parts: a mechanical portion with components

$$P_{iM}^{(m)} = +j\omega T_{ij}^{(m)}u_j^{(m)*} \tag{23}$$

and corresponding electrical portion

$$P_{iE}^{(m)} = -j\omega\Phi^{(m)}D_i^{(m)*}. \tag{24}$$

An asterisk denotes complex conjugation. A forward-traveling wave propagating in direction $\zeta$ produces a displacement field with components proportional to $\bar{\gamma}_{mk}$. Straightforward substitution of this plane wave solution into the pertinent foregoing equations yields the following expressions for the time average power flows due to mode $m$:

$$P_{iM}^{(m)} = P_0 \omega^2 (\tilde{c}_{ijkl} \bar{\gamma}_{mj} \alpha_k \bar{\gamma}_{ml})/v_m \quad \text{(no } m \text{ sum)}, \tag{25}$$

where

$$\tilde{c}_{ijkl} = c_{ijkl}^E + e_{kij} \Xi_l / \varepsilon_\zeta^S, \tag{26}$$

$$P_{iE}^{(m)} = P_0 \omega^2 (\tilde{e}_{ikl} \bar{\gamma}_{mk} \alpha_l (\Xi_j \bar{\gamma}_{mj}) / \varepsilon_\zeta^S)/v_m \quad \text{(no } m \text{ sum)} \tag{27}$$

with

$$\tilde{e}_{ikl} = e_{ikl} - \Xi_k \varepsilon_{il}^S / \varepsilon_\zeta^S. \tag{28}$$

The quantity $P_0$ is an arbitrary amplitude factor. From the sum of Eqs. (25) and (27) the power flow direction is easily obtained.

## B. Simple Thickness Modes of Plates

The simple thickness modes of plates are those for which all variations depend solely on the thickness coordinate—in our instance $\zeta$. We take the plate to be traction-free and driven by potentials $\pm \Phi_0$ on the surfaces $\zeta = \pm h$. These boundary conditions lead to the vanishing of the transformed stresses at the surfaces

$$\alpha_{ij}(\Gamma_{jk} u_{k,\zeta} + \Xi_j \mathscr{A}) = 0 \qquad \text{at} \quad \zeta = \pm h. \tag{29}$$

Together with the potential boundary condition, Eq. (29) determines the constants in Eq. (15) as

$$\mathscr{A} = (\Phi_0/h) \bigg/ \left[ 1 - \sum_m k_m^2 \tan X^{(m)}/X^{(m)} \right], \tag{30}$$

$$\mathscr{B} = 0, \tag{31}$$

where

$$X^{(m)} = \omega h/v_m \tag{32}$$

and

$$k_m^2 = (\bar{\gamma}_{mj} \Xi_j)^2 / \bar{c}_m \varepsilon_\zeta^S \quad \text{(no } m \text{ sum)}. \tag{33}$$

Transformation of Eq. (6) leads to

$$D_\zeta = \Xi_k u_{k,\zeta} - \varepsilon_\zeta^S \Phi_{,\zeta}. \tag{34}$$

With the help of Eq. (15) this reduces to

$$D_\zeta = -\varepsilon_\zeta^S \mathscr{A};$$ (35)

the current density is then just

$$J_\zeta = -j\omega D_\zeta = +j\omega \varepsilon_\zeta^S \mathscr{A}.$$ (36)

For any patch of area $A$, the total current passing through the plate is $AJ_\zeta$, so the input admittance is obtained for this portion by taking the quotient of total current to applied voltage $2\Phi_0$. The static capacitance of the plate section is

$$C_0 = \varepsilon_\zeta^S A/2h,$$ (37)

and the input admittance is found to be (Yamada and Niizeki, 1970)

$$Y_{\text{in}} = j\omega C_0 \Big/ \left[ 1 - \sum_m k_m^2 \frac{\tan X^{(m)}}{X^{(m)}} \right].$$ (38)

The $k_m$ are the piezoelectric coupling factors responsible for excitation of the modes $m$. They are defined in terms of effective piezoelectric constants $e_m$ such that comparison with Eq. (33) leads to the identification

$$e_m = \bar{\gamma}_{mj} \Xi_j.$$ (39)

Therefore, the effective piezoelectric constants and coupling factors are simply obtained from the solution for the infinite medium. In the presence of small loss, Eq. (38) is used with $X^{(m)}$ from Eq. (32) replaced by

$$\hat{X}^{(m)} \simeq X^{(m)}(1 - j\omega\eta_m/2\bar{c}_m).$$ (40)

## III. Critical Plate Frequencies

The piezoelectric plate vibrator has critical frequencies defined by the zeros and poles of the input admittance, Eq. (38). The zeros determine three harmonically related sequences of open-circuit antiresonance frequencies $f_{mA}^{(M)}$. $M$ is an odd integer, the harmonic number, and $N_m = v_m/2$ is the frequency constant for mode $m$:

$$f_{mA}^{(M)} = MN_m/2h.$$ (41)

In the antiresonance case the three thickness modes uncouple from each other. The short-circuit resonance frequencies, obtained from the poles of the admittance, are coupled so that the frequencies cannot be ascribed to any mode, except in a loose manner of speaking. They are denoted $f_R$ and

found from the solution of

$$\sum_m k_m^2 \frac{\tan X^{(m)}}{X^{(m)}} = 1, \tag{42}$$

where

$$X^{(m)} = (\pi/2)(f_R/f_{mA}^{(1)}). \tag{43}$$

Operation of the resonator in an air gap or in series with an external capacitor will have no effect upon the antiresonance frequencies; the resonance frequencies, however, will all be shifted to higher values. If the capacitance value inserted in series is $C_L$, then the modified resonance frequencies are found from Eq. (42) using

$$\hat{k}_m^2 = k_m^2/(1 + C_0/C_L). \tag{44}$$

## A. Two and Three Modes Excited

Doubly rotated crystal plates generally will have all three $k_m$ finite; yet it is still possible in many instances to treat the resonance frequencies as if they were uncoupled. This will be addressed in Section III,B. Here we consider the situation where such a simplification is not justified, and the coupling must be taken into account. The three mode case follows the discussion for two modes, so we start with the two mode case. A practically important instance is the rotated-Y-cut family of cuts in crystal class $3m$, which includes lithium tantalate and lithium niobate, discussed in Section V.

The interplay between two excited modes is seen in the dispersion diagram sketched in Fig. 2. The heavy lines trace branches of the solution of Eq. (42); plotted along the abscissa is the antiresonance frequency ratio

$$\beta = f_{2A}^{(1)}/f_{1A}^{(1)} = v_2/v_1, \tag{45}$$

and the ordinate is normalized frequency

$$\Omega = f/f_{1A}^{(1)}. \tag{46}$$

Bounds are readily established, as will be described below; these permit one to construct any portion of the spectrum rapidly, and from the construction to infer the behavior of the input admittance with driving frequency.

Construction of the terrace plot for two coupled modes proceeds by first finding the lines corresponding to the antiresonances for both modes. For mode one,

$$\Omega_{1A}^{(M)} = M \qquad (M = 1, 3, 5, \ldots). \tag{47}$$

These are a sequence of horizontal lines in the diagram. For mode two,

$$\Omega_{2A}^{(N)} = N\beta \qquad (N = 1, 3, 5, \ldots), \tag{48}$$

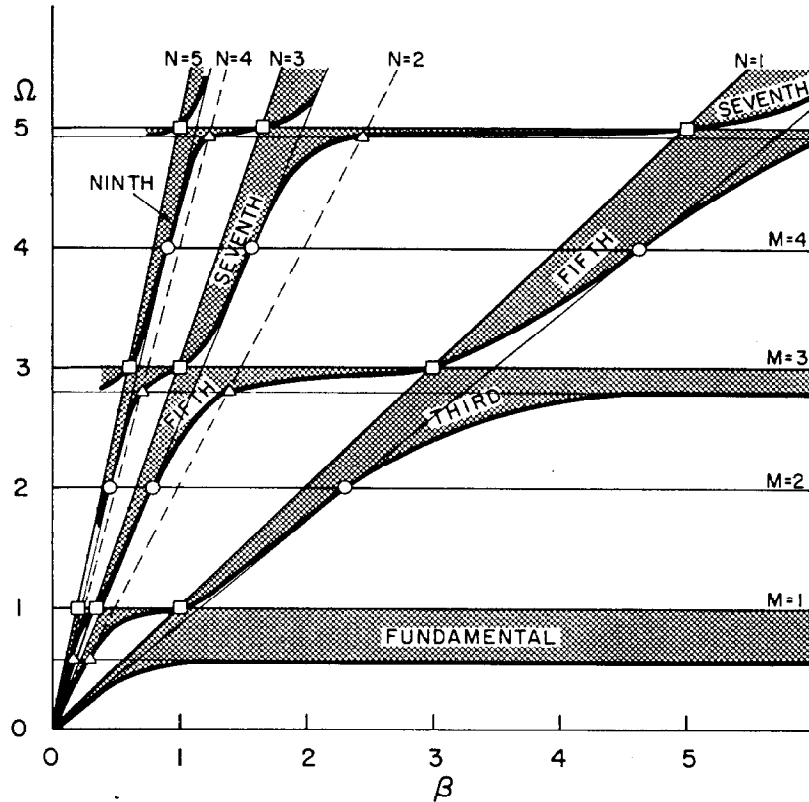giving lines of slope $N$. Next, Eq. (42) is solved twice: once with $k_1$ set to

FIG. 2. Dispersion diagram for a plate vibrator having two piezoelectrically excited modes. Normalized frequency $\Omega$ is plotted against $\beta$, the ratio of fundamental antiresonance frequencies. Regions between succeeding resonances and antiresonances, for fixed $\beta$, are crosshatched.

zero, and then with $k_2 = 0$. (Single mode solutions are discussed by graphical construction in Section III,B.) When $k_2$ is zero, the solution yields for $\Omega_{1R}^{(M)}$ a series of horizontal lines, each below the antiresonance line having the same $M$, but approaching successively closer to the $\Omega_{1A}^{(M)}$ lines with increasing $M$. With $k_1$ set to zero, the solution set consists of lines radiating from the origin. The line for $\Omega_{2R}^{(N)}$ has slope less than $N$, but approaching $N$ for $N$ large.

The next stage in the construction consists in finding where the horizontal $\Omega_{1R}^{(M)}$ lines intersect the solutions of Eq. (42); this is easily shown to occur where the $\Omega_{1R}^{(M)}$ lines cross radial lines of slope $N$, with $N$ even. Similarly, the radial lines for $\Omega_{2R}^{(N)}$ cross the horizontal lines with $M$ even at positions satisfying Eq. (42) also. Solutions of Eq. (42) for $M$ even and $N$ odd are marked in Fig. 2 as circles; those with $M$ odd and $N$ even are marked as triangles.

What happens when one of the two tangent functions in Eq. (42) approaches a pole? In order to balance the equation, the other tangent must obviously also approach a pole in such a fashion as to cancel the effect. This

line of thought may be carried out to show that the resonance frequency loci in the coupled mode case pass through the intersections with $M$ and $N$ odd; these are shown as squares.

Using the circles, triangles, and squares as a lattice of points through which the spectrum must pass, and with the horizontal and radial lines acting as boundaries, the solution branches to Eq. (42) may be found easily. In Fig. 2 the heavy solid lines have been drawn to show $\Omega_R$ for relatively large coupling factors. The shaded areas are those for which the input reactance is positive; i.e., the resonator appears inductive.

For a given crystal cut, the ratio $\beta$ will be a fixed number, usually between 1 and 2. A vertical line on the diagram at this value immediately gives the mode spectrograph sequence of resonances, the pole–zero separation of each resonance, and their location in frequency. In addition, one clearly sees how the resonances move with respect to each other when $\beta$ is changed and how the separations are affected.

When the full set of three $k_m$ is allowed, a three-dimensional construction is required, consisting of two $\beta$ axes

$$\beta_2 = f_{2A}^{(1)}/f_{1A}^{(1)}, \qquad \beta_3 = f_{3A}^{(1)}/f_{1A}^{(1)}, \tag{49}$$

and the $\Omega$ axis of Eq. (46). The result consists of the same sequence of horizontal resonance and antiresonance lines in both $\beta$-$\Omega$ planes as in Fig. 2. The radial resonance lines differ in each plane if $k_2 \neq k_3$. A terraced set of surfaces then describes the complete solution, the construction of which follows in general the procedure outlined here.

## B. Single Mode Excited

Equation (42) reduces to the single mode equation

$$k^2 \tan X = X \tag{50}$$

when two $k_m$ vanish, as occurs for certain combinations of crystal symmetry and plate orientation. An example is the excitation of rotated-Y-cut members in crystal class 32, which includes the AT and BT cuts of quartz. In many instances Eq. (50) may be used as an adequate approximation to Eq. (42) even when two or three $k_m$ are nonzero. The conditions permitting the approximation may be seen for the two mode case from Fig. 2. In those regions of the diagram where the curves lie near the lines $\Omega_{1R}^{(M)}$ or $\Omega_{2R}^{(N)}$, Eq. (50) may be used, including specifically the points marked by circles and triangles, where it is exact. As the coupling factors become smaller, the extent of the applicable regions increases, and conversely. Always to be avoided are the areas where, for $N$ and $M$ odd,

$$M \simeq N\beta; \tag{51}$$

these positions are those marked in Fig. 2 with squares. Here Eq. (50) cannot be used.

A graphical solution to Eq. (50) is shown in Fig. 3. Intersections of the tangent function branches with a straight line of slope $k^{-2}$ define the frequencies of resonance $f_{RO}^{(M)}$; the poles of the tangent function correspond to the antiresonance frequencies $f_{AO}^{(M)}$. The zero subscripts denote the
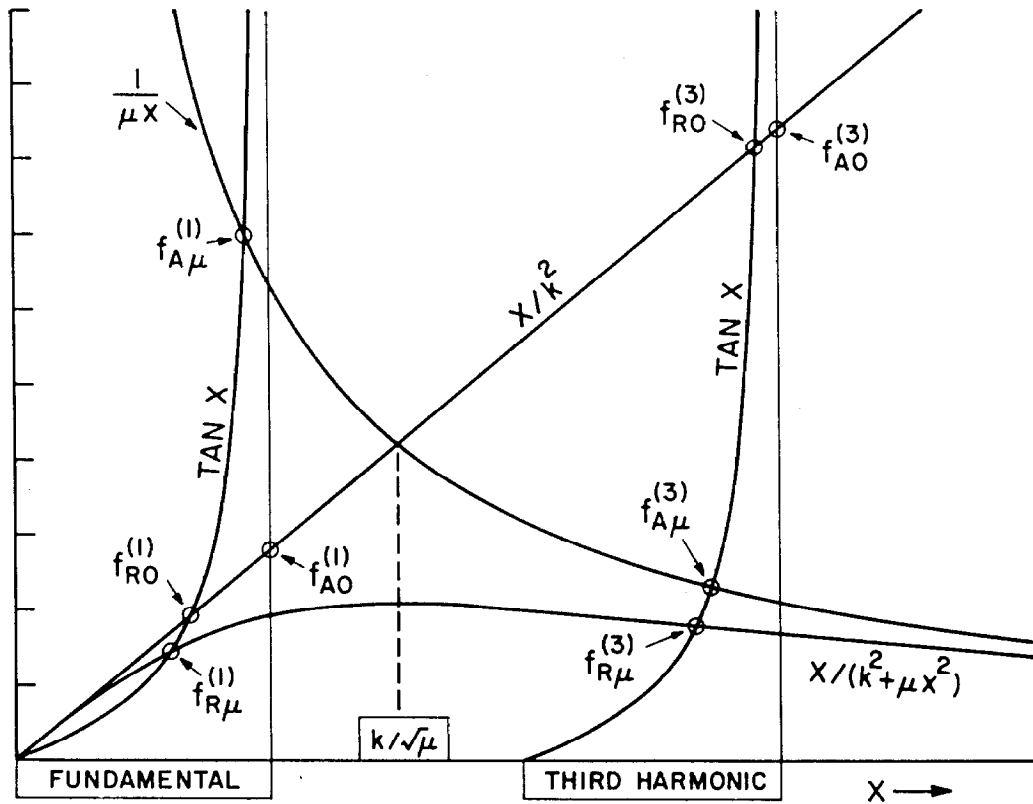


FIG. 3. Graphical solutions to the single mode frequency equations for resonance and antiresonance. The mass loaded case is distinguished by the subscript $\mu$.

absence of mass loading due to the electrode, which is considered in the next subsection. From the construction one sees that the solution consists of a progression of roots successively drawing closer to the harmonically related antiresonances. As the piezoelectric coupling factor $k$ increases, the resonance–antiresonance separation increases at each harmonic. Using Eq. (38), the effective input capacitance of the resonator in the limit of zero frequency is

$$C_{in} = C_0 \left/ \left(1 - \sum_m k_m^2\right)\right. .$$  (52)

Since the stored energy of a capacitor must be positive, the limiting value for the sum of the three $k_m^2$ is unity. If only one $k_m$ is finite, unity becomes its limiting value; such a value would reduce $f_{R0}^{(1)}$ to zero frequency—a clearly unphysical result. Piezoelectric materials, however, are available today with coupling factors in excess of 70%, which means that the fundamental resonance frequency is depressed by the large coupling to values less than three-quarters of the antiresonance frequency. Because of the anharmonic ratios of the frequencies $f_{R0}^{(M)}$ arising from Eq. (50), it is more convenient to characterize many of the plate properties in terms of the antiresonance frequencies $f_{A0}^{(M)}$, and to use $f_{A0}^{(1)}$ as the basis of normalizations.

## C. Effects of Mass Loading on Frequencies

It is current practice to plate metallic electrodes directly on the major surfaces of thickness mode vibrators in order to apply the driving voltage. The electrode coating is assumed here to be devoid of elastic stiffness and to be negligibly thick so that it is represented as a lumped mass $\bar{m}$ per unit area on each plate surface. Replacing Eq. (29) is the stress boundary condition

$$(\Gamma_{jk} u_{k,\zeta} + \Xi_j \mathscr{A}) = \pm \omega^2 \bar{m} u_j \qquad \text{at} \quad \zeta = \pm h. \tag{53}$$

Reduced mass loading is defined as

$$\mu = \bar{m}/\rho h, \tag{54}$$

and in terms of this quantity Eq. (53) leads to a modification of Eq. (38) in the presence of electrode coatings:

$$Y_{\text{in}} = j\omega C_0 \Big/ \left\{ 1 - \sum_m \left[ \left( \frac{k_m^2}{1 - \mu X^{(m)} \tan X^{(m)}} \right) \frac{\tan X^{(m)}}{X^{(m)}} \right] \right\}. \tag{55}$$

As in the traction-free situation, the open-circuit frequencies are uncoupled, but now each is determined from the roots of

$$\mu X^{(m)} \tan X^{(m)} = 1, \tag{56}$$

so they are no longer harmonically related. The resonance frequencies, on the other hand, remain coupled and are found from

$$\sum_m \left[ \left( \frac{k_m^2}{1 - \mu X^{(m)} \tan X^{(m)}} \right) \frac{\tan X^{(m)}}{X^{(m)}} \right] = 1. \tag{57}$$

The discussion of Fig. 2 can be extended to cover mass loading, with two or three $k_m$ nonzero. Bounds are readily constructed from which the depressed spectra are obtained in the general case; we show here the effect on a single mode, which is applicable whenever the conditions of Section III,B hold.

For one mode, Eq. (57) becomes

$$\tan X = X/(k^2 + \mu X^2) \tag{58}$$

with associated graphical solution shown in Fig. 3. Roots of Eq. (58) are designated $f_{R\mu}^{(M)}$; those of Eq. (56), $f_{A\mu}^{(M)}$. In each case $\mu$ has the effect of lowering the critical frequency; but for harmonics where $X < k/\mu^{1/2}$, the piezoelectric contribution to the lowering predominates and the resonance frequencies with and without $\mu$ cluster while the antiresonance frequencies form a separate group. Mass-loading effects predominate for harmonics for which the inequality is reversed, with the mass-loaded frequencies occurring together and the unloaded frequencies forming a separate group.

A more convenient measure of frequency shift due either to mass loading or piezoelectric coupling is frequency displacement, defined by Ballato and Lukaszek (1974) as

$$\delta = M - 2X/\pi. \tag{59}$$

In terms of antiresonance and resonance displacements, Eqs. (56) and (58) respectively become

$$\tan(\delta_A^{(M)}\pi/2) = \mu(M - \delta_A^{(M)})\pi/2, \tag{60}$$

and

$$\tan(\delta_R^{(M)}\pi/2) = \mu(M - \delta_R^{(M)})\pi/2 + 2k^2/\pi(M - \delta_R^{(M)}). \tag{61}$$

Figure 4 shows how $\delta_R^{(M)}$ varies with $M$ and $k$ as a function of $\mu$; for $k = 0$, $\delta_R^{(M)}$ becomes $\delta_A^{(M)}$.

The foregoing has considered some effects of mass loading on plate frequencies when both surfaces are equally loaded. A fact often overlooked in manufacturing is the influence of mass imbalances on the frequency spectrum. When an imbalance exists, even harmonics become excited as well as those that are odd. Although the effect is usually small as far as the magnitudes of the even resonances are concerned, nonlinear coupling via third order elastic constants can produce undesired activity dips at the operating resonance. In addition, the families of anharmonic overtones associated with each thickness mode by virtue of couplings to lateral modes in finite plates all couple to the even modes and their families. The result can be a very complex mode spectrum under the best of circumstances; but when doubly rotated cuts are used with their attendant complexities due to lack of orientational symmetry, any further geometrical asymmetry such as electrode imbalance further worsens the spectrum and decreases the utility of these elements in oscillators and filters.

## D. Approximations for Critical Frequencies

Apart from the antiresonances of traction-free plates, the critical frequencies are determined as roots of transcendental equations. Approxi-
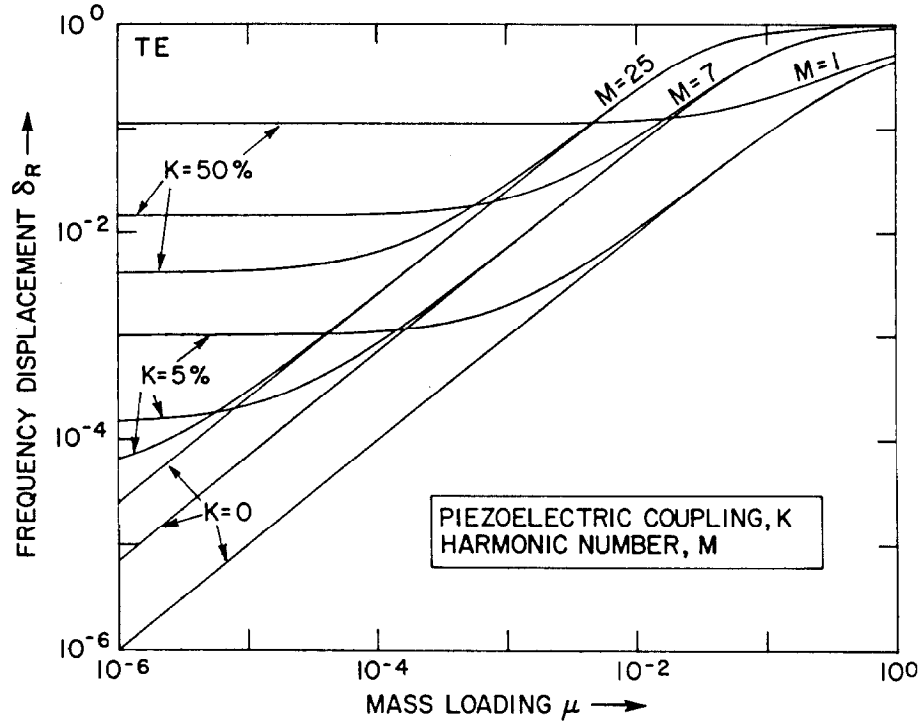
FIG. 4. Single mode frequency displacement versus mass loading for various piezoelectric coupling and harmonic values. Frequency displacement is a normalized measure of departure from antiresonance frequency with zero mass loading.

mate solutions to these equations, adequate for most applications, take the form of simple algebraic functions. Some of these are given here.

In the absence of mass loading, the resonance displacements are approximated by

$$\delta_{RO}^{(M)} \simeq 4k^2/\pi^2 M(1 + 4k^2/\pi^2 M^2) \simeq 4k^2/\pi^2 M. \tag{62}$$

The last form is accurate for all $k$ when $M > 1$, and up to $k = 30\%$ when $M = 1$; the first form is within $1\%$ at the fundamental up to $k = 50\%$.

With mass loading the displacements are found from

$$\delta_{R\mu}^{(M)} \simeq (\delta_{RO}^{(M)} + M\mu)/(1 + M\mu) \tag{63}$$

with $\delta_{RO}^{(M)}$ from Eq. (62). Setting $k = 0$ in Eq. (62) produces the result for $\delta_{A\mu}^{(M)}$ using Eq. (63).

Differences between resonance and antiresonance displacements are found to vary in $\mu$ dependence according to whether $M = 1$ or not. The expressions for the approximations are

$$\delta_{R\mu}^{(1)} - \delta_{A\mu}^{(1)} \simeq (2/\pi)(1 - (1 - k^2)^{1/2})\delta_{RO}^{(1)}/[(2/\pi)(1 - (1 - k^2)^{1/2}) + \delta_{RO}^{(1)}\mu^{1/2}] \tag{64}$$

when $M = 1$, and for $M > 1$,

$$\delta_{R\mu}^{(M)} - \delta_{A\mu}^{(M)} \simeq (2/\pi)^4 k^2 \delta_{RO}^{(M)}/[(2/\pi)^4 k^2 + (M - 1)^3 \delta_{RO}^{(M)}\mu^2]. \tag{65}$$

Operation of the vibrator with series load capacitance modifies the effective coupling factor as shown in Eq. (44). The modified value for $k^2$ introduced into Eqs. (62)–(65) produces the approximations pertinent to the use of $\delta_{L0}^{(M)}$ and $\delta_{L\mu}^{(M)}$.

## IV. Static Frequency–Temperature Behavior

One of the most important practical considerations for frequency control and selection is that of temperature behavior. The AT cut has maintained its dominant position among the thickness mode resonators for so many years mainly because of its superior characteristics in this regard. This section outlines how the temperature influence on the various critical frequencies is treated phenomenologically under the assumption that thermal changes take place slowly enough so that the vibrator is constantly at thermal equilibrium. The static behavior is described for single and multiple modes along with associated approximations.

### A. First Order Temperature Coefficients

Bechmann (1956) expanded the static frequency–temperature function as a power series and found that three terms were normally sufficient for an adequate description of AT- and BT-cut quartz resonators. This formalism has subsequently been applied to general, doubly rotated cuts of quartz and to other materials with satisfactory results.

If at reference temperature $T_0$ the critical frequency of interest is $f_0$, the expansion is

$$(f - f_0)/f_0 = \Delta f / f_0 = \sum_{n}^{3} T_f^{(n)}(T - T_0)^n \tag{66}$$

with

$$T_f^{(n)} = [(\partial^n f / \partial T^n)/n! \, f_0]_{T = T_0}. \tag{67}$$

The higher order terms with $n = 2$ and 3 are dealt with in Section IV,B; here the linear term is considered. As with the critical frequencies themselves, the temperature coefficients may be coupled or uncoupled. Simplest of all to describe are the first order temperature coefficients of the antiresonance frequencies. These are found by taking the logarithmic derivative of Eq. (41) with substitution of Eq. (19) to obtain

$$T_{f_{mA}}^{(1)} = \tfrac{1}{2}T_{\bar{c}_m}^{(1)} - \tfrac{1}{2}T_\rho^{(1)} - T_h^{(1)}. \tag{68}$$

$T_\rho^{(1)}$ and $T_h^{(1)}$ are obtained from the thermoelastic constants for the material,

while $T_{\bar{a}_m}^{(1)}$ requires differentiation of the cubic that arises from Eq. (17).[1] Because the $\Gamma_{jk}$ involve the elastic, piezoelectric, and dielectric material constants plus the plate orientation angles, the expression for $T_{\bar{a}_m}^{(1)}$ is lengthy in general, but is nevertheless straightforward. In Eq. (68) the superscript relating to the harmonic $(M)$ has been omitted; the antiresonance result is independent of $M$.

Using Eq. (68), the locus of $T_{f_{m\mathrm{A}}}^{(1)} = 0$ was mapped in detail by Bechmann *et al.* (1962) for quartz, with the result shown in Fig. 5. The angles are
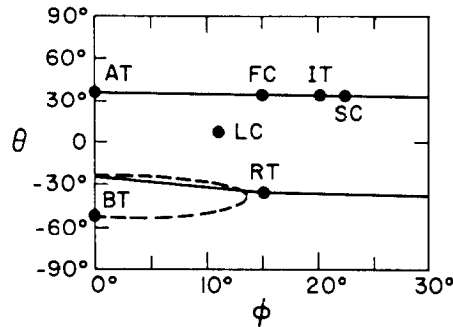


FIG. 5. Loci of zeros of first order temperature coefficient of antiresonance frequency in quartz. The angles are those shown in Fig. 1. Solid lines denote the slower quasi-shear mode $c$; the dashed loop indicates the faster quasi-shear mode $b$. Locations of a number of useful cuts are shown.

those described in connection with Fig. 1. In Fig. 5 the locations of the AT and BT cuts are seen to belong to different branches. Shown dashed is the zero temperature coefficient locus for the $b$ mode, while the solid lines indicate the locus for the $c$ mode. Also indicated are a number of additional cuts: the IT cut (Bottom and Ives, 1951); the RT cut (Bechmann, 1961); the LC cut (Hammond and Benjaminson, 1965); the FC cut (Lagasse *et al.*, 1972); and the SC cut (Holland, 1974; EerNisse, 1975). These cuts will be discussed more extensively in Section V,A in connection with properties of quartz. It is important to notice here that the presence of a continuous locus of zero

---

[1] In defining the temperature derivative of the elastic constants, $\rho$, $h$, and $\bar{c}_m$ are allowed to vary. However, more fundamental equations could have been derived in terms of reference (material) coordinates, and $\rho$ and $h$ would have been constant. The result would have been an equally valid, but numerically different, set of effective elastic constant temperature coefficients. In either case the temperature dependence of the effective elastic constants depends explicitly on temperature and strain, including the strain dependence on temperature.

Very recently (Tiersten, 1975a), an analysis has been made using the third-order elastic stiffnesses; the portions of dependence of the effective elastic constants on the third-order stiffnesses and on the change in strain with temperature have been calculated. From these results the fundamental dependence of the effective elastic constants on temperature can be obtained (H. F. Tiersten, private communication, 1976).

The alternate procedure, used here, was that followed by Bechmann *et al.* (1962); the third-order elastic constants only became available at a later date (Thurston *et al.*, 1966).

temperature coefficient orientations affords the possibility of locating a cut having some other optimal property simultaneously with good static thermal characteristics.

Figure 5, plotted for the thickness modes, also furnishes the approximate loci for other modes, e.g., contour modes (Baldwin and Bokovoy, 1936), and surface acoustic wave (SAW) modes (Schulz *et al.*, 1970). When $\bar{c}_m$ and $h$ are defined properly, Eq. (68) is just the negative of the temperature coefficient of delay employed in SAW analyses; to characterize these elements requires the addition to Fig. 5 of a third axis representing propagation angle so the zero locus is a surface in angle space.

Resonance frequencies differ from the antiresonances in depending upon the coupling factor. For the single mode case, Onoe (1969) showed that the difference between the resonance and antiresonance temperature coefficients is proportional to the temperature coefficient of coupling:

$$T^{(1)}_{f_R} - T^{(1)}_{f_A} = T^{(1)}_X = -G_0 T^{(1)}_k, \tag{69}$$

where

$$G_0 = 2k^2/(X^2 + k^2(k^2 - 1)), \tag{70}$$

and where $X$ is the $M$th root of Eq. (50). In the limit of small $k$, Eq. (70) becomes

$$G_0 \simeq 8k^2/\pi^2 M^2. \tag{71}$$

This approximation is suitable for many quartz applications, and on the scale of Fig. 5 no sensible difference between $T^{(1)}_{f_R}$ and $T^{(1)}_{f_A}$ would be manifest. For high precision applications, as well as for high coupling materials, Eq. (70) must be used since the difference in the temperature coefficients can be appreciable. An example is given in Section V,C. Equations (69)–(70) contain the influence of harmonic on $T^{(1)}_{f_R}$; the additional effect of mass loading has been given recently (Ballato, 1976). Insertion of a series load capacitor $C_L$ also shifts the temperature behavior, its influence acting like a shift to a higher harmonic with the exception that the harmonic shift is quantized. The load frequency temperature coefficient is approximately

$$T^{(1)}_{f_L} \simeq T^{(1)}_{f_A} - G_0 T^{(1)}_k/(1 + C_0/C_L). \tag{72}$$

When considering the multimode case, Eq. (42) must be differentiated to find the temperature coefficient of resonance frequency. The result is

$$T^{(1)}_{f_R} = \sum_p^3 k_p^2(A_p T^{(1)}_{f_{pA}} + 2B_p T^{(1)}_{k_p}) \bigg/ \sum_q^3 k_q^2 A_q, \tag{73}$$

where

$$B_m = \tan X^{(m)}/X^{(m)}, \qquad A_m = B_m - \sec^2 X^{(m)}, \tag{74}$$

and where $X^{(m)}$ is a root of Eq. (42).

Alternatively, one may find $T_{f_R}^{(1)}$ numerically by computing the effective values of the elastic, piezoelectric, and dielectric constants at two temperatures using their temperature coefficients in the analog of Eq. (66) and then finding $f_R$ at those temperatures in the manner described earlier. From these values and the temperature interval, $T_{f_R}^{(1)}$ follows approximately from Eq. (67).

## B. Higher Order Temperature Coefficients

Expressions analogous to Eq. (68) for $n = 2$ and 3 were derived in Bechmann *et al.* (1962). These are more succinctly written as

$$\hat{T}_{f_{mA}}^{(n)} = \tfrac{1}{2}\hat{T}_{\bar{c}_m}^{(n)} - \tfrac{1}{2}\hat{T}_\rho^{(n)} - \hat{T}_h^{(n)}, \tag{75}$$

where

$$\hat{T}_Y^{(n)} = \begin{cases} T_Y^{(1)} & \text{for } n = 1, \tag{76} \\[2mm] T_Y^{(2)} - \tfrac{1}{2}(T_Y^{(1)})^2 & \text{for } n = 2, \tag{77} \\[2mm] T_Y^{(3)} - T_Y^{(2)} \cdot T_Y^{(1)} + \tfrac{1}{3}(T_Y^{(1)})^3 & \text{for } n = 3, \tag{78} \end{cases}$$

and where $Y$ is $f_{mA}$, $\bar{c}_m$, $\rho$, or $h$. Altitude charts for all three orders of the $c$ mode in quartz are given in Hafner (1974). Only one orientation exists where $T_{f_{mA}}^{(n)} = 0$ simultaneously for $n = 2$ and 3; this occurs for the $c$ mode, and defines the LC cut (Hammond and Benjaminson, 1965). At this orientation the frequency–temperature curve is ultralinear and the cuts are well suited for thermometric application.

The higher order temperature coefficients are listed in Table I for selected cuts along the upper zero locus of Fig. 5. The inflection temperature $T_i$, defined as the temperature for which the second derivative of Eq. (66) vanishes, is obtained from

$$T_i - T_0 = -T_{f_A}^{(2)}/3T_{f_A}^{(3)}; \tag{79}$$

it is seen from Table I to increase monotonically with angle $\varphi$.

TABLE I

HIGHER ORDER TEMPERATURE COEFFI-
CIENTS OF QUARTZ CUTS (MODE $c$)

| Cut | $T_{f_A}^{(2)}$ $(10^{-9}/\mathrm{K}^2)$ | $T_{f_A}^{(3)}$ $(10^{-12}/\mathrm{K}^3)$ |
|-----|------|------|
| AT | −0.45 | 108.6 |
| 5° V | −1.77 | 104.7 |
| 10° V | −2.65 | 96.2 |
| 13.9° V | −4.37 | 85.6 |
| FC | −5.55 | 82.2 |
| IT | −10.1 | 68.4 |
| SC | −12.3 | 58.2 |
| 25° V | −13.8 | 47.4 |
| 30° V | −12.4 | 31.4 |

Resonance frequency temperature coefficients for the single mode case
are determined from the relations

$$T_X^{(2)} = T_{f_R}^{(2)} - T_{f_A}^{(2)} - T_X^{(1)}T_{f_A}^{(1)}, \tag{80}$$

$$T_X^{(3)} = T_{f_R}^{(3)} - T_{f_A}^{(3)} - T_X^{(2)}T_{f_A}^{(1)} - T_X^{(1)}T_{f_A}^{(2)} \tag{81}$$

with $T_X^{(1)}$ from Eq. (69), and $T_X^{(2)}$ and $T_X^{(3)}$ determined approximately from

$$\hat{T}_X^{(n)} \simeq -G_0 \, \hat{T}_k^{(n)} \tag{82}$$

for $n = 2, 3$. $G_0$ is given in Eq. (70); $X$ and $k$ are to be used for $Y$ from Eqs.
(77)–(78) in the expansions of Eq. (82). These equations and those corre-
sponding for $n = 1$ relate $T_{f_R}^{(n)}$ to $T_{f_A}^{(n)}$ and the associated coupling factor
coefficients of different orders. $T_{f_A}^{(n)}$ is found from Eqs. (75)–(78) in the
manner described for $n = 1$ following Eq. (68); $T_k^{(n)}$ is obtained from differen-
tiation of Eq. (33).

Inclusion of mass-loading effects leads to modification of Eqs. (75),
(79)–(82), and is treated in detail by Ballato and Lukaszek (1975). Exper-
imental data relating $\mu$ to changes in the higher order coefficients are pres-
ently very scarce; T. J. Lukaszek (private communication, 1976) has found
a lowering of $T_i$ with $\mu$.

The higher order coefficients for the resonance frequencies in the
multimode case may be determined after the manner of Eq. (73), but the
results are quite lengthy, and recourse to the numerical method is not to be
discouraged.

## V. Properties of Doubly Rotated Cuts

This section is devoted to a compilation of data on doubly rotated cuts of four materials: quartz, aluminum phosphate, lithium tantalate, and lithium niobate. Quartz and aluminum phosphate are members of crystal class 32 and have remarkably similar properties. Quartz is treated in considerable detail. Its position as perennial favorite for many frequency control applications certainly merits an expanded account. However, the attention given this familiar material here is largely for a different reason: that a new, and hitherto unsuspected, but most desirable, property has recently come to light. It appears that certain doubly rotated orientations in quartz possess compensating combinations of nonlinear elastic properties that render the plate frequencies insensitive to mechanical and thermal shocks of various types. This fortunate circumstance can be expected to have widespread consequences for a number of high precision uses. Aluminum phosphate, like quartz, has a locus of zero temperature coefficient cuts—a property only recently determined (Chang and Barsch, 1976). It has an appealing potential for wider band resonator, filter, and SAW applications because it combines low loss with piezoelectric coupling factors about 2.5 times that of quartz.

Lithium tantalate and lithium niobate are refractory oxides of crystal class 3*m*. The tantalate possesses a locus of zero temperature cuts and moderate to large coupling values, making it suitable for wideband filter and transducer uses. Lithium niobate lacks cuts having zero temperature coefficients, but its large coupling coefficients commend it for a variety of transducer applications.

Although they could not be included here, a number of additional types of materials deserve mention as potential candidates for future work. These include the tungsten bronze structures (crystal class 4*mm*) comprising the solid solutions consisting of mixtures of strontium barium niobate with barium lithium niobate; for various ratios these are likely to have good temperature behavior with sizeable piezoelectric coupling. A group of sulfosalts appears to have promise as high coupling, low velocity, and zero temperature coefficient materials. $Tl_3VS_4$, in class $\bar{4}3m$ is representative (Weinert and Isaacs, 1975). These and other crystals from the 20 piezoelectric classes may be characterized as to their resonator properties by means of the theory outlined in previous sections. Compilations of measured crystal constants may be found in the Landolt–Börnstein tables (1966, 1969).

### A. Quartz

In the first part of this section the linear properties of quartz pertinent to vibrators are discussed. The next portion considers those effects relying on nonlinear elastic behavior. Tradeoffs between doubly rotated quartz cuts

and the traditional AT cut are given in the last part of the section. All calculations were carried out using as input data the values given by Bechmann (1951, 1958) and Bechmann *et al.* (1962), along with the temperature coefficients of permittivity from Landolt–Börnstein (1966). Alternative sets of constants such as those of Koga *et al.* (1958), McSkimin *et al.* (1965), or Zelenka and Lee (1971) produce results differing from those given here generally by only a small percentage, which is comparable to the error likely to be encountered in using the one-dimensional approximation. Additional results for this material are given in Section VI. An excellent resume of other aspects of quartz crystal resonators, their technology, and applications is given by Hafner (1974) with further references to the literature.

### 1. *Linear Properties of Quartz Resonators*

A global view of the most important resonator quantities of interest is given in Fig. 6 for orientations $(YXwl)\varphi/\theta$, with $\varphi = 0°(6°)30°$ and $-90° \leq \theta \leq 90°$. The three modes are labeled in accordance with Eq. (18). Frequency constants $N_m$ are obtained from halving the velocities in Eq. (19); coupling factors are found from Eq. (33); and Eq. (68) yields the antiresonance temperature coefficients.

For cuts $(YXw)\varphi$, $|k_a|$ rises nearly linearly from zero at $\varphi = 0°$ to about 9% at $\varphi = 30°$; $|k_b|$ rises in a parabolic fashion from zero at $\varphi = 0°$ to a 7% maximum at $\varphi \simeq 11°$, and falls parabolically to zero at $\varphi = 30°$; $|k_c|$ falls nearly linearly from about 13.5% at $\varphi = 0°$ to zero at $\varphi = 30°$. All modes nearly coincide at 6.5% for $\varphi = 18°$.

Because $X_1$ is a digonal symmetry axis in quartz, the elastic constants with indices 15, 16, 25, 26, 35, 36, 45, and 46 vanish along with the piezoelectric constants with indices 15, 16, 21, 22, 23, 24, 31, 32, 33, and 34. For rotated-Y-cut plates $(YXl)\theta$, the digonal axis is, moreover, contained in the plane of the plate, and this leads to zero $\varphi$ derivatives of many quantities. These cuts are therefore less complicated than doubly rotated cuts. For example, only the pure shear mode is piezoelectrically driven. In the sequel we shall give values for various quantities and their angle derivatives for a number of doubly rotated cuts so that the effects of angle variations may be calculated from the relation

$$q(\varphi, \theta) \simeq q(\varphi_0, \theta_0) + (\partial q/\partial \varphi)(\varphi - \varphi_0) + (\partial q/\partial \theta)(\theta - \theta_0), \qquad (83)$$

where $q$ is any quantity. When $\varphi_0 = 0°$, one usually has to extend the expansion to second order. The most important instance of this is the expansion for the temperature coefficient of the AT-cut $c$ mode:

$$T_{f_A}^{(1)}(\varphi, \theta) - T_{f_A}^{(1)}(0°, \theta_0) \simeq (-5.1 \times 10^{-6}/\text{K}, \,°\theta)(\theta - \theta_0)$$

$$+ (-9.0 \times 10^{-9}/\text{K}, \,(°\varphi)^2)(\varphi)^2. \qquad (84)$$
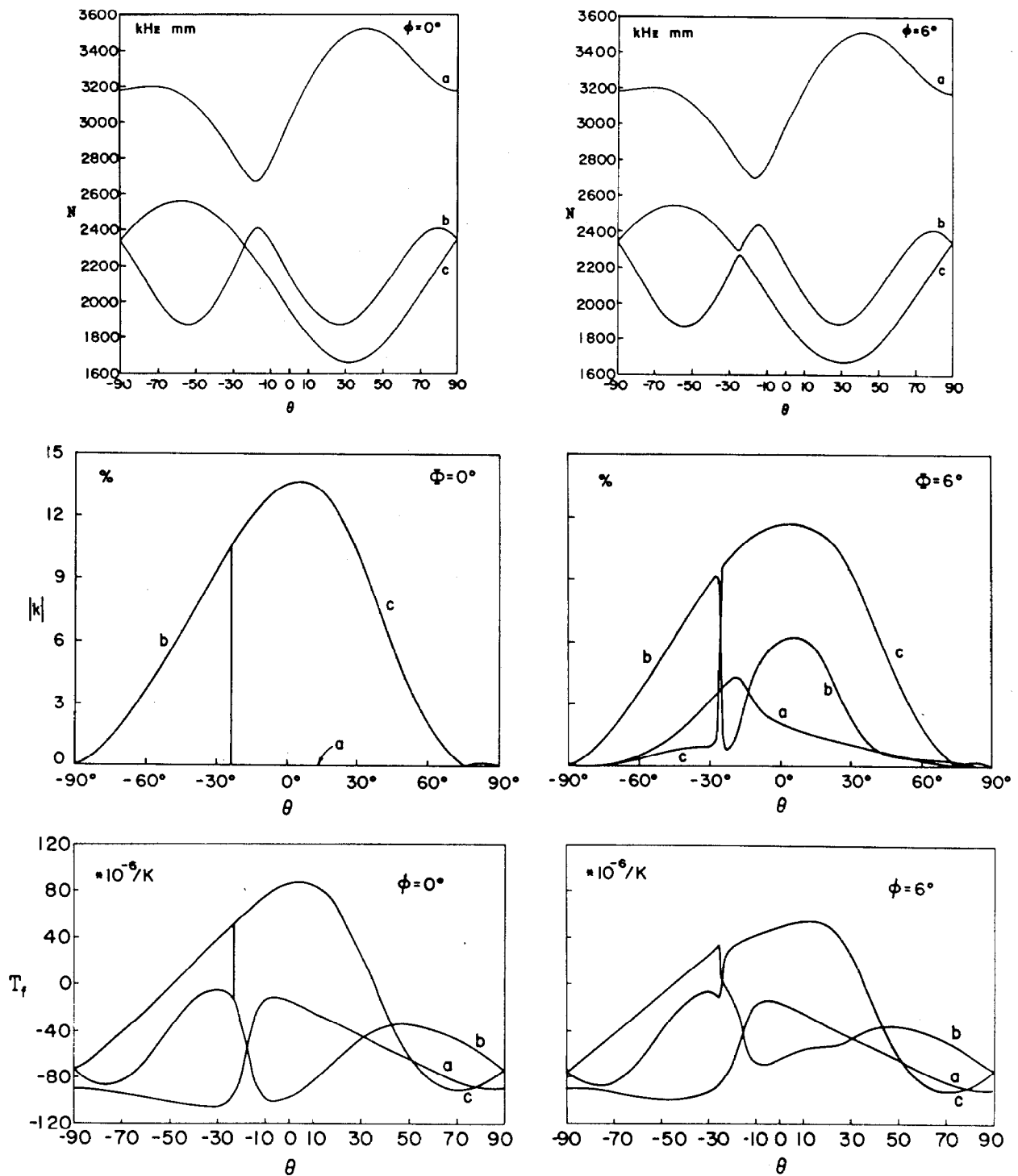
FIG. 6. Thickness mode properties of doubly rotated cuts of quartz. Frequency constants $N$ are in kHz mm, coupling factors $|k|$ are in percent, and temperature coefficients $T_f^{(1)}$ are in $10^{-6}/K$.
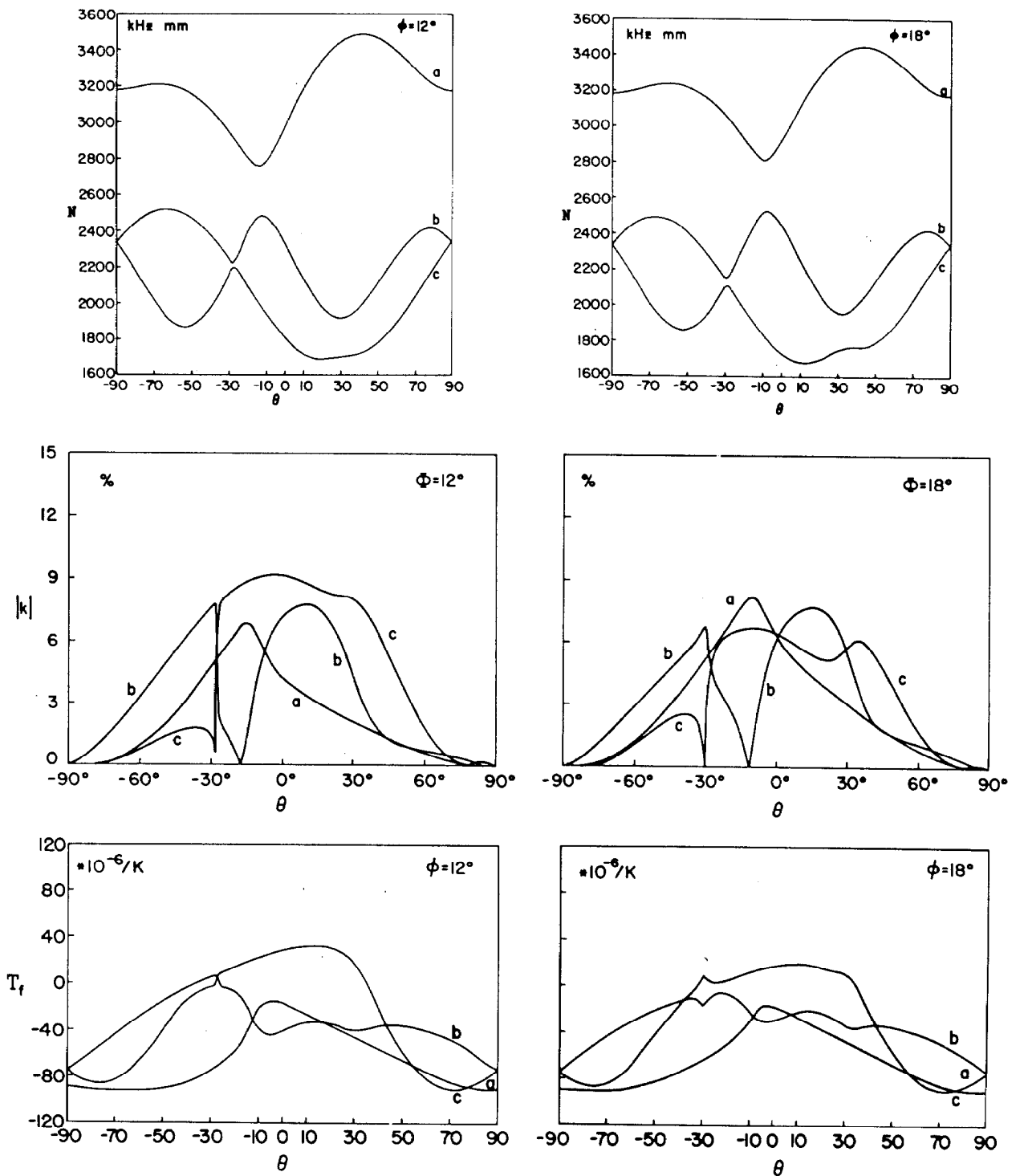
FIG. 6—*continued*

Equations (83)–(84) are extremely useful for determining the influence of manufacturing deviations on yield and the tradeoff between angular errors.

Figure 5 displays the loci of $T_{f_A}^{(1)} = 0$ for modes $b$ and $c$. From Fig. 5 one

FIG. 6—*continued*

sees that the *b*- and *c*-mode curves touch at $\varphi = 0°$, $\theta \simeq -24°$, corresponding to the point in Fig. 6 where $N_b = N_c$. Another point of degeneracy exists in quartz. It was found by Epstein (1973) and occurs at the point in Fig. 5

TABLE II

FREQUENCY CONSTANTS AND ANGLE GRADIENTS. QUARTZ CUTS $(YXwl)\varphi/\theta > 0$ [a]

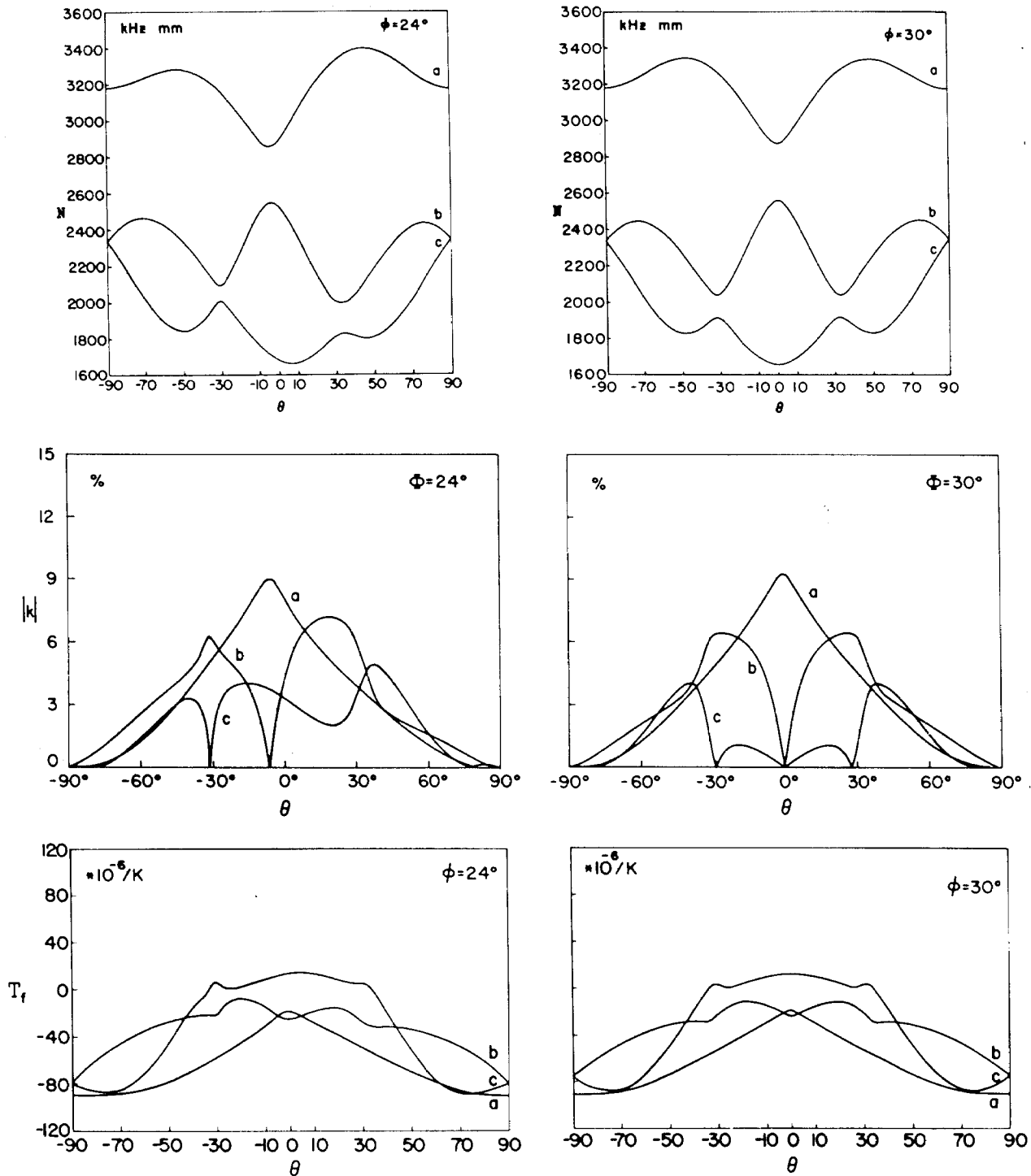| Crystal cut | $\varphi$ | $\theta$ | $N_a$ | $N_b$ | $N_c$ | $\dfrac{\partial N_a}{\partial \theta}$ | $\dfrac{\partial N_b}{\partial \theta}$ | $\dfrac{\partial N_c}{\partial \theta}$ | $\dfrac{\partial N_a}{\partial \varphi}$ | $\dfrac{\partial N_b}{\partial \varphi}$ | $\dfrac{\partial N_c}{\partial \varphi}$ |
|---|---|---|---|---|---|---|---|---|---|---|---|
| | degrees | | kHz mm | | | kHz mm/deg $\theta$ | | | kHz mm/deg $\varphi$ | | |
| AT | 0 | 35.25 | 3504 | 1900 | 1661 | 3.60 | 6.91 | 2.09 | 0 | 0 | 0 |
| 5 V | 5 | 34.94 | 3497 | 1903 | 1668 | 3.89 | 6.46 | 1.92 | −2.45 | 1.90 | 3.02 |
| 10 V | 10 | 34.64 | 3477 | 1915 | 1690 | 4.34 | 5.59 | 1.87 | −4.89 | 3.70 | 5.95 |
| 13.9 V | 13.90 | 34.40 | 3454 | 1931 | 1717 | 4.81 | 4.71 | 1.83 | −6.76 | 4.96 | 8.12 |
| FC | 15 | 34.33 | 3446 | 1936 | 1726 | 4.96 | 4.45 | 1.80 | −7.28 | 5.29 | 8.71 |
| IT | 19.10 | 34.08 | 3411 | 1959 | 1766 | 5.59 | 3.56 | 1.51 | −9.17 | 6.39 | 10.8 |
| SC | 21.93 | 33.93 | 3382 | 1977 | 1797 | 6.08 | 3.15 | 1.03 | −10.4 | 7.05 | 12.0 |
| 25 V | 25 | 33.72 | 3346 | 2000 | 1836 | 6.67 | 3.05 | 0.06 | −11.7 | 7.76 | 13.1 |
| 30 V | 30 | 33.42 | 3281 | 2041 | 1905 | 7.76 | 4.36 | −3.13 | −13.7 | 9.14 | 13.9 |
| LC | 11.17 | 9.39 | 3165 | 2140 | 1727 | 19.0 | −17.9 | −7.15 | −6.07 | 17.1 | −10.0 |

[a] $T_f^{(1)} = 0$ for the $c$ mode of these cuts.

where the $b$-mode loop intersects the $c$-mode line at $\varphi \simeq 10.4°$, $\theta \simeq -26.6°$. Near this point the power flow angles exhibit their maximum departures from the propagation direction $\zeta$.

The cuts selected for inclusion in the following tables are those having $T_f^{(1)} = 0$, plus the LC cut. Of greatest importance is the $c$-mode locus for

TABLE III

FREQUENCY CONSTANTS AND ANGLE GRADIENTS. QUARTZ CUTS $(YXwl)\varphi/\theta < 0$ [a]

| Crystal cut | $\varphi$ | $\theta$ | $N_a$ | $N_b$ | $N_c$ | $\dfrac{\partial N_a}{\partial \theta}$ | $\dfrac{\partial N_b}{\partial \theta}$ | $\dfrac{\partial N_c}{\partial \theta}$ | $\dfrac{\partial N_a}{\partial \varphi}$ | $\dfrac{\partial N_b}{\partial \varphi}$ | $\dfrac{\partial N_c}{\partial \varphi}$ |
|---|---|---|---|---|---|---|---|---|---|---|---|
| | degrees | | kHz mm | | | kHz mm/deg $\theta$ | | | kHz mm deg $\varphi$ | | |
| BT | 0 | −49.20 | 3089 | 2536 | 1884 | −10.2 | −3.84 | 5.56 | 0 | 0 | 0 |
| | 5 | −46.56 | 3075 | 2508 | 1901 | −10.6 | −5.76 | 8.44 | 5.69 | −6.32 | −0.89 |
| | 10 | −38.63 | 3032 | 2391 | 1990 | −11.8 | −10.9 | 15.9 | 12.9 | −14.0 | −2.92 |
| | 5 | −24.98 | 2769 | 2296 | 2277 | −15.5 | −6.66 | 15.2 | 12.1 | −10.8 | −3.85 |
| | 10 | −32.23 | 2950 | 2313 | 2107 | −13.8 | −13.1 | 20.5 | 15.4 | −16.3 | −3.71 |
| | 12.5 | −33.33 | 3004 | 2286 | 2075 | −12.6 | −13.6 | 19.5 | 16.1 | −17.0 | −4.63 |
| RT | 15 | −34.50 | 3059 | 2260 | 2040 | −11.3 | −13.9 | 18.2 | 16.1 | −17.0 | −5.46 |
| | 17.5 | −35.78 | 3112 | 2236 | 2003 | −9.96 | −14.1 | 16.5 | 15.8 | −16.6 | −6.13 |
| | 20 | −36.79 | 3161 | 2209 | 1971 | −8.72 | −14.2 | 14.9 | 15.3 | −16.0 | −6.76 |

[a] $T_f^{(1)} = 0$ for the $b$ mode of first three entries; for the $c$ mode of remainder.
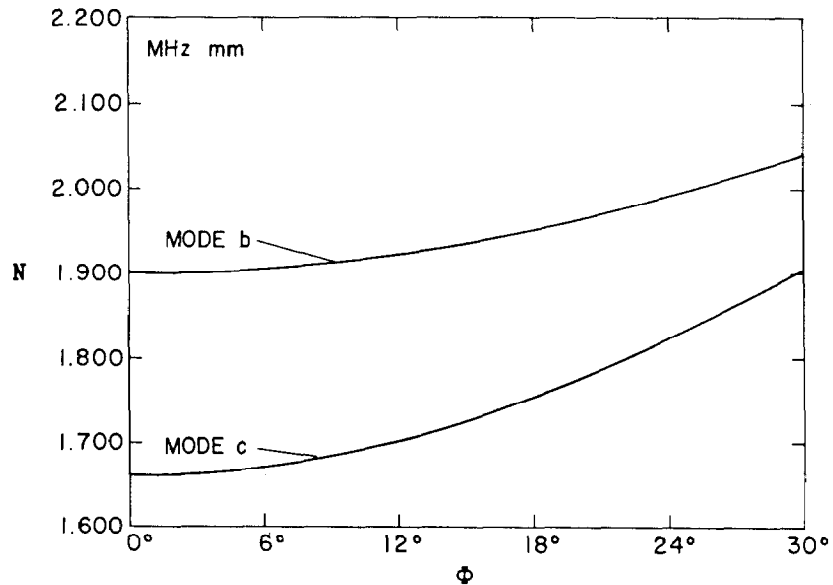
FIG. 7. Antiresonance frequency constants of the *b* and *c* modes in quartz along the AT-SC locus of Fig. 5. Mode separation declines from 14% at the AT cut to 10% at the SC cut.

$\theta > 0°$ which is adequately described by a straight line with equation

$$\theta° = +35.25° - (11/180)\varphi°. \tag{85}$$

Its importance derives from the nonlinear behavior discussed in Section V,A,2. Figure 7 shows, for the *b* and *c* modes, the antiresonance frequency constants along this locus. Tables II and III list $N_m$ and their angle gradients for $\theta \gtrless 0°$, respectively. Tables IV and V similarly pertain to $|k_m|$, with Fig. 8 showing plots of the coupling factors on the upper zero temperature coefficient locus.
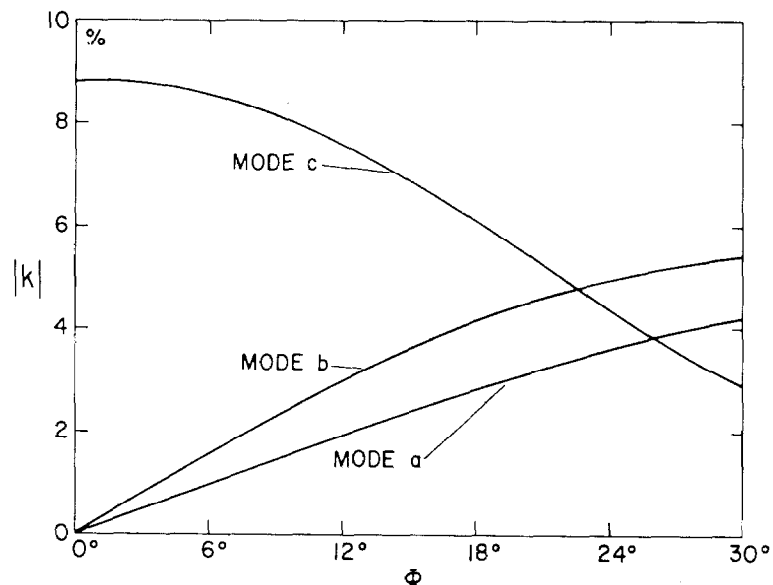


FIG. 8. Piezoelectric coupling factors along the AT-SC locus of Fig. 5. At the SC cut, the *b* and *c* mode excitations are approximately equal.

TABLE IV

COUPLING FACTORS AND THEIR ANGLE GRADIENTS. QUARTZ CUTS $(YXwl)\varphi/\theta > 0$ [a]

| Crystal cut | $\varphi$ | $\theta$ | $|k_a|$ | $|k_b|$ | $|k_c|$ | $\dfrac{\partial|k_a|}{\partial\theta}$ | $\dfrac{\partial|k_b|}{\partial\theta}$ | $\dfrac{\partial|k_c|}{\partial\theta}$ | $\dfrac{\partial|k_a|}{\partial\varphi}$ | $\dfrac{\partial|k_b|}{\partial\varphi}$ | $\dfrac{\partial|k_c|}{\partial\varphi}$ |
|---|---|---|---|---|---|---|---|---|---|---|---|
| | degrees | | percent | | | $10^{-3}/\deg\theta$ | | | $10^{-3}/\deg\varphi$ | | |
| AT | 0 | 35.25 | 0 | 0 | 8.80 | 0 | 0 | −2.97 | 1.57 | 2.57 | 0 |
| 5 V | 5 | 34.94 | 0.80 | 1.29 | 8.63 | −0.24 | −1.28 | −2.69 | 1.59 | 2.50 | −1.00 |
| 10 V | 10 | 34.64 | 1.60 | 2.53 | 7.97 | −0.47 | −2.45 | −1.88 | 1.54 | 2.21 | −1.90 |
| 13.9 V | 13.90 | 34.40 | 2.20 | 3.39 | 7.16 | −0.65 | −3.13 | −0.93 | 1.47 | 1.87 | −2.42 |
| FC | 15 | 34.33 | 2.37 | 3.61 | 6.89 | −0.69 | −3.27 | −0.61 | 1.44 | 1.76 | −2.53 |
| IT | 19.10 | 34.08 | 2.96 | 4.33 | 5.79 | −0.87 | −3.69 | 0.72 | 1.33 | 1.30 | −2.78 |
| SC | 21.93 | 33.93 | 3.33 | 4.71 | 4.99 | −0.98 | −3.81 | 1.75 | 1.23 | 0.98 | −2.78 |
| 25 V | 25 | 33.72 | 3.71 | 5.05 | 4.11 | −1.10 | −3.81 | 3.01 | 1.09 | 0.70 | −2.58 |
| 30 V | 30 | 33.42 | 4.23 | 5.43 | 2.87 | −1.28 | −3.56 | 5.19 | 0.82 | 0.39 | −1.73 |
| LC | 11.17 | 9.39 | 3.21 | 7.64 | 9.21 | −0.67 | 0.03 | −0.45 | 0.28 | 1.15 | −4.63 |

[a] $T_{f_A}^{(1)} = 0$ for the $c$ mode of these cuts.

TABLE V

COUPLING FACTORS AND THEIR ANGLE GRADIENTS. QUARTZ CUTS $(YXwl)\varphi/\theta < 0$ [a]

| Crystal cut | $\varphi$ | $\theta$ | $|k_a|$ | $|k_b|$ | $|k_c|$ | $\dfrac{\partial|k_a|}{\partial\theta}$ | $\dfrac{\partial|k_b|}{\partial\theta}$ | $\dfrac{\partial|k_c|}{\partial\theta}$ | $\dfrac{\partial|k_a|}{\partial\varphi}$ | $\dfrac{\partial|k_b|}{\partial\varphi}$ | $\dfrac{\partial|k_c|}{\partial\varphi}$ |
|---|---|---|---|---|---|---|---|---|---|---|---|
| | degrees | | percent | | | $10^{-3}/\deg\theta$ | | | $10^{-3}/\deg\varphi$ | | |
| BT | 0 | −49.20 | 0 | 5.62 | 0 | 0 | 1.95 | 0 | 2.34 | 0 | 1.11 |
| | 5 | −46.56 | 1.16 | 5.96 | 0.64 | 0.71 | 1.85 | 0.20 | 2.08 | −0.68 | 1.27 |
| | 10 | −38.63 | 3.02 | 6.73 | 1.49 | 1.36 | 1.48 | 0.15 | 1.78 | −1.53 | 1.43 |
| | 5 | −24.98 | 3.24 | 8.67 | 4.42 | 1.08 | −31.2 | 63.1 | 5.11 | −13.0 | 20.7 |
| | 10 | −32.23 | 3.93 | 7.63 | 1.49 | 1.49 | 1.32 | −0.16 | 2.07 | −1.89 | 1.17 |
| | 12.5 | −33.33 | 4.19 | 7.03 | 1.80 | 1.54 | 1.27 | −0.40 | 1.35 | −1.77 | 1.06 |
| RT | 15 | −34.50 | 4.27 | 6.46 | 2.12 | 1.55 | 1.26 | −0.54 | 0.82 | −1.63 | 1.03 |
| | 17.5 | −35.78 | 4.23 | 5.90 | 2.45 | 1.52 | 1.27 | −0.53 | 0.42 | −1.50 | 1.07 |
| | 20 | −36.79 | 4.14 | 5.41 | 2.77 | 1.48 | 1.30 | −0.49 | 0.12 | −1.39 | 1.10 |

[a] $T_{f_A}^{(1)} = 0$ for the $b$ mode of first three entries; for the $c$ mode of remainder.

The temperature coefficients of antiresonance frequency and their angle gradients for the selected cuts are given in Tables VI and VII. Corresponding entries for the coupling temperature coefficients appear in Tables VIII and IX. Use of the $T_{km}^{(1)}$ values in Eq. (69) discloses that along the locus expressed

by Eq. (85), $T_X^{(1)}$ for mode $c$ remains nearly constant at $-0.25 \times 10^{-6}/\mathrm{K}$ for $\varphi < 18°$ and then nearly linearly increases to $-0.15 \times 10^{-6}/\mathrm{K}$ at $\varphi = 30°$. Associated with the solution to Eq. (17) are the piezoelectrically

TABLE VI

ANTIRESONANCE FREQUENCY TEMPERATURE COEFFICIENTS AND THEIR ANGLE GRADIENTS. QUARTZ CUTS $(YXwl)\varphi/\theta > 0$ [a]

| Crystal cut | $\varphi$ | $\theta$ | $Tf(a)$ | $Tf(b)$ | $Tf(c)$ | $\dfrac{\partial Tf(a)}{\partial \theta}$ | $\dfrac{\partial Tf(b)}{\partial \theta}$ | $\dfrac{\partial Tf(c)}{\partial \theta}$ | $\dfrac{\partial Tf(a)}{\partial \varphi}$ | $\dfrac{\partial Tf(b)}{\partial \varphi}$ | $\dfrac{\partial Tf(c)}{\partial \varphi}$ |
|---|---|---|---|---|---|---|---|---|---|---|---|
| | degrees | | $10^{-6}/\mathrm{K}$ | | | $10^{-6}/\mathrm{K}$ deg $\theta$ | | | $10^{-6}/\mathrm{K}$ deg $\varphi$ | | |
| AT | 0 | 35.25 | −48.9 | −31.3 | 0 | −0.86 | 1.54 | −5.08 | 0 | 0 | 0 |
| 5° V | 5 | 34.94 | −48.8 | −31.3 | 0 | −0.87 | 1.52 | −4.99 | −0.09 | 0.16 | −0.10 |
| 10° V | 10 | 34.64 | −49.2 | −30.6 | 0 | −0.87 | 1.40 | −4.71 | −0.18 | 0.31 | −0.18 |
| 13.9° V | 13.90 | 34.40 | −49.8 | −29.5 | 0 | −0.87 | 1.26 | −4.41 | −0.25 | 0.41 | −0.21 |
| FC | 15 | 34.33 | −50.1 | −29.1 | 0 | −0.87 | 1.21 | −4.32 | −0.28 | 0.43 | −0.21 |
| IT | 19.10 | 34.08 | −51.2 | −27.5 | 0 | −0.87 | 1.07 | −3.98 | −0.37 | 0.50 | −0.20 |
| SC | 21.93 | 33.93 | −52.1 | −26.2 | 0 | −0.88 | 1.02 | −3.78 | −0.44 | 0.54 | −0.18 |
| 25° V | 25 | 33.72 | −53.5 | −24.7 | 0 | −0.88 | 1.05 | −3.65 | −0.53 | 0.60 | −0.15 |
| 30° V | 30 | 33.42 | −56.3 | −21.5 | 0 | −0.88 | 1.45 | −3.80 | −0.71 | 0.85 | −0.22 |
| LC | 11.17 | 9.39 | −26.1 | −39.7 | 39.8 | −0.93 | 0.55 | 0.34 | −0.19 | 2.58 | −2.28 |

[a] $Tf(m)$ stands for $T_{f_A}^{(1)}$ (mode $m$).

TABLE VII

ANTIRESONANCE FREQUENCY TEMPERATURE COEFFICIENTS AND THEIR ANGLE GRADIENTS. QUARTZ CUTS $(YXwl)\varphi/\theta < 0$ [a]

| Crystal cut | $\varphi$ | $\theta$ | $Tf(a)$ | $Tf(b)$ | $Tf(c)$ | $\dfrac{\partial Tf(a)}{\partial \theta}$ | $\dfrac{\partial Tf(b)}{\partial \theta}$ | $\dfrac{\partial Tf(c)}{\partial \theta}$ | $\dfrac{\partial Tf(a)}{\partial \varphi}$ | $\dfrac{\partial Tf(b)}{\partial \varphi}$ | $\dfrac{\partial Tf(c)}{\partial \varphi}$ |
|---|---|---|---|---|---|---|---|---|---|---|---|
| | degrees | | $10^{-6}/\mathrm{K}$ | | | $10^{-6}/\mathrm{K}$ deg $\theta$ | | | $10^{-6}/\mathrm{K}$ deg $\varphi$ | | |
| BT | 0 | −49.20 | −95.6 | 0 | −30.9 | −0.74 | 2.06 | 2.84 | 0 | 0 | 0 |
| | 5 | −46.56 | −94.5 | 0 | −24.0 | −0.46 | 1.82 | 2.61 | 1.09 | −1.05 | −0.10 |
| | 10 | −38.63 | −86.6 | 0 | −7.71 | 0.35 | 1.18 | 1.57 | 2.06 | −2.02 | −0.05 |
| | 5 | −24.98 | −91.4 | 39.7 | 0 | 1.49 | −8.31 | 8.37 | 3.19 | −4.81 | 1.77 |
| | 10 | −32.23 | −83.4 | 11.7 | 0 | 0.69 | 1.06 | 0.55 | 2.48 | −2.65 | 0.28 |
| | 12.5 | −33.33 | −78.5 | 4.52 | 0 | 0.74 | 0.78 | 0.96 | 2.07 | −2.28 | 0.32 |
| RT | 15 | −34.50 | −74.6 | −1.49 | 0 | 0.76 | 0.56 | 1.37 | 1.71 | −1.92 | 0.32 |
| | 17.5 | −35.78 | −71.7 | −6.47 | 0 | 0.76 | 0.41 | 1.75 | 1.42 | −1.58 | 0.25 |
| | 20 | −36.79 | −69.2 | −10.4 | 0 | 0.76 | 0.29 | 2.09 | 1.19 | −1.31 | 0.19 |

[a] $Tf(m)$ stands for $T_{f_A}^{(1)}$ (mode $m$).

TABLE VIII

TEMPERATURE COEFFICIENTS OF COUPLING AND THEIR ANGLE GRADIENTS. QUARTZ CUTS
$(YXwl)\varphi/\theta > 0°$ [a]

| Crystal cut | $\varphi$ | $\theta$ | $Tk_a$ | $Tk_b$ | $Tk_c$ | $\dfrac{\partial Tk_a}{\partial\theta}$ | $\dfrac{\partial Tk_b}{\partial\theta}$ | $\dfrac{\partial Tk_c}{\partial\theta}$ | $\dfrac{\partial Tk_a}{\partial\varphi}$ | $\dfrac{\partial Tk_b}{\partial\varphi}$ | $\dfrac{\partial Tk_c}{\partial\varphi}$ |
|---|---|---|---|---|---|---|---|---|---|---|---|
| | degrees | | | $10^{-6}/K$ | | | $10^{-6}/K$ deg $\theta$ | | | $10^{-6}/K$ deg $\varphi$ | |
| AT | 0 | 35.25 | — | — | 88.2 | — | — | 16.0 | 0 | 0 | 0 |
| 5° V | 5 | 34.94 | −192 | −183 | 89.1 | −1.81 | −27.5 | 15.9 | 0 | −1.17 | 2.45 |
| 10° V | 10 | 34.64 | −192 | −184 | 104 | −1.81 | −27.9 | 14.0 | −0.04 | −2.33 | 5.34 |
| 13.9 V | 13.90 | 34.40 | −191 | −188 | 127 | −1.83 | −28.8 | 10.9 | −0.05 | −3.34 | 8.22 |
| FC | 15 | 34.33 | −191 | −190 | 136 | −1.84 | −29.2 | 9.58 | −0.05 | −3.65 | 9.19 |
| IT | 19.10 | 34.08 | −191 | −200 | 181 | −1.87 | −31.5 | 1.39 | −0.06 | −5.04 | 13.6 |
| SC | 21.93 | 33.93 | −191 | −210 | 224 | −1.90 | −33.7 | −9.60 | −0.05 | −6.25 | 17.5 |
| 25° V | 25 | 33.72 | −191 | −225 | 290 | −1.94 | −36.9 | −32.6 | −0.04 | −8.01 | 22.1 |
| 30° V | 30 | 33.42 | −190 | −262 | 428 | −2.01 | −42.9 | −12.0 | −0.01 | −11.8 | 21.1 |
| LC | 11.17 | 9.39 | −157 | −93.9 | −138 | −0.87 | 3.14 | 7.85 | 0.17 | −2.81 | 5.89 |

[a] $T_{f_A}^{(1)} = 0$ for the $c$ mode of these cuts.

stiffened eigenvectors $\bar{\gamma}_m$ which determine the directions of particle displacement and enter the expressions for power flow, effective coupling constant, etc. For rotated Y cuts, the driven mode is uncoupled and has motion strictly along the digonal axis $X_1$. In general, the doubly rotated cut has particle motion out of the plane of the plate with consequent increased coupling to mounting supports and to the compressional mode in the ambient fluid. Both of these mechanisms will lead to increased loss. In order to show the displacements belonging to each mode in a simple and symmetrical fashion, we adopt the following conventions defining the displacement angles $\varphi_d^{(m)}$ and $\theta_d^{(m)}$ with respect to the plate $(X_i'')$ axes:

For mode $a$, which is predominantly thickness extensional, the displacement direction is that corresponding to $X_2''$ when it undergoes the rotations

$$(X_2''X_1''wl)\varphi_d^{(a)}/\theta_d^{(a)}. \tag{86}$$

For mode $b$, the fast quasi-thickness-shear mode, the displacement direction is that corresponding to $X_3''$ when it undergoes the rotations

$$(X_3''X_2''wl)\varphi_d^{(b)}/\theta_d^{(b)}. \tag{87}$$

For mode $c$, the slow quasi-thickness-shear mode, the displacement direction is that corresponding to $X_1''$ when it undergoes the rotations

$$(X_1''X_3''wl)\varphi_d^{(c)}/\theta_d^{(c)}. \tag{88}$$

TABLE IX

TEMPERATURE COEFFICIENTS OF COUPLING AND THEIR ANGLE GRADIENTS. QUARTZ CUTS
$(YXwl)\varphi/\theta < 0°$ [a]

| Crystal cut | $\varphi$ | $\theta$ | $Tk_a$ | $Tk_b$ | $Tk_c$ | $\dfrac{\partial Tk_a}{\partial \theta}$ | $\dfrac{\partial Tk_b}{\partial \theta}$ | $\dfrac{\partial Tk_c}{\partial \theta}$ | $\dfrac{\partial Tk_a}{\partial \varphi}$ | $\dfrac{\partial Tk_b}{\partial \varphi}$ | $\dfrac{\partial Tk_c}{\partial \varphi}$ |
|---|---|---|---|---|---|---|---|---|---|---|---|
| | degrees | | $10^{-6}/K$ | | | $10^{-6}/K$ deg $\theta$ | | | $10^{-6}/K$ deg $\varphi$ | | |
| BT | 0 | −49.20 | — | −444 | — | — | 5.57 | — | 0 | 0 | 0 |
| | 5 | −46.56 | −218 | −433 | 189 | 3.40 | 5.26 | −13.8 | −0.41 | −1.26 | 0.97 |
| | 10 | −38.63 | −197 | −402 | 115 | 2.81 | 4.91 | −7.25 | −0.84 | −2.33 | 3.21 |
| | 5 | −24.98 | −152 | −354 | −249 | 2.35 | −7.45 | −9.00 | −2.42 | −7.14 | −21.2 |
| | 10 | −32.23 | −180 | −372 | 84.0 | 2.58 | 4.63 | −2.26 | −1.27 | −1.23 | 11.2 |
| | 12.5 | −33.33 | −185 | −381 | 112 | 2.48 | 5.50 | 4.14 | −0.84 | −1.71 | 12.3 |
| RT | 15 | −34.50 | −190 | −393 | 136 | 2.42 | 6.69 | 7.75 | −0.50 | −1.95 | 11.8 |
| | 17.5 | −35.78 | −194 | −407 | 153 | 2.39 | 8.07 | 7.96 | −0.26 | −2.09 | 10.1 |
| | 20 | −36.79 | −196 | −421 | 168 | 2.36 | 9.92 | 7.79 | −0.09 | −1.86 | 8.61 |

[a] $T_{f_A}^{(1)} = 0$ for the $b$ mode of first three entries; for the $c$ mode of remainder.

Aside from symmetry, this choice of definitions for $\varphi_d^{(m)}$ and $\theta_d^{(m)}$ has the advantage of showing deviations from pure mode displacements for which both angles vanish. Figure 9 displays $|\varphi_d^{(m)}|$ as solid lines for all modes and $|\theta_d^{(m)}|$ as dashed lines along the locus of Eq. (85). The AT cut ($\varphi = 0°$) $c$ mode is pure, with the $a$ and $b$ modes coupled. As $\varphi$ increases, the out-of-plane displacements for the desired $c$ mode increase appreciably. Tables X and XI provide displacement angles for the selected cuts.
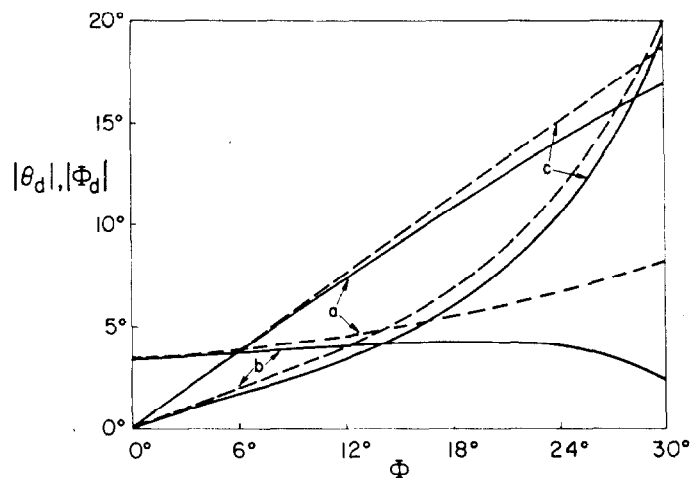


FIG. 9. Angles of particle displacement for quartz plates along the AT–SC locus of Fig. 5. Solid lines are for $|\varphi_d^{(m)}|$, and dashed for $|\theta_d^{(m)}|$.

TABLE X

PARTICLE DISPLACEMENT ANGLES AND MOTIONAL TIME CONSTANTS. QUARTZ CUTS $(YXwl)\varphi/\theta > 0°$ [a]

| Crystal cut | $\varphi$ | $\theta$ | $\|\varphi_d^{(a)}\|$ | $\|\varphi_d^{(b)}\|$ | $\|\varphi_d^{(c)}\|$ | $\|\theta_d^{(a)}\|$ | $\|\theta_d^{(b)}\|$ | $\|\theta_d^{(c)}\|$ | $\tau_1^{(a)}$ | $\tau_1^{(b)}$ | $\tau_1^{(c)}$ |
|---|---|---|---|---|---|---|---|---|---|---|---|
| | degrees | | degrees | | | degrees | | | femtoseconds | | |
| AT | 0 | 35.25 | 0 | 3.56 | 0 | 3.56 | 0 | 0 | 10.2 | 6.71 | 11.8 |
| 5° V | 5 | 34.94 | 3.04 | 3.78 | 1.46 | 3.87 | 1.66 | 3.14 | 10.3 | 6.73 | 11.8 |
| 10° V | 10 | 34.64 | 6.05 | 4.04 | 2.84 | 4.36 | 3.27 | 6.26 | 10.3 | 6.69 | 11.8 |
| 13.9° V | 13.90 | 34.40 | 8.36 | 4.23 | 4.12 | 4.88 | 4.76 | 8.69 | 10.4 | 6.62 | 11.8 |
| FC | 15 | 34.33 | 9.00 | 4.28 | 4.55 | 5.05 | 5.24 | 9.37 | 10.4 | 6.59 | 11.8 |
| IT | 19.10 | 34.08 | 11.3 | 4.37 | 6.60 | 5.76 | 7.49 | 11.9 | 10.5 | 6.46 | 11.8 |
| SC | 21.93 | 33.93 | 12.9 | 4.28 | 8.57 | 6.31 | 9.57 | 13.7 | 10.5 | 6.35 | 11.7 |
| 25° V | 25 | 33.72 | 14.5 | 3.95 | 11.5 | 7.01 | 12.6 | 15.6 | 10.6 | 6.21 | 11.7 |
| 30° V | 30 | 33.42 | 16.9 | 2.38 | 19.3 | 8.29 | 20.0 | 18.6 | 10.8 | 5.97 | 11.6 |
| LC | 11.17 | 9.39 | 6.33 | 23.6 | 27.9 | 20.4 | 27.5 | 4.40 | 11.6 | 9.70 | 10.8 |

[a] $T_{f_A}^{(1)} = 0$ for the $c$ mode of these cuts.

TABLE XI

PARTICLE DISPLACEMENT ANGLES AND MOTIONAL TIME CONSTANTS. QUARTZ CUTS $(YXwl)\varphi/\theta < 0°$ [a]

| Crystal cut | $\varphi$ | $\theta$ | $\|\varphi_d^{(a)}\|$ | $\|\varphi_d^{(b)}\|$ | $\|\varphi_d^{(c)}\|$ | $\|\theta_d^{(a)}\|$ | $\|\theta_d^{(b)}\|$ | $\|\theta_d^{(c)}\|$ | $\tau_1^{(a)}$ | $\tau_1^{(b)}$ | $\tau_1^{(c)}$ |
|---|---|---|---|---|---|---|---|---|---|---|---|
| | degrees | | degrees | | | degrees | | | femtoseconds | | |
| BT | 0 | −49.20 | 0 | — | 90.0 | 11.8 | 90.0 | 11.8 | 11.8 | 4.89 | 8.68 |
| | 5 | −46.56 | 7.51 | 21.7 | 24.0 | 12.5 | 80.6 | 13.3 | 11.9 | 5.06 | 8.81 |
| | 10 | −38.63 | 15.9 | 24.7 | 17.2 | 14.0 | 70.1 | 17.6 | 12.1 | 5.84 | 9.06 |
| | 5 | −24.98 | 12.9 | 6.78 | 13.0 | 17.8 | 69.2 | 13.9 | 15.2 | 7.27 | 6.36 |
| | 10 | −32.23 | 18.1 | 25.5 | 16.4 | 16.2 | 68.2 | 20.5 | 12.7 | 6.37 | 8.83 |
| | 12.5 | −33.33 | 19.3 | 29.8 | 12.2 | 14.6 | 64.6 | 20.3 | 12.3 | 6.46 | 9.13 |
| RT | 15 | −34.50 | 19.8 | 25.5 | 8.02 | 13.0 | 61.2 | 19.9 | 11.8 | 6.44 | 9.41 |
| | 17.5 | −35.78 | 19.7 | 22.0 | 3.98 | 11.4 | 58.0 | 19.3 | 11.5 | 6.42 | 9.68 |
| | 20 | −36.79 | 19.3 | 18.7 | 0.17 | 9.97 | 54.7 | 18.7 | 11.2 | 6.34 | 9.92 |

[a] $T_{f_A}^{(1)} = 0$ for the $b$ mode of first three entries; for the $c$ mode of remainder.

Also given in Tables X and XI are the motional time constants

$$\tau_1^{(m)} = \eta_m / \bar{c}_m,\tag{89}$$

where $\eta_m$ and $\bar{c}_m$ are obtained from Eqs. (21) and (17), respectively. Viscosity values of Lamb and Richter (1966) for room temperature have been used for

the calculations. The time constant is related to the resonator quality factor $Q_m$ by the relation

$$Q_m = 1/\omega_0 \tau_1^{(m)}, \tag{90}$$

with $\omega_0$ the nominal angular frequency of the mode; the relation of $\tau_1^{(m)}$ to the parameters of the equivalent electrical network will be discussed in Section VI,A. The loss represented by $\eta_m$ in Eq. (89) pertains solely to the bulk wave attenuation due to the crystal viscosity, and Eq. (90) hence gives the intrinsic $Q$ for each mode. To this will be added any other loss mechanisms such as that due to mounting of the plate and mode conversion losses due to surface features. The frequency–temperature curves along the $c$ mode locus of Eq. (85) may be constructed using the data of Tables I and VI plus Eq. (83). This is done in Fig. 10 for the case of the SC cut. From the graph it
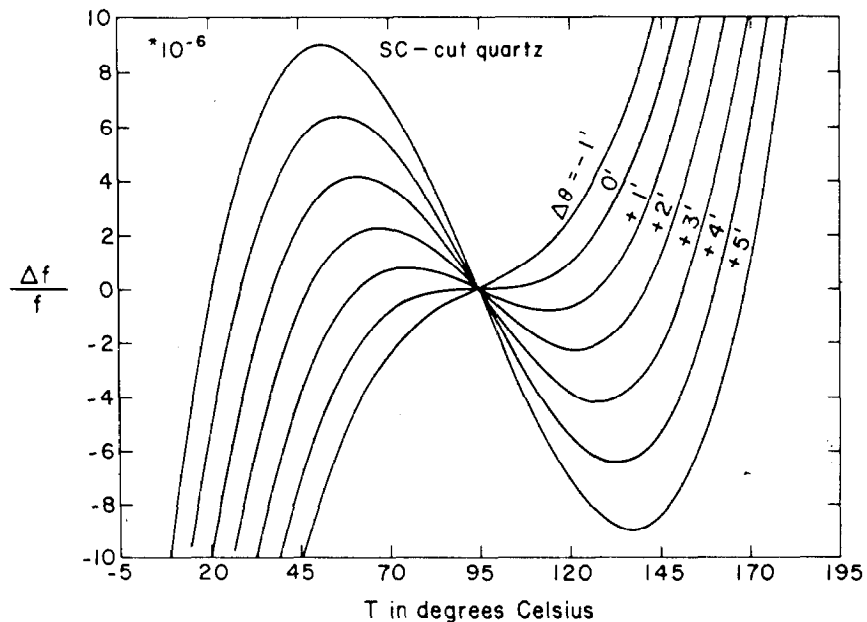


Fig. 10. Frequency–temperature characteristics for SC-cut quartz, as a function of variations in angle $\theta$. The lower turning point is convenient for oven-controlled applications, and is flatter than the corresponding AT cut at its upper turning point.

is apparent that this cut should be excellent for oven-controlled applications due to its high inflection temperature of 95.4°C; comparison with the corresponding AT-cut curves discloses that the SC cut is flatter than the AT cut and less sensitive to changes in $\theta$.

## 2. Nonlinear Effects in Quartz Resonators

A brief and qualitative account is given in this section of a number of effects whose explanations lie in the area of nonlinear elasticity (Thurston, 1964). Some of the effects are small in magnitude; but for high and even

medium precision quartz resonators, all constitute nonnegligible error budget entries. Although they are interrelated, the effects are grouped, for convenience, in four categories:

(a) initial stress and acceleration,
(b) nonlinear resonance and intermodulation,
(c) nonlinear mode coupling,
(d) dynamic thermal and film stress.

Recent theoretical predictions by Holland (1974) and EerNisse (1975) of doubly rotated quartz cuts exhibiting greatly reduced category d effects, followed by experimental confirmation (Kusters, 1976), will very probably have far-reaching consequences in opening up for detailed exploration and use multiply rotated cuts of quartz and other materials. Because the nonlinear effects listed above are related, one may minimize one effect by a choice of $\varphi$ and $\theta$ and expect that, by comparison to the standard AT cut, at least some of the other effects would simultaneously be reduced in size. Most applications will dictate a zero temperature coefficient requirement, so that the choice of angles follows the curves of Fig. 5. Experimental considerations indicate that the region of greatest interest is the $c$-mode locus for $\theta > 0°$ containing the FC, IT, and SC cuts, and along this locus is where we concentrate our attention. It is entirely possible that a second SC cut exists on the $\theta < 0°$ locus as well, along with an analogous SAW mode cut.

a. *Initial stress and acceleration effects.* In-plane diametric forces applied to the periphery of vibrating plates produce frequency changes that depend upon the azimuth angle $\psi$ in the plane of the plate. If $\psi$ is measured from the $X_1''$ axis, then it is found experimentally (Gerber and Miles, 1961) that for the AT cut the effect is zero at $\psi$ values of 60° and 120°. For the IT cut at $\varphi = 19.1°$, Ballato (1960) found the zeros to occur at $\psi = 85°$ and 163° with a maximum value only one-third that of the AT cut. This points to a reduced coefficient at the SC cut as well. Calculations for rotated Y cuts (Lee and Haines, 1974; Lee *et al.*, 1975) show excellent agreement with experiment.

Plate resonators subjected to acceleration fields experience distributed body forces in place of the concentrated edge loadings discussed above, but the effect is similar. Frequency shifts are comparable in both cases (order $10^{-9}$), and a factor ten improvement is needed in applications involving operation in shock and vibration environments. Work in this area has been carried out by Valdois *et al.* (1974) as well as by Lee and Wu (1976) with encouraging results.

b. *Nonlinear resonance and intermodulation effects.* The nonlinear resonance, or amplitude–frequency effect (Hammond *et al.*, 1963) pertains to the shape of the resonance amplitude versus frequency curve. Resonance

curves for linear systems with small loss will be symmetric; with nonlineari-
ties present, the curve is distorted by leaning toward higher or lower
frequencies. The AT cut leans toward higher frequencies, its effective stiffness
increasing with drive level, while the BT cut behaves in opposite fashion as a
soft spring. Indirect evidence indicates that the curve becomes symmetric in
the region between the FC and SC cuts, with a compensation of the nonlin-
earities taking place.[2] Figure 11 represents a typical surface for a hard
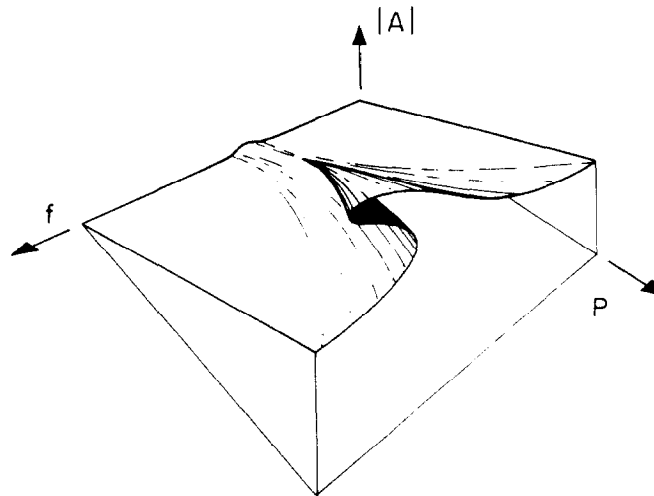


FIG. 11. Pleated surface depicting the frequency $(f)$, input power $(P)$, amplitude $|A|$
behavior of a nonlinear resonator with hard spring. AT cuts are representative; around the SC
cut the pleat disappears until much higher power levels are reached.

spring, with amplitude $|A|$ plotted as function of resonator frequency $f$ and
input power level $P$. Beyond a certain power level (normally in the micro-
watt range) the amplitude–frequency curve becomes distinctly asymmetric; at
still higher levels it ceases to become a single-valued function of frequency.
Advances in characterizing this important effect have been made by Gag-
nepain (1972). Tiersten (1976) has made a very accurate analysis of the
problem.

Closely related to the nonlinear resonance phenomenon is that of inter-
modulation, where energy supplied to a resonator at one frequency "spills
over" and appears at another frequency. This cross talk occurs with both
discrete resonator and monolithic filter (Spencer, 1972) structures. It is im-
portant in front-end filters and in adjacent channel filtering with transmit-
ters proximate to receivers. The effect appears due to nonlinearities

[2] This has been experimentally confirmed in cuts of orientation $\varphi = 21.93°, \theta = +34.11°$.
The resonators were planoconvex, of 1-diopter contour, and diameter 15 mm. They operated at
10 MHz, third harmonic. The lower turning points occurred at 72 $\pm$ 4°C (J. A. Kusters, private
communication, 1976).

associated with the bulk material as well as to surface features such as microcracks and microtwinning (Smythe, 1974; Tiersten, 1975b).

c. *Nonlinear mode coupling effects.* Anomalies in the frequency or admittance temperature characteristic of a resonator are called "activity dips" or "bandbreaks." They are generally conceded to be caused by various combinations of different modal frequencies coming into coincidence at particular temperatures because of differing temperature coefficients. The presence of activity dips is a persistent problem and necessitates a good deal of costly testing for medium and high precision resonator units. Doubly rotated cuts generally could be expected to have even more problems in this regard than AT cuts since they exhibit less symmetry and have, therefore, a more complicated mode spectrum when lateral boundaries are taken into account.

The modal interference that takes place may be linear or nonlinear. If the impressed voltage can drive the desired thickness mode and at the same time drive a harmonic of a flexural mode, e.g., then the vibrator admittance will reflect this fact as the linear superposition of the separate modal admittances. With temperature changes it is possible for the two resonance frequencies to cross and produce an anomaly. Linear activity dips have been described by Wood and Seed (1967) and by Fukuyo *et al.* (1967).

Nonlinear activity dips are less well understood and perhaps more important. Wood and Seed (1967) found the AT-cut fundamental thickness shear frequency to be affected by interfering modes at twice its frequency; Franx (1967) observed the same type of coupling due to a mode at three times the fundamental. Birch and Weston (1976) investigated both cases. Koga (1969) found the twenty-first harmonic of contour extension interfering nonlinearly with the thickness shear fundamental. Similar results were obtained by Fukuyo *et al.* (1967), who succeeded in measuring the temperature coefficients of a spectrum of interfering modes. In all cases the sensitivity of mode coupling to power levels is a characteristic of the nonlinearity. Hafner (1956) found that the anomalies encountered at the fifth and seventh harmonics were nonlinear in nature and depended on the electrode film as well as the quartz. This finding correlates with certain film stress results to be described in category d.

d. *Dynamic thermal and film stress effects.* Section IV discussed static frequency–temperature resonator characteristics; here transient thermal effects are reviewed. If an AT cut at thermal equilibrium experiences a small but abrupt temperature rise, the resonance frequency exhibits a sharp negative spike (order $10^{-7}/K$) followed by an asymptotic approach to its new equilibrium value (Warner, 1963). The BT cut behaves in opposite fashion. This dynamic thermal effect has been ascribed to thermal gradients, and explained on this basis by Holland (1974). He also disclosed (Holland, 1974, 1976) that the effect could be greatly reduced at the TS cut (thermal shock)

of orientation $(YXwl)\varphi \simeq 22.8°/\theta \simeq 34.3°$. The prediction was quickly verified (Kusters, 1976; Kusters and Leach, 1977) with the experimental TTC cut (thermal transient compensated) having angles $\varphi = 21.93°$, $\theta = 33.93°$. For crystals of this orientation, the thermal transient effect for the $c$ mode is reduced by a factor of more than one hundred, leading to promising applications for both fast warm-up oscillators and high precision frequency standards. It appears also possible that low cost temperature control could be provided for lower precision units by placing heating elements directly on the quartz surfaces.

The first actual disclosure of orientation angles for a doubly rotated cut having planar stress compensation was made by EerNisse (1975). This cut, designated the SC cut (stress compensated) is located at $(YXwl)\varphi \simeq 22.4°/\theta \simeq 34.3°$. The resonance frequencies of plates of this orientation are free from third-order elastic constant effects of mechanical stress bias, as would be caused by electrode films on the plate surfaces. It is no accident that the TS- and SC-cut orientations nearly coincide. Although the rationale in each case is different, the formulations are practically identical; they differ only in that electrode stresses are isotropic, whereas thermal stresses are not. Both problems are one-dimensional. Because "stress compensated" is a more general phrase, we choose to use it indifferently for the general family of cuts TS/TTC/SC in the neighborhood of which one or more planar stress effects are minimized. The acceleration problem mentioned in a is one-dimensional, and could also reasonably be expected to be improved for SC cuts. The influence of mechanical stress bias caused by electrode films may be seen from the experiments of Warner and may be related to Hafner's (1956) discovery of their role in causing activity dips. Warner (1963) investigated frequency transients caused by sudden temperature changes applied to resonators plated conventionally as well as to resonators plated for lateral field excitation. In the latter units the frequency spike was drastically reduced, probably because the most active central area of the resonator was devoid of plating, as is necessary for lateral field excitation. These results are discussed by Gerber and Sykes (1974). Another example of film stress bias is demonstrated by the experiments of Filler and Vig (1976), who used patches of electrobonded nickel applied diametrically at the periphery of circular AT-cut resonators to study the azimuthal dependence. Their results are similar to the azimuthal behavior found for the edge force effect, with frequency change replaced by apparent orientation angle shift.

The problem of aging, or long-term frequency drift, depends upon a number of causative factors, and electrode stress must be included among them. As electrode films relax slowly in time, the resonator frequency will similarly change, unless the cut is stress-compensated. Fortunately, for the SC cuts, the locus of zero stress sensitivity is nearly perpendicular to the

locus of zero temperature coefficient, so these may be adjusted virtually independently (EerNisse, 1976). The static frequency–temperature behavior of these cuts has been presented in Fig. 10. It is adjusted by slight changes in $\theta$; the stress coefficient is altered by changes in $\varphi$.

### 3. Summary of Advantages and Disadvantages of Doubly Rotated Quartz Cuts

We conclude the discussion of quartz resonators by summarizing the current status of pros and cons of doubly rotated resonators with orientations on the $\theta > 0°$ branch of the zero temperature coefficient locus. In all cases the comparison is with respect to an AT cut having the same frequency and electrode area. The doubly rotated cut in question usually lies in the neighborhood of the SC cut, although in some instances the data at present are too fragmentary to permit more than an indication of the orientation of optimal behavior.

*Advantages*

*Lessened edge force sensitivity.* The IT cut has about one-third the magnitude of the AT cut. This is of importance in shock and vibration environments.

*Reduced acceleration sensitivity.* One order of magnitude improvement is presently needed.

*Improved amplitude–frequency behavior.* This is of importance for high precision oscillators.

*Lessened intermodulation effects.* This is required for filters.

*Fewer activity dips.* Nonlinear elastic constants are compensated, reducing mode couplings.

*Greatly improved transient frequency–temperature behavior.* Two or three orders of magnitude improvement is found. This is important for fast warm-up oscillators.

*Greatly improved planar stress behavior.* Electrode film relaxation is a long-term aging factor that would be virtually eliminated. It is probable that current low aging crystals achieve their low aging behavior due to compensating aging processes. An SC cut fabricated using standard AT-cut cleaning procedures would probably show higher aging because the film component would be absent (J. R. Vig, private communication, 1976). Ultraclean procedures would nearly eliminate the contamination process and would lead the way to ultralow aging units.

*Improved static frequency–temperature behavior.* Inflection temperature is increased; frequency deviation is decreased. For high precision oven-controlled applications, operation at the inflection temperature or at the lower turning point is more stable than at the AT-cut upper turning point.

*Thicker, less fragile plates; slightly improved quality factors.*

*Increased capacitance ratio.* (See Section VI.) High precision applications call for reducing the influence of external circuitry to a minimum to maintain a good noise figure. Data on FC cuts indicate improvements in phase noise.

*Disadvantages*

*More complex unwanted mode spectra.* Additional contouring or bevelling restraints are imposed; suitability for filter use is potentially impaired.

*Proximity and strength of b mode.* At the SC cut the undesired *b* mode is nearly of equal strength with the useful *c* mode, and about 10% above it in frequency. Additional circuitry is required to suppress the *b* mode in some applications; in others, proper contouring reduces its strength adequately.

*Larger out-of-plane displacements.* There are increased mounting losses with attendant $Q$ degradation. Proper contouring can improve this situation.

*Increased capacitance ratio and motional resistance.* An increased ratio is an advantage in certain high precision applications, but is a drawback for temperature-compensated crystal oscillators (TCXOs) of the fast warm-up variety and for monolithic filters (Spencer, 1972).

*Orienting and X raying doubly rotated cuts more difficult.* The relatively strong $12\bar{3}1$ plane at $\varphi = 19.10°$, $\theta = +16.57°$ used for locating the IT cut can also be used for the SC cut.

*Tighter $\varphi$, $\theta$ tolerances required.* Most physical and electrical properties are more sensitive to angle misorientations when $\varphi > 0°$. For AT cuts, most quantities of interest have zero $\varphi$ derivatives, so departures in $\varphi$ are manifested only in second order.

The last two disadvantages are manufacturing considerations that will largely be obviated by new technology such as microprocessor control. Remaining entries are intrinsic and stem from the double rotation that lowers the plate symmetry from monoclinic to triclinic. Theoretical analyses are also rendered more difficult. The advantages enumerated arise largely from compensation of nonlinear effects. Additional considerations are given by Ballato and Iafrate (1976). At present there are insufficient data comparing AT and doubly rotated cuts with regard to ease of obtaining required surface finish, impurity migration rates, and X-ray/neutron resistance and recovery.

Additional work on doubly rotated orientations in quartz and other crystals is needed particularly in the areas of calculating the dispersion curves and developing approximate plate theories of various orders. These tasks have been carried out for piezoelectric crystals with monoclinic symmetry by Lee and Syngellakis (1975), and Syngellakis and Lee (1976). The study of static stress effects and acceleration sensitivity in triclinic plates is also of pressing interest, and measurement of the higher order piezoelectric

and dielectric constants (Besson, 1974) is needed to fill in portions of the nonlinear treatments.

An additional nonlinear mechanism sufficiently large in quartz to cause discrepancies in high precision applications is the polarizing effect (Hruška and Kazda, 1968; Kusters, 1970; Hruška, 1971; Baumhauer and Tiersten, 1973; Tiersten, 1975a). In this effect (order $10^{-12}$ m/V) bias or stray electric fields produce changes in the effective elastic, piezoelectric, and dielectric material constants. The largest changes in quartz take place in the elastic constants, but the coefficient happens to vanish for the driven mode in rotated Y cuts. For doubly rotated cuts in general, the effect will be present. Ungrounded units used in probes, or in vibrators subject to oscillator circuitry biases, are susceptible but can be protected in a simple manner (J. A. Kusters, private communication, 1976).

## B. ALUMINUM PHOSPHATE

Aluminum phosphate, $AIPO_4$, also known as berlinite, is a material in crystal class 32 very like quartz in structure and physical properties. It occurs naturally only as tiny crystals, but may be grown to large size by the hydrothermal method (Stanley, 1954). An early determination of the elastic and piezoelectric constants was reported by Mason (1950). More recent work by Chang and Barsch (1976) disclosed the presence of zero temperature coefficient thickness modes; zero coefficient SAW cuts have also been found (Carr and O'Connell, 1976, Jhunjhunwala *et al.*, 1976).

Using the recently determined material constants and temperature coefficients of Chang and Barsch (1976), Fig. 12 shows the calculated frequency constants $N_m = v_m/2$, the coupling factors $|k_m|$, and antiresonance temperature coefficients $T^{(1)}_{f_{m\Lambda}}$ for doubly rotated cuts $(YXwl)\varphi/\theta$, $\varphi = 0°(6°)30°$, and $|\theta| \leq 90°$. The similarity to Fig. 6 is readily apparent. Frequency constants for berlinite are somewhat lower; the coupling factors are roughly double that of quartz, and the temperature coefficients are very much the same. Degeneracy of the *b* and *c* modes takes place at $(YXl)\theta \simeq -24.5°$.

For plates $(YXw)\varphi$, as $\varphi$ varies from 0° to 30°, $|k_a|$ rises almost linearly from 0 to 16%; $|k_b|$ arcs from 0 to 11% and back to 0%, while $|k_c|$ falls nearly linearly from 24 to 0%.

The loci of $T^{(1)}_{f_{m\Lambda}} = 0$ for $m = b$, *c* are shown in Fig. 13. From Fig. 12 it is seen how shallow the $T^{(1)}_f$ surfaces are, particularly for $\varphi > 12°$. Small changes in the values of the measured constants could therefore affect the loci in Fig. 13 appreciably. For this reason, it is not appropriate to pursue more detailed calculations of angle gradients, etc., at this time. On the basis of current information, berlinite appears particularly attractive for mono-
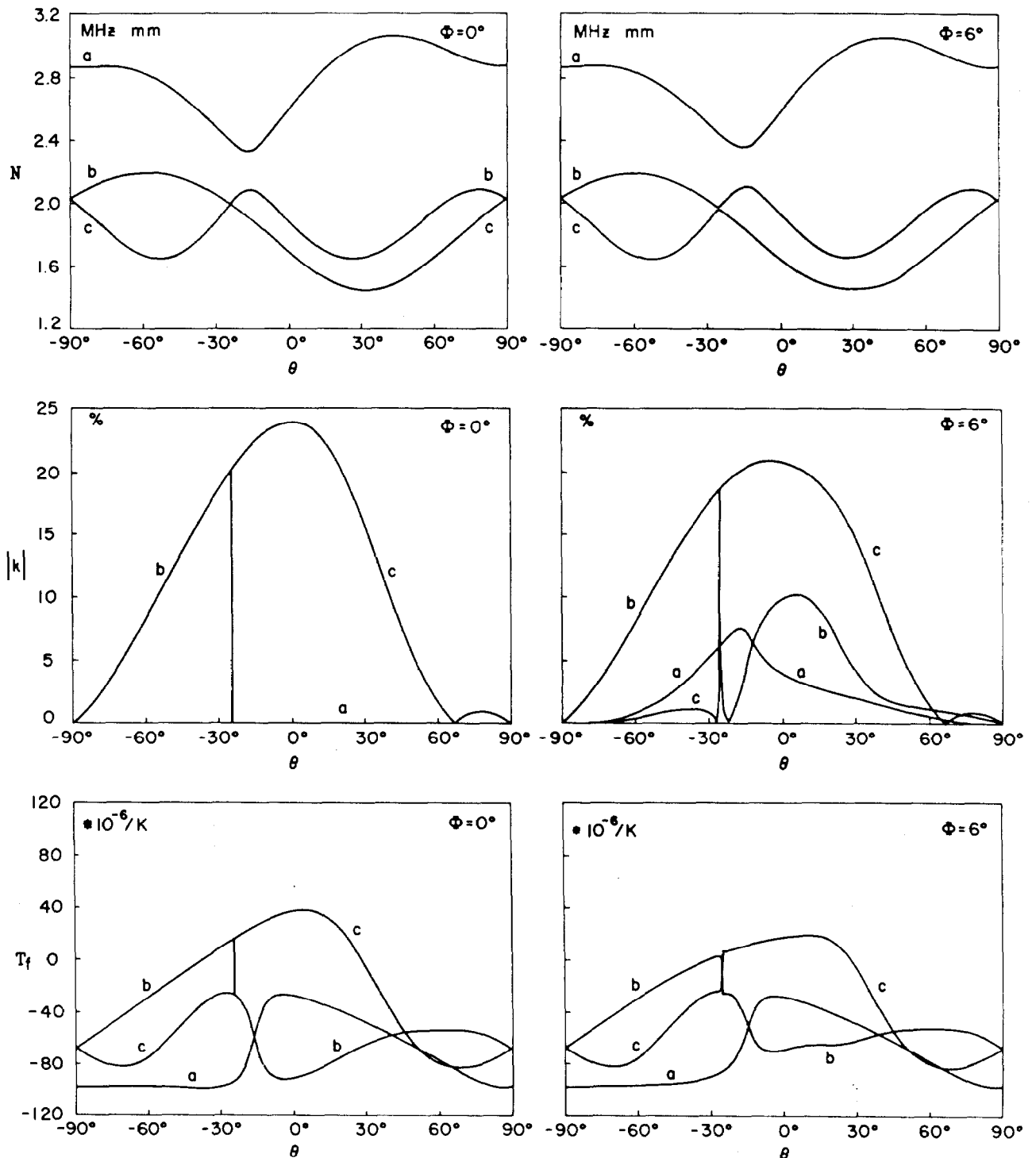
FIG. 12. Thickness mode properties of doubly rotated cuts of aluminum phosphate. Frequency constants $N$ are in MHz mm, coupling factors are in percent, and temperature coefficients $T_{f_\lambda}^{(1)}$ are in $10^{-6}/K$.

lithic (Tiersten, 1969) and wider band conventional filters and for SAW applications. Additional measurements of the higher order temperature coefficients and the nonlinear elastic constants would be most desirable.
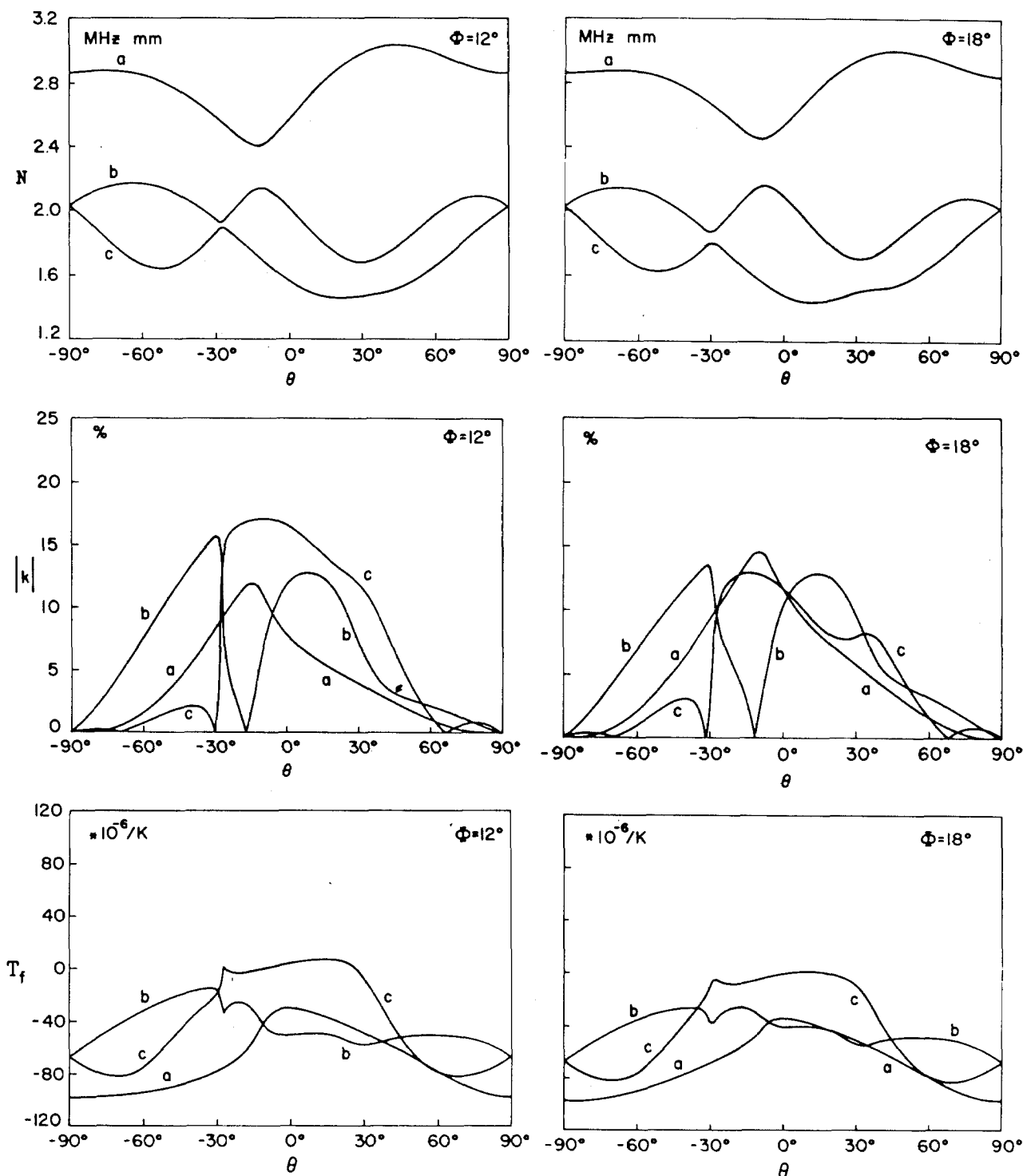
FIG. 12—*continued*

## C. LITHIUM TANTALATE

Lithium tantalate and lithium niobate (discussed in Section V,D) are refractory oxides in crystal class 3*m*. A thorough investigation of their elastic, piezoelectric, and dielectric properties, including first and second
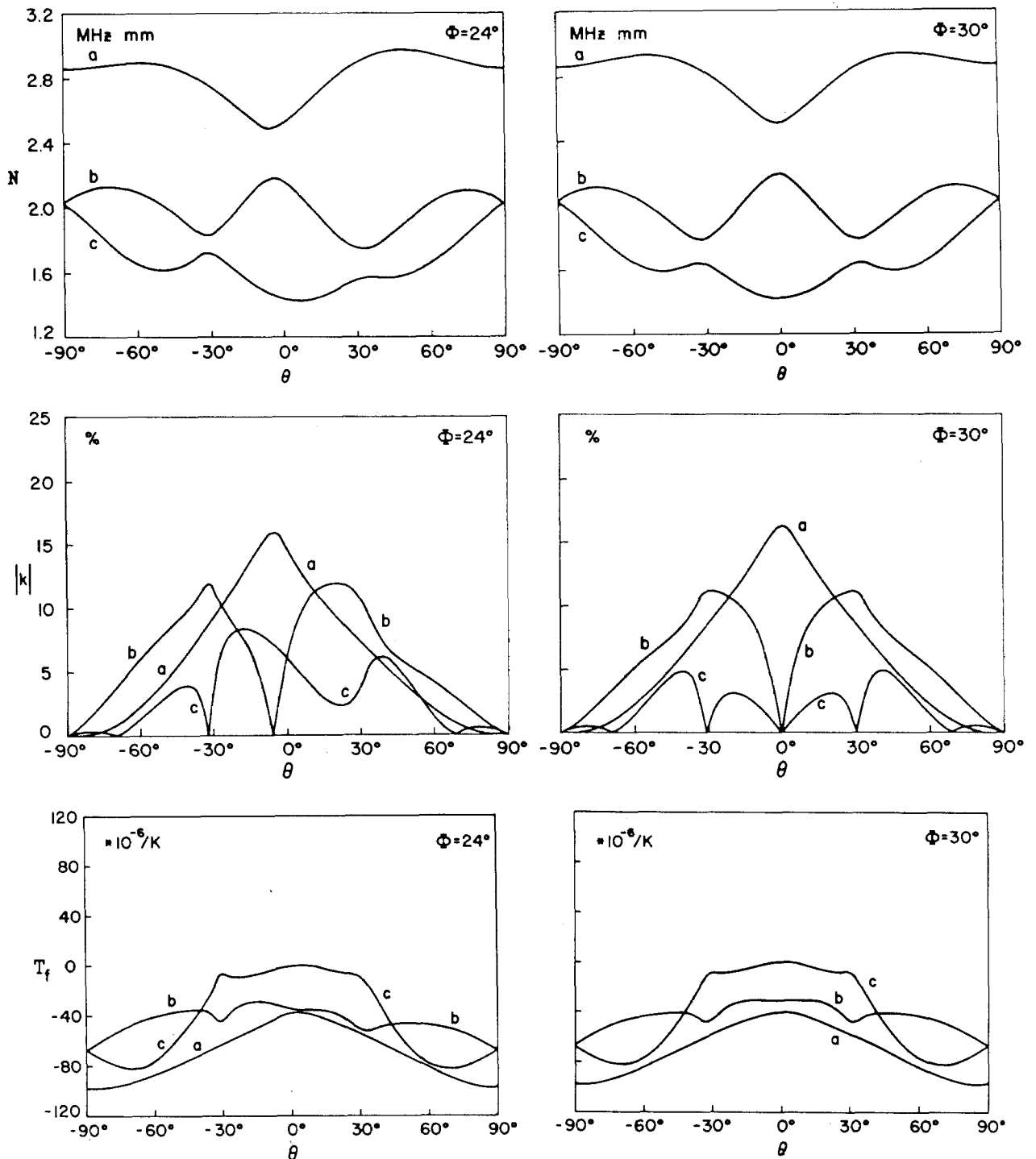
FIG. 12—*continued*

order temperature coefficients, was made by Smith and Welsh (1971). More recently. Détaint and Lançon (1976) investigated doubly rotated thickness modes of the tantalate and constructed altitude charts of coupling and temperature coefficients. In Fig. 14 are shown $N_m$, $|k_m|$ and $T_{fmA}^{(1)}$ for lithium
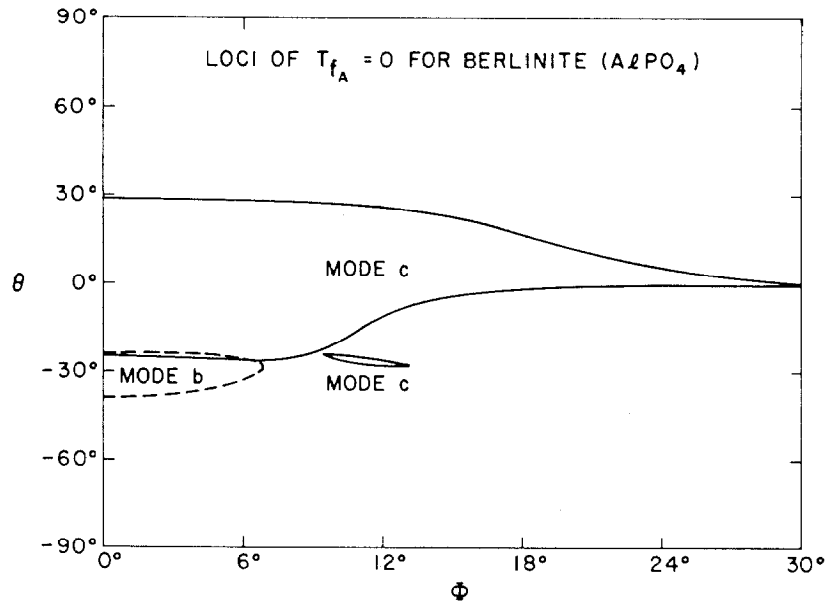
FIG. 13. Loci of zeros of first order temperature coefficient of antiresonance frequency in aluminum phosphate. Note the similarity to Fig. 5.

tantalate cuts $(YXwl)\varphi/\theta$, $\varphi = 0°(6°)30°$, and $|\theta| \leq 90°$. These have been computed using the data of Smith and Welsh (1971) with $e_{33}$ taken from Warner *et al.* (1967) as suggested by Détaint and Lançon (1976). Points of accidental degeneracy of the $b$ and $c$ modes occur for cuts $(YXl)\theta \simeq -29.9°$, $+26.9°$, and $37.8°$.

Whereas quartz possesses a digonal axis of symmetry, $3m$ crystals have a mirror plane (Juretschke, 1974; Nye, 1957); taking this normal to the $X_1$ axis causes the elastic constants with indices 15, 16, 25, 26, 35, 36, 45, and 46 to vanish along with the piezoelectric constants with indices 11, 12, 13, 14, 25, 26, 35, and 36. Some of the differences between the 32 and $3m$ symmetries may be seen by a comparison of Fig. 14 with Fig. 6 or 12 for the case $\varphi = 30°$. For example, when $\theta = 0°$ for class $3m$ and when $|\theta| = 90°$ for class 32, $|k_a|$ is zero, while both $|k_b|$ and $|k_c|$ are finite; when $\theta = 0°$ for class 32 and when $|\theta| = 90°$ for class $3m$, $|k_a|$ is finite, while both $|k_b|$ and $|k_c|$ vanish. Also, for rotated Y cuts, the pure shear mode in class 32 is the only one piezoelectrically driven, while it is undriven in class $3m$, and the quasi-extensional and quasi-shear modes are driven instead. For lithium tantalate plates $(YXw)\varphi$, as $\varphi$ varies from $0°$ to $30°$, $|k_a|$ decreases from 21 to $0\%$; $|k_b|$ rises from 33 to $42.5\%$; and $|k_c|$ rises from $0\%$ to a shallow maximum of $2.5\%$ at $\varphi = 11°$ and levels off to $2\%$.

Because of the large piezoelectric coupling constants, the difference between the resonance and antiresonance fundamental frequencies is relatively large, as is the difference between their respective temperature coefficients. In Fig. 15 are given the loci of the zeros of $T_{f_A}^{(1)}$ and $T_{f_R}^{(1)}$ versus
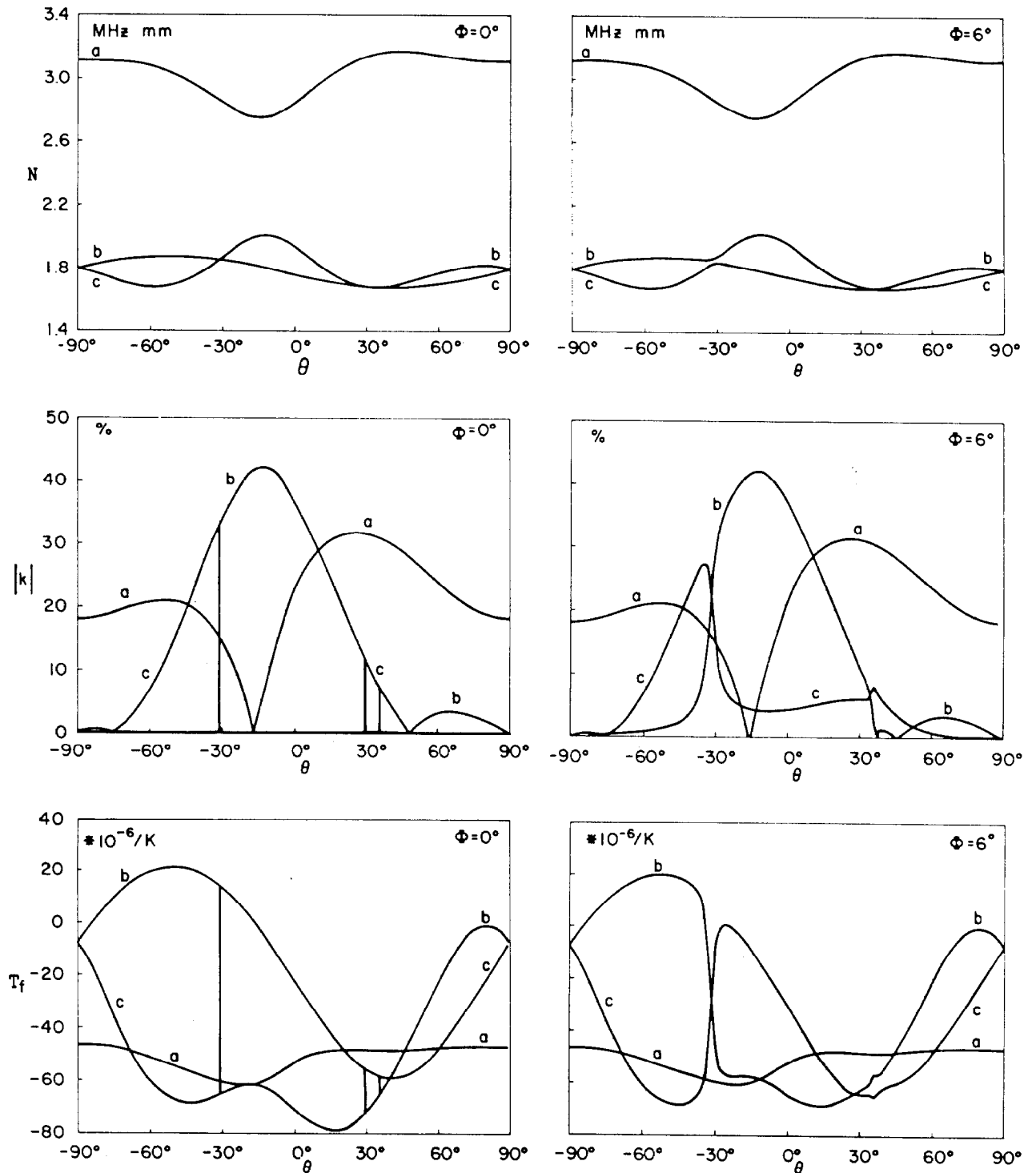
FIG. 14. Thickness mode properties of doubly rotated cuts of lithium tantalate. Frequency constants $N$ are in MHz mm, coupling factors are in percent, and temperature coefficients $T_{f_\lambda}^{(1)}$ are in $10^{-6}/K$.
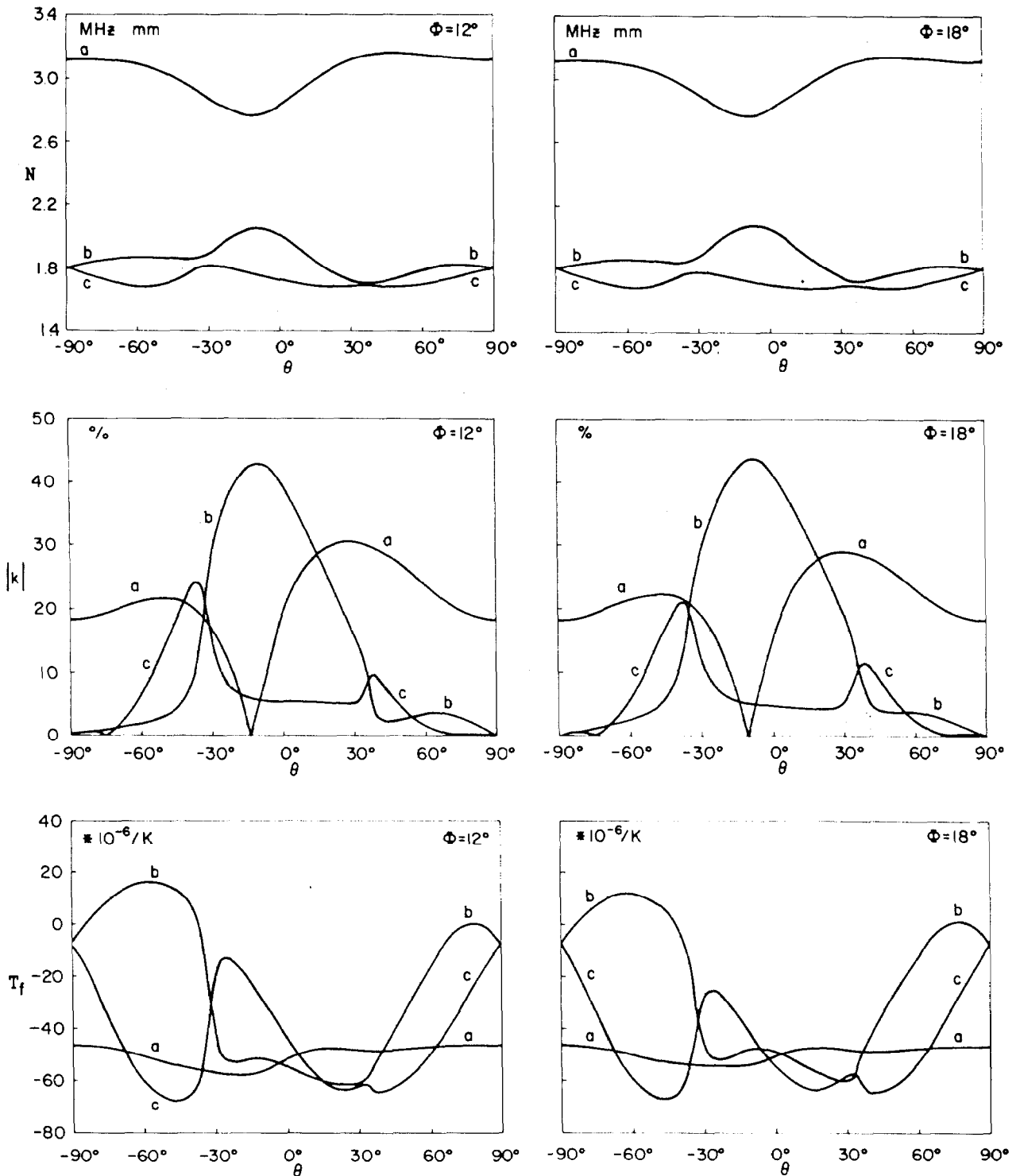
FIG. 14—*continued*

$\varphi$, $\theta$ for modes $b$ and $c$, from Détaint and Lançon (1976). Mode $a$ has no zero temperature coefficient. The curves are for $M = 1$; changing $M$, or using a series load capacitor $C_L$ will shift the $T_{f_R}^{(1)}$ loci toward the invariant $T_{f_A}^{(1)}$ loci. The $b$-mode resonance frequency loop for $\varphi > 15°$ has no corre-
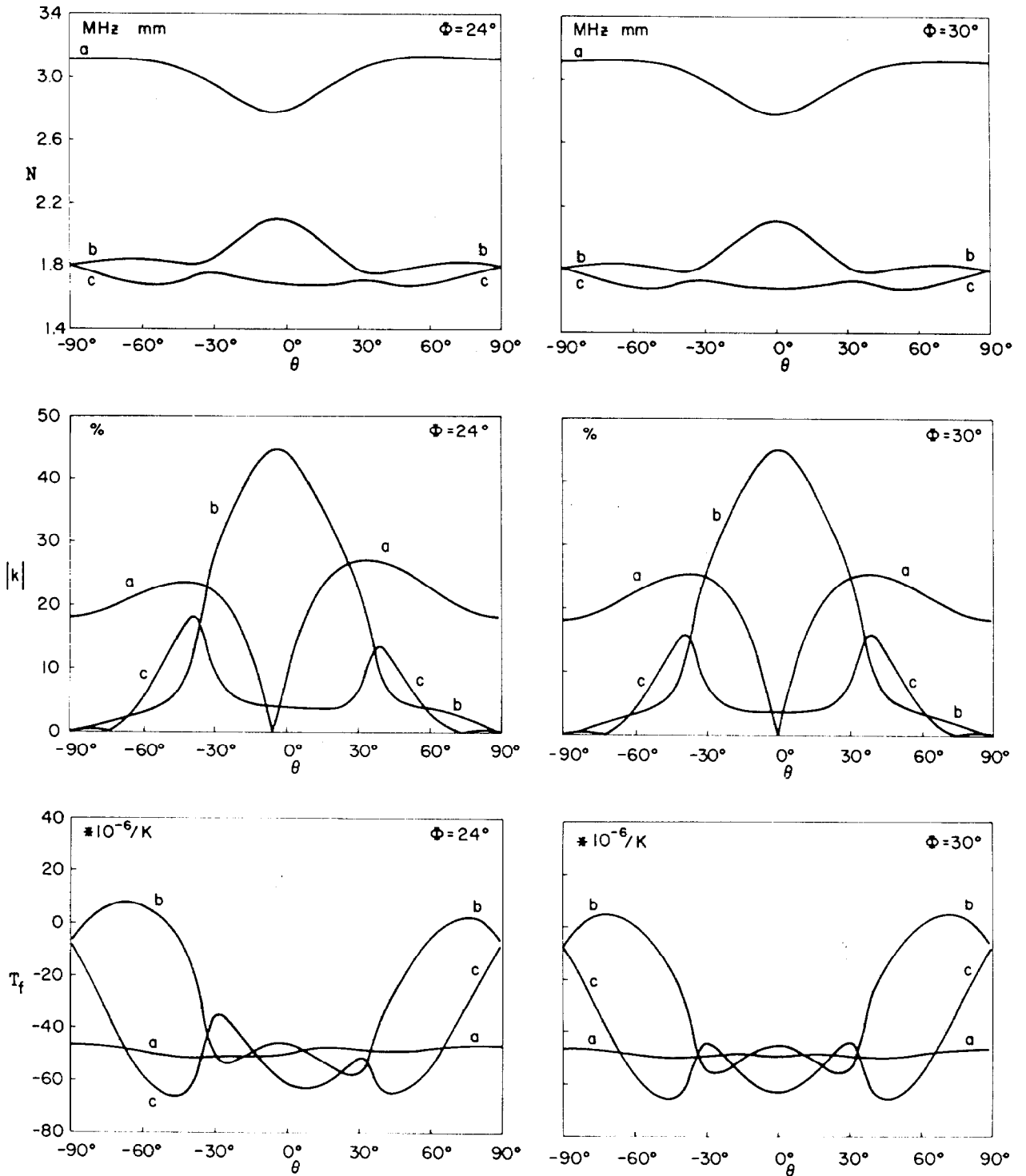
sponding $T_{f_A}^{(1)}$ curve; it occurs in the region of maximum $|k_b|$. An altitude chart of $|k_b|$ in percent, from Détaint and Lançon (1976), is shown in Fig. 16. When $\varphi = 0°$, $|k_b|$ vanishes for $-90° \leq \theta \leq -29.9°$, and for $+26.9° \leq \theta \leq +37.8°$. Altitude charts of the fundamental resonance
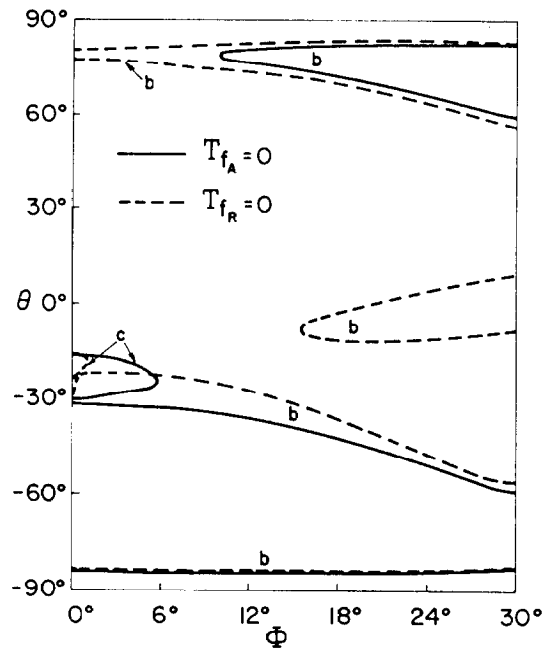
FIG. 15. Loci of zeros of first order temperature coefficients in lithium tantalate. Solid lines are for antiresonance frequencies; dashed are for resonance frequencies. All curves are for the fundamental harmonic. (After Détaint and Lançon, 1976).
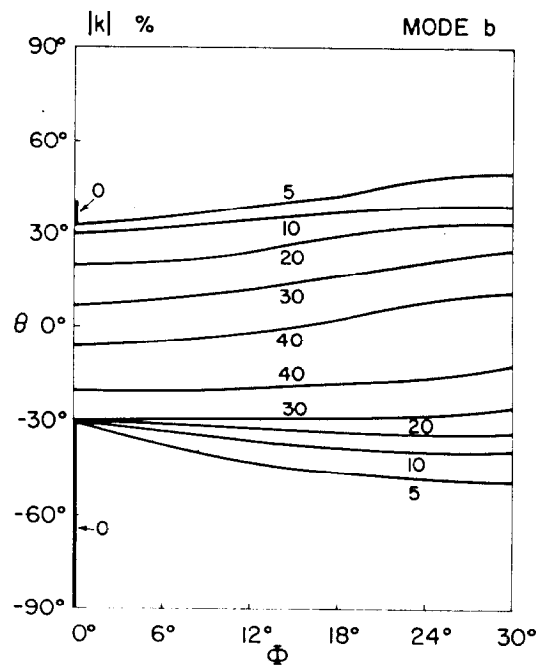
FIG. 16. Piezoelectric coupling coefficients for the *b* mode in lithium tantalate. (After Détaint and Lançon, 1976).

frequency constants, defined as in Eq. (41) with $f_R$ substituted for $f_{mA}^{(M)}$, are given by Détaint and Lançon (1977).

The presence of a zero temperature coefficient locus in lithium tantalate for the fundamental and harmonics of the $b$ and $c$ modes, simultaneously with large piezoelectric coupling values, indicates excellent filter device potential. Three of the practical areas of work remaining for this material are: investigation of higher order temperature behavior $T_f^{(3)}$; measurement of the nonlinear elastic and piezoelectric constants with determination of possible "SC cuts"; computation of dispersion diagrams for doubly rotated orientations for both open- and short-circuited boundary conditions, and application of these spectra to the design of monolithic filters and other devices. Exact and approximate dispersion curves for these electrical conditions have already been determined for rotated Y cuts of LiTaO$_3$ (Lee and Syngellakis, 1975; Syngellakis and Lee, 1976).

## D. Lithium Niobate

The data of Smith and Welsh (1971) have been used to compute the frequency constants $N_m$, piezoelectric coupling factors $|k_m|$, and first order temperature coefficients $T_{f_{mA}}^{(1)}$ for lithium niobate. Figure 17 presents the results for doubly rotated cuts $(YXwl)\varphi/\theta$, $\varphi = 0°(6°)30°$, $|\theta| \leq 90°$. Degeneracy of the $b$ and $c$ modes takes place for cuts $(YXl)\theta$, $\theta \simeq +24.1°$, $+48.9°$, and $+59.0°$. For plates $(YXw)\varphi$, as $\varphi$ varies from $0°$ to $30°$, $|k_a|$ decreases slowly from 31 to 0%; $|k_b|$ rises from 57 to 69%, and $|k_c|$ rises slowly from 0 to 7%. There are no orientations having $T_{f_{mA}}^{(1)}$ values greater than $-40 \times 10^{-6}/K$; the main advantage of this material for piezoelectric applications is its suitability for transducer use owing to large $|k|$ values. Wideband filter applications are also possible.

## VI. Electrical Characteristics of Plate Vibrators

The use of mechanical vibrators as undamped resonant elements for frequency control and as acoustic transducers has led to their representations as equivalent electrical circuits (Mason, 1948). This section gives expressions for the lumped equivalent circuit parameters of thickness mode plate vibrators with traction-free boundaries, obtained from the exact relation for input admittance. In terms of these parameters, values are given for doubly rotated quartz plates. Also provided are data on mode spectra for a variety of quartz cuts, showing the influences of multimode couplings.

### A. Lumped Equivalent Circuit Parameters

Crystal vibrators are usually represented in the vicinity of a single resonance by an electrical circuit consisting of a shunt capacitance $C_0$ in
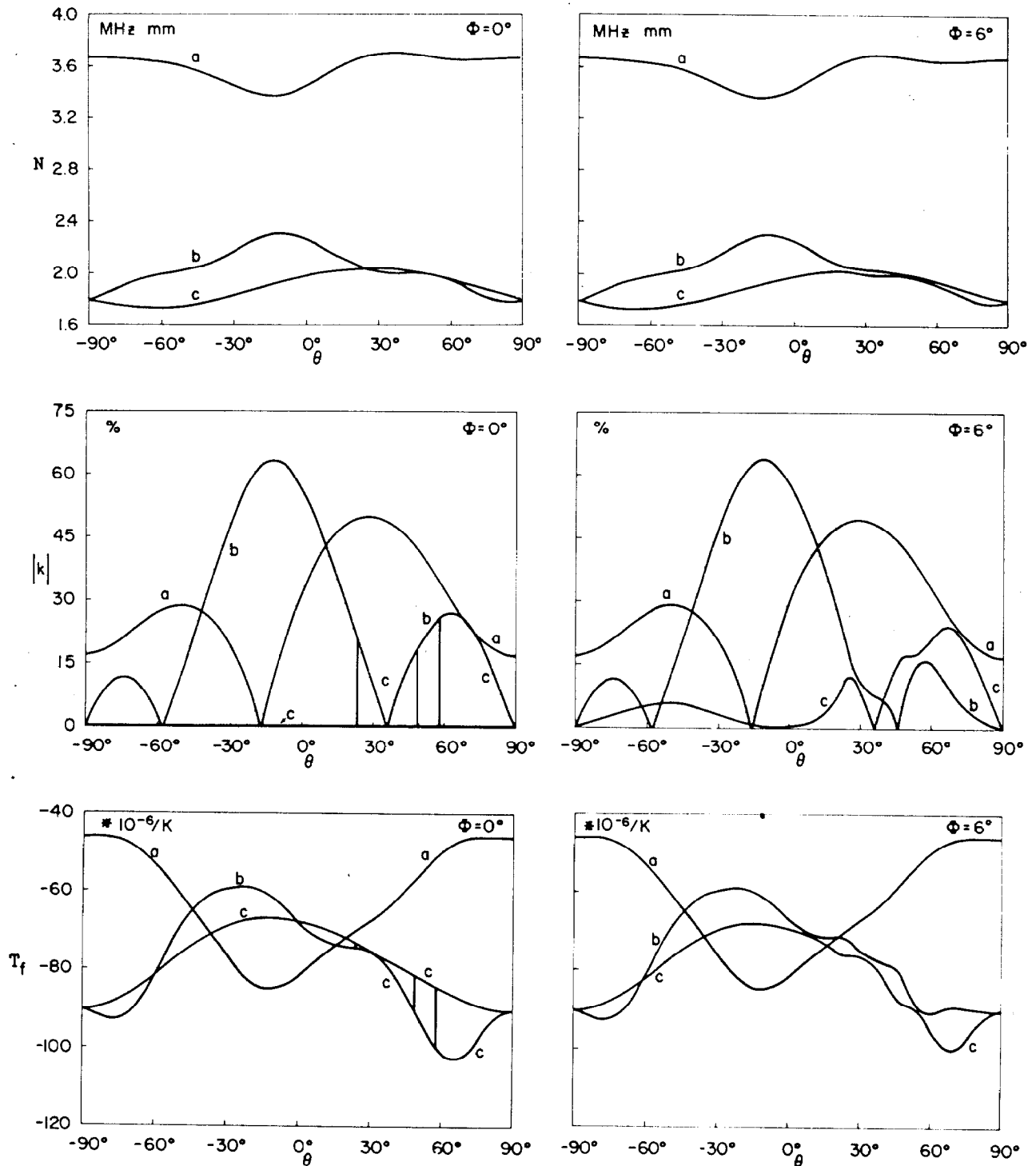
FIG. 17. Thickness mode properties of doubly rotated cuts of lithium niobate. Frequency constants $N$ are in MHz mm, coupling factors are in percent, and temperature coefficients $T_{f_A}^{(1)}$ are in $10^{-6}/K$.

parallel with a series $C_1$, $R_1$, $L_1$ chain (Mason, 1948). Reduction to this form starts from Eqs. (38) and (40). It is convenient to discuss the lossless case first, and to deal with a single mode. When Eq. (38), written for a single
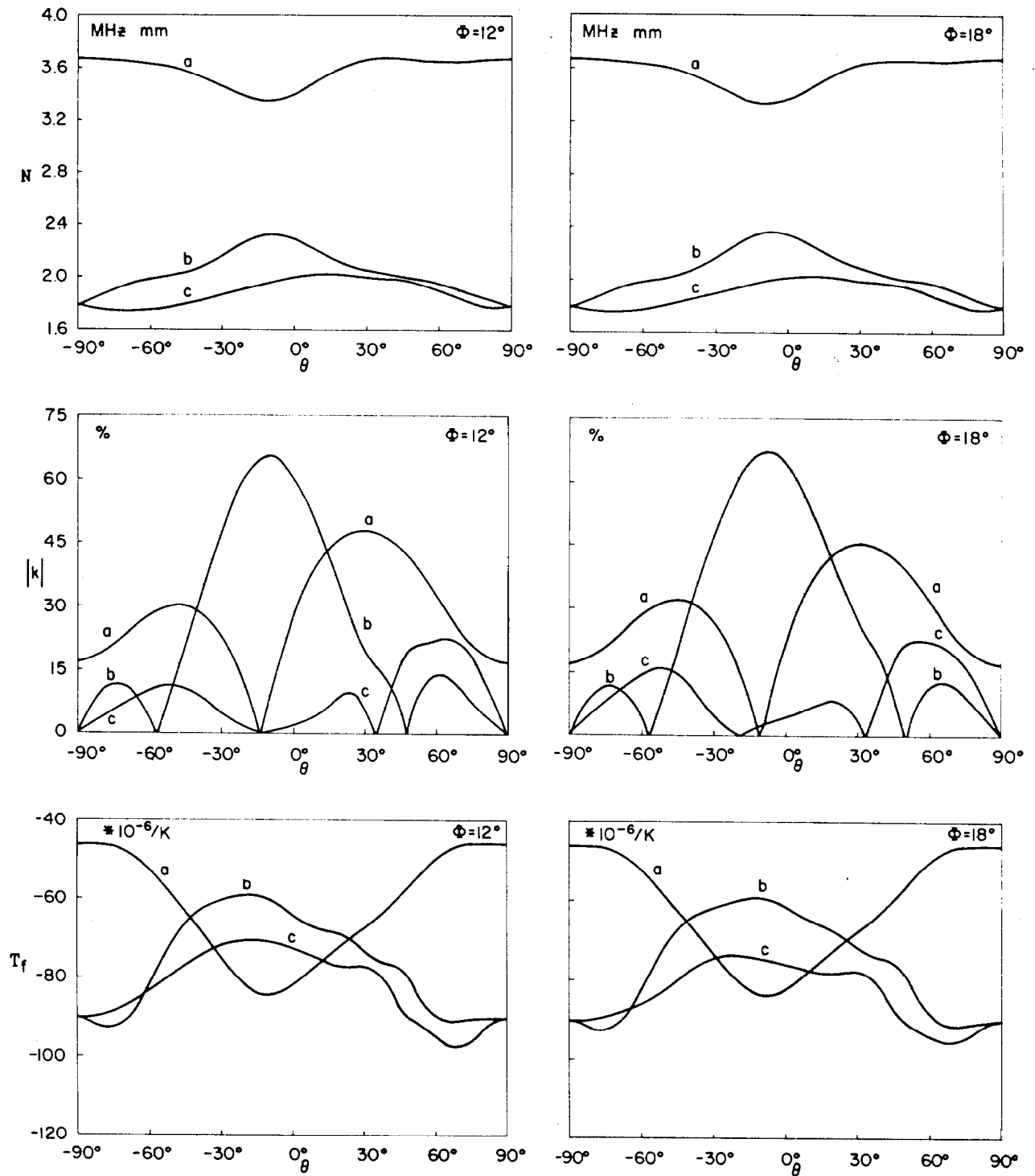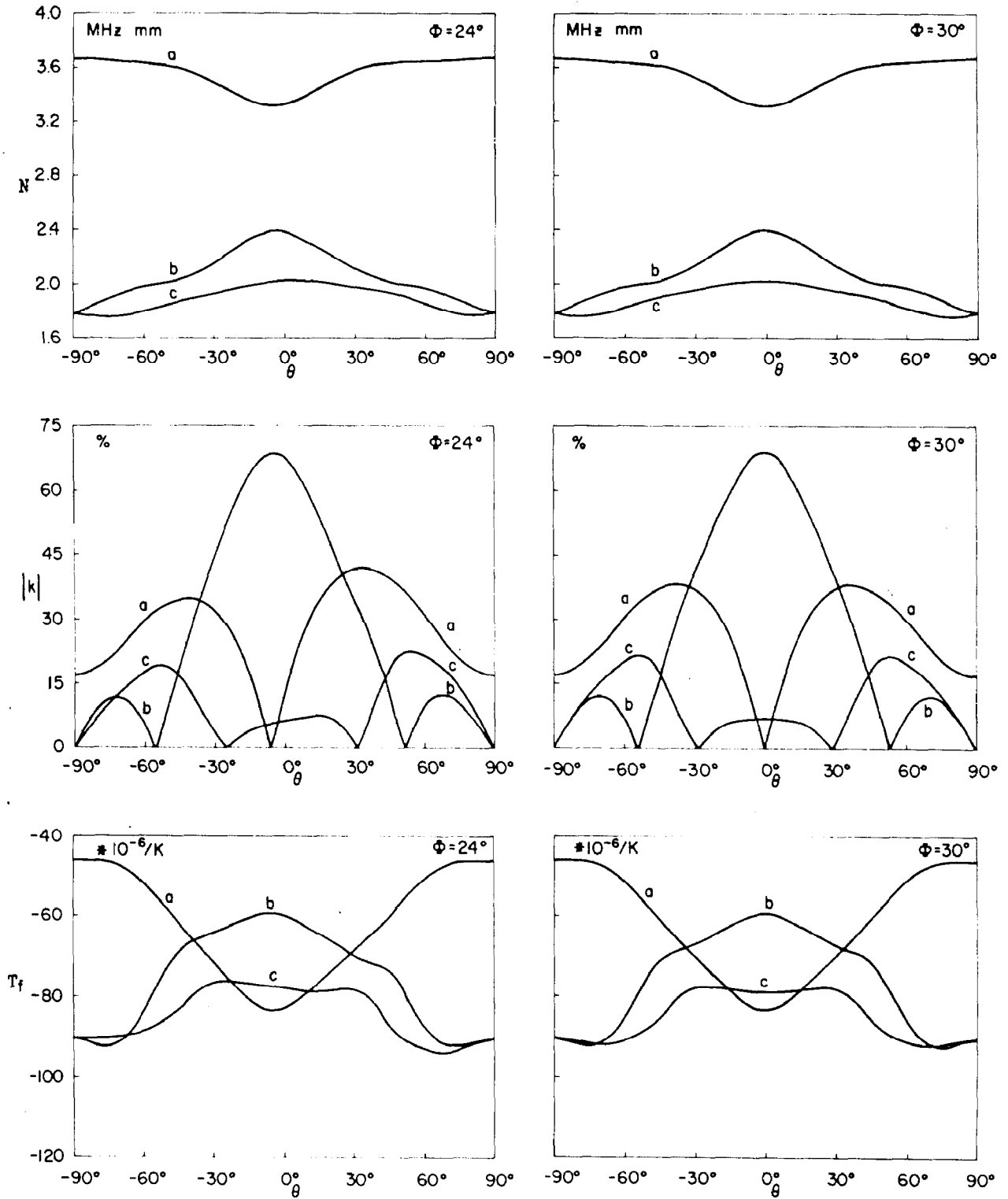
FIG. 17—*continued*

FIG. 17—*continued*

mode, has subtracted from it the immittances corresponding to a shunt capacitor $C_0$, followed by a series capacitor $-C_0$, the remaining admittance is

$$Y_{TL} = j\omega C_0 k^2 \tan X/X. \tag{91}$$

Expansion of the tangent function in partial fractions leads to a network realization of the individual terms as series $LC$ circuits; $Y_{TL}$ is then just the shunt connection of these series branches. Each series branch consists of an inductance of constant value

$$L' = h^2/2C_0 k^2 v^2 \tag{92}$$

and a capacitance that depends on the harmonic $M$

$$C'_M = 8C_0 k^2/\pi^2 M^2. \tag{93}$$

$M$ is an odd integer, and $v$ is obtained from Eq. (19). The complete and exact circuit for a single lossless mode is then a shunt capacitor $C_0$, followed by a series capacitor $-C_0$, followed in turn by an infinite number of parallel branches each consisting of a series $L'C'_M$ chain (Onoe and Jumonji, 1967). Loss is incorporated by adding to each $L'C'_M$ chain a resistance $R'_M$ of value

$$R'_M = \tau_1/C'_M = \pi^2 M^2 \eta h/4e^2 A. \tag{94}$$

The piezoelectric constant $e$ is given by Eq. (39), and the viscosity $\eta$ by Eq. (21). Motional capacitance ratios $r'_M$ are

$$r'_M = C_0/C'_M = \pi^2 M^2/8k^2. \tag{95}$$

In order to obtain the simple four-element circuit described earlier, valid in the vicinity of a single resonance, the influences of both the series negative capacitor and of the shunt harmonic branches $L'C'_M$ must be taken into account. We assume all shunt branches resonating above the branch of interest are represented as capacitors, and those below are represented as open circuits. Then the elements of the equivalent circuit become

$$\bar{C}_0 = C_0/F, \tag{96}$$

$$L = L'F^2, \tag{97}$$

$$C_M = C_0/r_M. \tag{98}$$

In Eqs. (96)–(98)

$$F = 1 - k^2 I, \tag{99}$$

$$I = 1 - 8\Sigma'/\pi^2, \tag{100}$$

$$\Sigma' = \sum_{K < M} K^{-2} \quad (K, M \text{ odd}), \tag{101}$$

$$r_M = r'_M F - 1. \tag{102}$$

With loss included $R_M$ becomes

$$R_M = R'_M F^2.\tag{103}$$

The four-element circuit conventionally used thus consists of $R_M$, $L$, and $C_M$ connected in series, all shunted by $\bar{C}_0$; in the limit of small $k$ these may be replaced by $R'_M$, $L'$, $C'_M$, and $C_0$, respectively. Extension of the foregoing to more than one mode is straightforward, but usually not warranted. Equation (91) then consists of one term for each mode represented; the realization for each mode is the same as in the single mode case, with the infinite shunt branches in parallel. Reduction to a four-element network then follows. Temperature coefficients of the circuit elements are readily obtained from the material in Section IV and the defining Eqs. (92)–(103).

The piezoelectric coupling factors in quartz are not large, and the capacitance ratios $r_m$ for each mode $m$ can be obtained separately from Eq. (95). From Eqs. (43), (59), and (62) it follows that the fractional difference between antiresonance and resonance frequencies is approximately $1/2r_M$ for each mode; and from Eq. (71) it is seen that $G_0 \simeq 1/r_M$. Capacitance ratios are therefore important quantities in oscillator and filter design. For doubly rotated quartz cuts on the locus of Eq. (85), the ratios $r_m$ for $m = a$, $b$, $c$ are given in Fig. 18 for the fundamental harmonic $M = 1$. At the SC cut the $c$-mode ratio is about three times that of the AT cut. Tables XII and XIII list
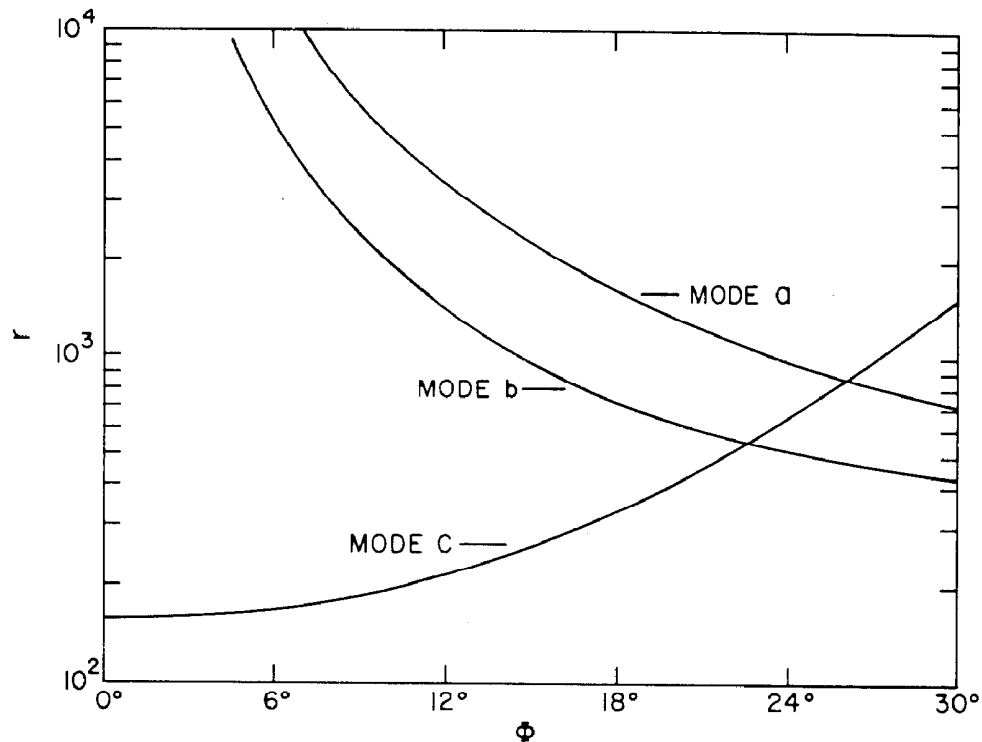


FIG. 18. Capacitance ratios for doubly rotated quartz cuts along the AT-SC locus of Fig. 5.

TABLE XII

CAPACITANCE RATIOS AND THEIR ANGLE GRADIENTS. QUARTZ CUTS $(YXwl)\varphi/\theta > 0$ [a]

| Crystal cut | $\varphi$ | $\theta$ | $r_a$ | $r_b$ | $r_c$ | $\dfrac{\partial r_a}{\partial\theta}$ | $\dfrac{\partial r_b}{\partial\theta}$ | $\dfrac{\partial r_c}{\partial\theta}$ | $\dfrac{\partial r_a}{\partial\varphi}$ | $\dfrac{\partial r_b}{\partial\varphi}$ | $\dfrac{\partial r_c}{\partial\varphi}$ |
|---|---|---|---|---|---|---|---|---|---|---|---|
| | degrees | | $10^{+2}$ | | | $10^{+2}/\deg\theta$ | | | $10^{+2}/\deg\varphi$ | | |
| AT | 0 | 35.25 | — | — | 1.59 | — | — | 0.11 | — | — | 0 |
| 5° V | 5 | 34.94 | 191 | 74.3 | 1.66 | 11.2 | 14.7 | 0.10 | −75.5 | −28.8 | 0.04 |
| 10° V | 10 | 34.64 | 48.1 | 19.3 | 1.94 | 2.80 | 3.73 | 0.09 | −9.27 | −3.36 | 0.09 |
| 13.9° V | 13.90 | 34.40 | 25.4 | 10.7 | 2.41 | 1.49 | 1.97 | 0.06 | −3.38 | −1.18 | 0.16 |
| FC | 15 | 34.33 | 22.0 | 9.45 | 2.60 | 1.29 | 1.71 | 0.05 | −2.68 | −0.92 | 0.19 |
| IT | 19.10 | 34.08 | 14.1 | 6.59 | 3.68 | 0.83 | 1.12 | −0.09 | −1.26 | −0.40 | 0.35 |
| SC | 21.93 | 33.93 | 11.1 | 5.55 | 4.96 | 0.65 | 0.90 | −0.35 | −0.82 | −0.23 | 0.55 |
| 25° V | 25 | 33.72 | 8.95 | 4.84 | 7.31 | 0.53 | 0.73 | −1.07 | −0.53 | −0.13 | 0.92 |
| 30° V | 30 | 33.42 | 6.90 | 4.19 | 14.9 | 0.42 | 0.55 | −5.39 | −0.27 | −0.06 | 1.80 |
| LC | 11.17 | 9.39 | 11.9 | 2.11 | 1.46 | 0.50 | −0.002 | 0.01 | −2.08 | −0.06 | 0.15 |

[a] $T_{f_A}^{(1)} = 0$ for the $c$ mode of these cuts.

values of $r_m$ and their angle derivatives for selected quartz cuts. Note that the AT cut value of 159 given is for a laterally unbounded plate with a uniform distribution of motion over the plate surface area. This value is a lower bound; in practice, values in the range 180–210 are usually encountered. To account for the nonuniform amplitude distribution, Bechmann (1952) introduced a factor $\Psi$ equal to the quotient of the square of the surface integral

TABLE XIII

CAPACITANCE RATIOS AND THEIR ANGLE GRADIENTS. QUARTZ CUTS $(YXwl)\varphi/\theta < 0$ [a]

| Crystal cut | $\varphi$ | $\theta$ | $r_a$ | $r_b$ | $r_c$ | $\dfrac{\partial r_a}{\partial\theta}$ | $\dfrac{\partial r_b}{\partial\theta}$ | $\dfrac{\partial r_c}{\partial\theta}$ | $\dfrac{\partial r_a}{\partial\varphi}$ | $\dfrac{\partial r_b}{\partial\varphi}$ | $\dfrac{\partial r_c}{\partial\varphi}$ |
|---|---|---|---|---|---|---|---|---|---|---|---|
| | degrees | | $10^{+2}$ | | | $10^{+2}/\deg\theta$ | | | $10^{+2}/\deg\varphi$ | | |
| BT | 0 | −49.20 | | 3.90 | | | −0.27 | | | 0 | |
| | 5 | −46.56 | 92.2 | 3.47 | 302 | −11.4 | −0.22 | −19.1 | −33.2 | 0.08 | −120 |
| | 10 | −38.63 | 13.6 | 2.72 | 55.3 | −1.22 | −0.12 | −1.09 | −1.60 | 0.12 | −10.6 |
| | 5 | −24.98 | 11.8 | 1.64 | 6.31 | −0.78 | 1.18 | −18.0 | −3.71 | 0.49 | −5.91 |
| | 10 | −32.23 | 7.99 | 2.12 | 55.4 | −0.61 | −0.07 | 1.20 | −0.84 | 0.11 | −8.70 |
| | 12.5 | −33.33 | 7.04 | 2.50 | 38.0 | −0.52 | −0.09 | 1.68 | −0.45 | 0.13 | −4.48 |
| RT | 15 | −34.50 | 6.98 | 3.01 | 27.0 | −0.49 | −0.12 | 1.39 | −0.26 | 0.15 | −2.68 |
| | 17.5 | −35.78 | 6.90 | 3.54 | 20.6 | −0.50 | −0.15 | 0.89 | −0.14 | 0.18 | −1.80 |
| | 20 | −36.79 | 7.19 | 4.21 | 16.0 | −0.52 | −0.20 | 0.57 | −0.04 | 0.22 | −1.28 |

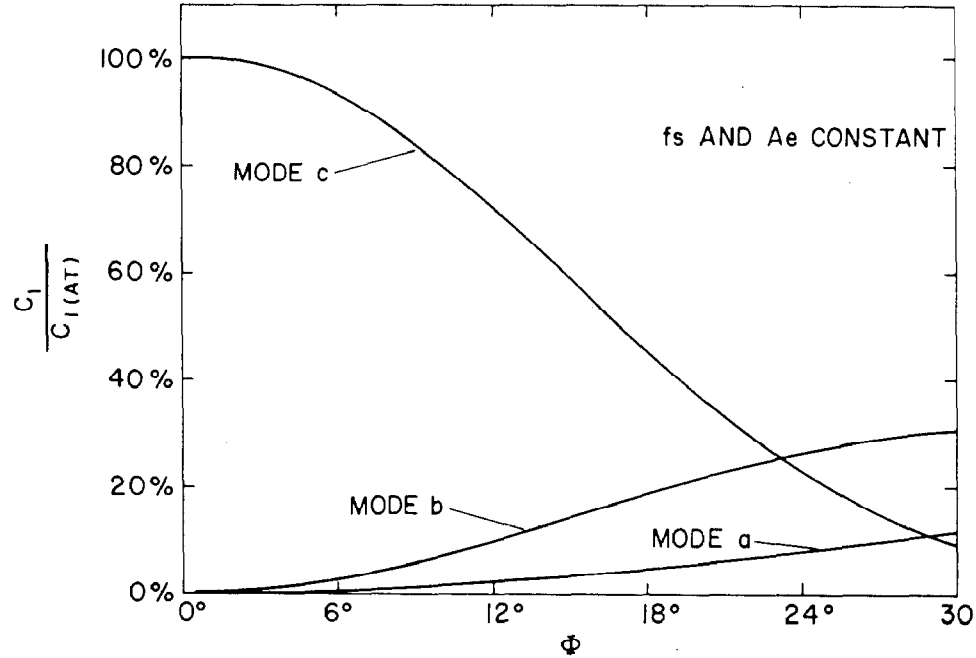[a] $T_{f_A}^{(1)} = 0$ for the $b$ mode of first three entries; for the $c$ mode of remainder.

FIG. 19. Motional capacitances for doubly rotated quartz cuts along the AT-SC locus of Fig. 5, normalized to that of an AT cut having identical electrode area and frequency.

of the normalized amplitude function by the surface integral of its square. This factor, which is less than or equal to one, multiplies $C_M$ and divides $L$ and $R_M$ to produce effective values. This approximate technique can be applied to doubly rotated cuts if the motional distribution is known for a given design; alternatively, one may derive more accurate expressions for any resonator geometry by using variational methods (Tiersten, 1969; Holland and EerNisse, 1969; Lee and Haines, 1974).

Motional capacitance $C_M$ is proportional to electrode area and to fundamental frequency. Considering these to be fixed, we can determine the value of $C_M$ normalized to that of the AT-cut $c$ mode. For the locus of Eq. (85), the result is plotted in Fig. 19 from the harmonic-independent relation

$$\frac{C_M}{C_{M(AT)}} = \frac{C_1}{C_{1(AT)}} = \frac{\left(\varepsilon_\zeta^S / r^{(m)} N_m\right)}{\left(\varepsilon_\zeta^S / r^{(c)} N_c\right)_{AT}}. \tag{104}$$

Since in crystals of trigonal symmetry $\varepsilon_\zeta^S$ does not depend on angle $\varphi$ and the zero temperature coefficient locus is nearly a constant in $\theta$, the permittivities in Eq. (104) are virtually equal and the variations in Fig. 19 result from changes of coupling factor and modal velocity. The ratios shown will moreover hold well for finite plates since $\Psi$ will be approximately constant for both the AT and doubly rotated plate, and will cancel in the quotient. Utilizing Eq. (94) plus the foregoing makes it possible to plot the ratio of the

motional resistances along the locus; the results are given in Fig. 20. The
results are similar to those in Fig. 19, but they depend, additionally, on the
variations in $\tau_1^{(m)}$ with position on the locus. The same remark concerning
finite plates holds here also. If $C_0$ is maintained constant, rather than elec-
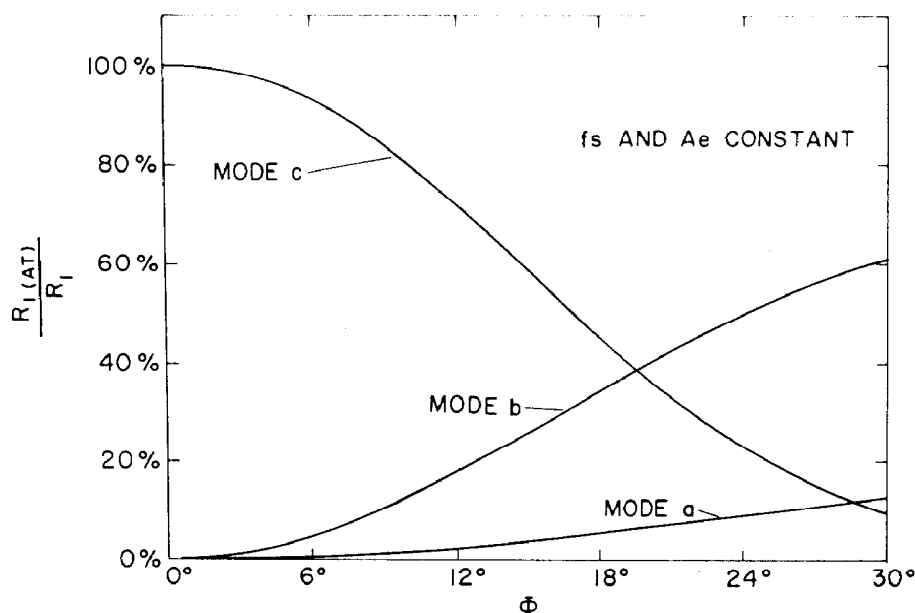trode area and fundamental frequency, the resistance ratio curve for the $c$



FIG. 20. Motional resistances for doubly rotated quartz cuts along the AT-SC locus of
Fig. 5, reciprocally normalized to that of an AT cut having identical electrode area and
frequency.

mode remains virtually unaltered; the $b$-mode curve is raised from about 60
to 75% at $\varphi = 30°$, while the $a$-mode curve rises to 25% at $\varphi = 30°$.

## B. MODE SPECTROGRAPHS

Mode spectrographs are plots of resonator input susceptance versus
frequency. Often measured in practice is a quantity proportional to the
resonator plate susceptance when the shunt capacitance $C_0$ has been bal-
anced out, e.g., by a bridge. We have plotted this quantity $B_R$ normalized to
the susceptance $B_0$ of the shunt capacitance in Fig. 21 for the FC cut of
quartz at $\varphi = 15°$. The ordinate is found from

$$\left| \frac{B_R}{B_0} \right| = \left| \sum_m k_m^2 \frac{\tan X^{(m)}}{X^{(m)}} \right| \bigg/ \left| 1 - \sum_m k_m^2 \frac{\tan X^{(m)}}{X^{(m)}} \right|. \tag{105}$$

The abscissa is percentage frequency offset from the $c$-mode fundamental
antiresonance frequency. Figure 21 is plotted for the lossless case, but both
resonances are marked with a figure in percent to indicate the response level
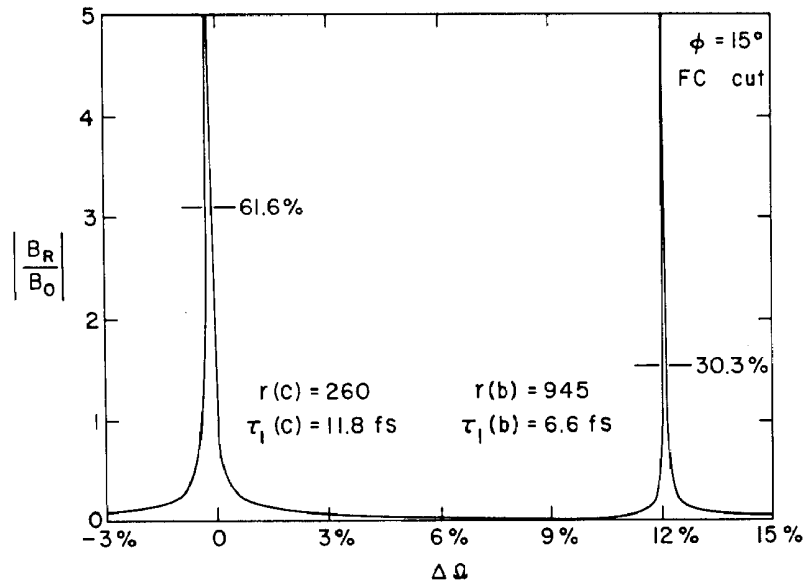when losses are present, compared to the AT-cut $c$-mode fundamental reso-

FIG. 21. Mode spectrograph for an FC-cut quartz resonator, showing proximity of $b$ and $c$ modes. Indicated on each resonance curve is the ratio of mode height, when loss is included, to that of an AT cut.

nance. The relative levels are given by

$$(r_1^{(c)}\tau_1^{(c)})_{\text{AT}}/(r_M^{(m)}\tau_1^{(m)}). \tag{106}$$

Table XIV contains a list of modal parameters for additional cuts on the locus of Eq. (85); the entry $|B_R/B_0|$ denotes the maximum value. From this table one can visualize the shifting modal strengths and separations of the spectrographs with changing $\varphi$. In Fig. 22 is given a wider frequency plot for the SC cut. The ordinate is in decibels relative to the $b$-mode fundamental. Normalized frequency is the abscissa; the modes and their harmonics are labeled by the notation $m^{(M)}$. One sees the cluttering of the spectrum produced by the three series of harmonics. These are only the thickness modes; in practice, each mode will have associated with it anharmonic overtones due to lateral phase reversals across the plate, further crowding the spectrum. Contouring can reduce these effects very much. More important in many respects are the strength and proximity of the $b$- and $c$-mode fundamental resonances. Here contouring can reduce the $b$-mode strength somewhat, but the separation remains fixed.

When thin flat plates are required to have clean mode spectra, e.g., high frequency filter crystals and crystals for fix-tuned oscillators, the required amount of mode spectral purity is achieved by control of the electrode geometry. According to energy trapping considerations (Shockley et al., 1967), optimal suppression of unwanted responses occurs when the electrode diameter to plate thickness ratio times $M \cdot \sqrt{\mu}$ equals $K_M$, a constant. For
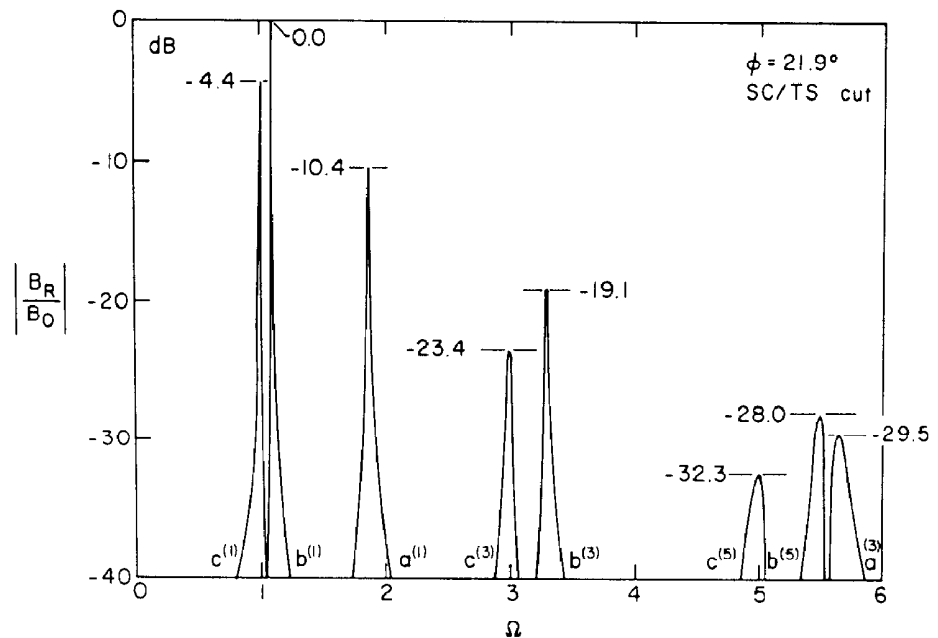
FIG. 22. Extended frequency spectrograph of an SC-cut resonator. Mode levels are normalized to the $b$-mode fundamental strength. Modes are labeled with superscript harmonic numbers. The ordinate scale is in decibels.

$M = 1$, $K_M$ ranges from 1.8 to 2.4; $K_M = 1.8$, 1.6, and 1.4 for $M = 3, 5$, and 7, respectively, for AT-cut quartz. Strictly speaking, the electrode patch can be longer in one direction than in the other, and the best shape is nearly an ellipse (Mindlin, 1968). For SC-cuts, similar considerations appear to apply, with the possibility of even larger $K_M$. Spectra nearly devoid of

TABLE XIV

MODAL PARAMETERS OF SELECTED QUARTZ RESONATOR CUTS[a]

| Cut | Mode $b$ | | | Mode $c$ | | | Mode separation |
|---|---|---|---|---|---|---|---|
| | $r$ | $\tau_1$ | $|B_R/B_0|$ | $r$ | $\tau_1$ | $|B_R/B_0|$ | |
| AT | $\infty$ | 6.7 | 0 | 159 | 11.8 | 100 | 14.4 |
| 13.9° V | 1071 | 6.6 | 26.6 | 241 | 11.8 | 66.4 | 12.4 |
| FC | 945 | 6.6 | 30.3 | 260 | 11.8 | 61.6 | 12.1 |
| IT | 659 | 6.4 | 47.3 | 368 | 11.8 | 39.9 | 10.6 |
| SC | 555 | 6.4 | 53.5 | 496 | 11.7 | 32.4 | 9.8 |
| 30° V | 419 | 6.0 | 75.5 | 1493 | 11.6 | 10.9 | 6.9 |

[a] $r$ for fundamental resonance $(M = 1)$; $\tau_1$ in femtoseconds; mode separation in percent; $|B_R/B_0|$ in percent, normalized to AT-cut, $c$-mode value.

anharmonic responses for all three modes up to $M = 5$ have been attained (T. J. Lukaszek, private communication, 1977).

## VII. Analog Electric Network Models

In the preceding section lumped parameter networks were discussed. These are used to represent resonators over relatively narrow frequency ranges. When other than traction-free boundary conditions are to be employed, as in transducers, the lumped analysis can be extended to include the new circumstances. Operation over wider frequency bands, in the time domain, or with materials having large piezoelectric coupling, requires use of more exact networks. These contain transcendental functions representing wave transmission in the vibrator. Mason's book (1948) is the classical reference for such networks; Berlincourt *et al.* (1964) have provided a valuable survey of these equivalent circuits for many kinds of vibrators.

This section describes equivalent networks of the analog type. These have the distinction of being drawn in such a fashion as to match up, on a one-to-one basis, the circuit components with the physical features they represent. This description produces a schematic that is valid in a point-to-point manner rather than merely yielding a circuit that produces the correct port-to-port immittance matrix. Matching the physical features and their electrical counterparts leads to a building-block approach that heightens understanding and simplifies the representation and analysis of more complex structures; it also facilitates the use of computer aided design (CAD) techniques.

### A. Transmission Line Equations for Waves in a Piezoelectric Crystal

Waves on a transmission line obey the Heaviside equations

$$V_{m,\zeta} = -j\omega I_m Z_m / v_m \tag{107}$$

and

$$I_{m,\zeta} = -j\omega V_m / Z_m v_m. \tag{108}$$

$V_m$ and $I_m$ are the modal voltage and current, respectively; $Z_m$ is the modal impedance; and $v_m$ is the wave velocity. Application of transmission line formalisms to acoustic wave problems has been made recently by Oliner (1969), Oliner *et al.* (1972a,b), and Auld (1973). We show here that acoustic plane waves propagating in an arbitrarily anisotropic, linear, piezoelectric

medium satisfy Eqs. (107)–(108). In Section VII,B transmission lines are incorporated into analog networks for doubly rotated thickness mode plates.

Normal coordinate transformations of displacement and stress are defined by

$$u_m^\circ = \bar{\gamma}_{mj} u_j \tag{109}$$

and

$$T_{\zeta m}^\circ = \bar{\gamma}_{mj}(\bar{\Gamma}_{jk} u_{k,\zeta} + \Xi_j \mathscr{A}). \tag{110}$$

With the help of Eqs. (17), (39), and (109), Eq. (110) becomes

$$T_{\zeta m}^\circ = \bar{c}_m u_{m,\zeta}^\circ + e_m \mathscr{A}. \tag{111}$$

The first term on the right-hand side of Eq. (111) is due to the "wavy" stress component $\tilde{T}_{\zeta m}^\circ$, while the second term is a spatial constant, arising from the piezoelectric effect, that we shall denote as $\bar{\tilde{T}}_{\zeta m}^\circ$. For the wave portion we have

$$\tilde{T}_{\zeta m}^\circ = \bar{c}_m u_{m,\zeta}^\circ. \tag{112}$$

Equation (1) is transformed into

$$\bar{\gamma}_{mj} T_{ij,i} = -\rho\omega^2 u_m^\circ. \tag{113}$$

The left-hand side of this equation is $T_{\zeta m,\zeta}^\circ$, but because $\bar{\tilde{T}}_{\zeta m,\zeta}^\circ$ vanishes within the crystal, we get finally

$$\tilde{T}_{\zeta m,\zeta}^\circ = -\rho\omega^2 u_m^\circ. \tag{114}$$

Equations (112) and (114) become isomorphic with Eqs. (107)–(108) by the definitions

$$V_m = A\tilde{T}_{\zeta m}^\circ \tag{115}$$

$$I_m = -j\omega u_m^\circ \tag{116}$$

$$Z_m = A\rho v_m \tag{117}$$

and identification of $v_m$ with Eq. (19).

## B. Equivalent Networks for Thickness Modes

Synthesis of Eq. (30), representing the electrical input admittance, begins as in Section VI,A with extraction of the static shunt capacitor $C_0$, followed by a negative $C_0$ in series. The negative capacitance results from the reactions between the driving electric field applied and the $\zeta$-directed electric fields produced by the acoustic waves. With the capacitors extracted the remainder is [cf. Eq. (91)]

$$Y_{TL} = j\omega C_0 \sum_m k_m^2 \tan X^{(m)}/X^{(m)}. \tag{118}$$

The terms in Eq. (118) are now interpreted in the light of Section VII,A as leading to transmission lines. That is, each of the admissible plane waves for a given propagation direction $\zeta$ is represented by a transmission line supporting one of the wave stresses $\tilde{T}^{\circ}_{\zeta m}$ in the bulk of the crystal. The piezoelectric driving stresses $\overline{T}^{\circ}_{\zeta m}$ come into play at the plate surfaces only. In order to have an analog network, the ideal transformers that are the circuit equivalents of the $\overline{T}^{\circ}_{\zeta m}$ must be removed to the surfaces. It has been shown that when this is done, the network that results is an exact analog of the physical workings of the plate vibrator (Ballato *et al.*, 1974).

For a single mode, the analog network is shown in Fig. 23 along with
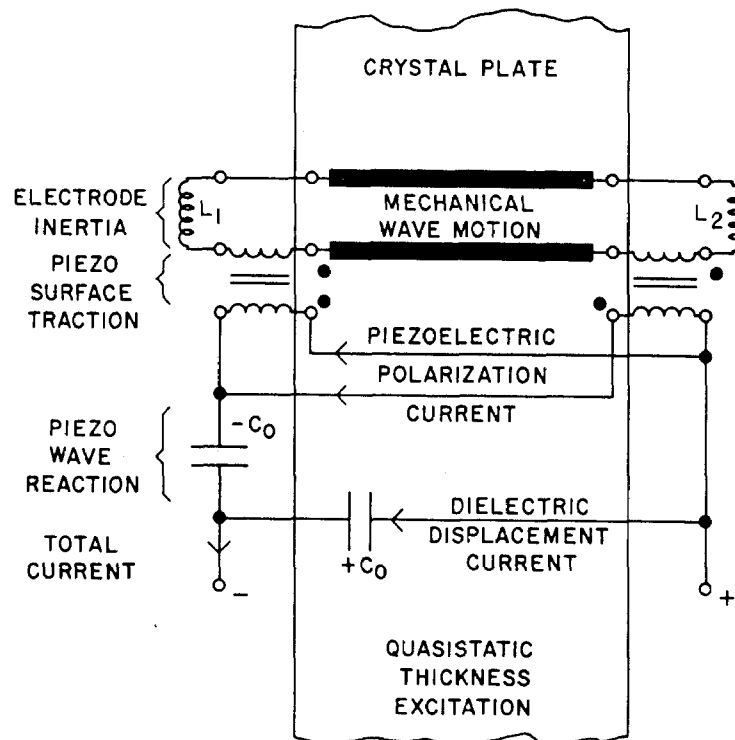


FIG. 23. Analog quasi-static exact equivalent network for a thickness mode crystal plate with one piezoelectrically excited mode. Inductors represent inertial tractions due to electrodes; transformers represent piezoelectric surface tractions driving the mode. Physical correspondences with network features are labeled.

the corresponding physical features. Lumped at the surfaces are identical piezoelectric transformers supplying $\delta$ functions of traction to drive the plate. The primaries are connected in parallel. Also located at the surfaces are the mechanical ports and the negative capacitor. In the traction-free case, the mechanical ports would be short-circuited; in Fig. 23 they have been provided with terminating inductors $L_i$ that represent mass loadings caused by electrodes. The lumped electrode masses result in $\delta$ functions of

inertial traction at the boundaries in series with the piezoelectric tractions. The inductances are of value

$$L_i = \bar{m}_i A, \tag{119}$$

where $\bar{m}_i$ is the mass per unit area on each surface. When the surface masses are equal, the schematic of Fig. 23 is mechanically symmetrical; the transmission line center is a current node, and may be bisected to yield the simplified network of Fig. 24. Figure 24 is no longer an analog circuit due to



ELECTRICAL.        BOUNDARY    ELECTRODE    BISECTED
PORT AND SHUNT      PIEZO      FILMS        CRYSTAL
CAPACITANCE        NETWORK     (LUMPED      PLATE
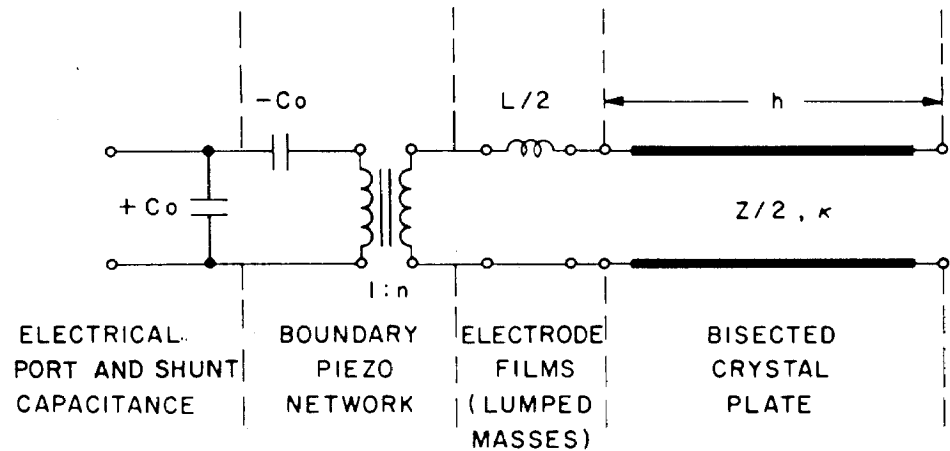                               MASSES)

FIG. 24. Bisected version of Fig. 23 for the case of equal inductors.

the bisection, but its components are interpretable in physical terms. It has a transmission line of characteristic impedance $Z/2 = A\rho v_m/2$ and propagation constant $\kappa = \omega/v_m$; the inductor is $L/2 = \bar{m}A/2 = \rho h\mu A/2$, and the turns ratio is $n = e_m A/2h$. The input admittance of Eq. (55) is exactly realized, for one mode, by Fig. 24.

In the multimode case, where two or three modes are excited, the analog network is given by an augmented version of Fig. 23. Each mode has a transmission line of length $2h$, terminated at its mechanical ports by inductors if mass loaded or by short circuits if traction-free; in series with the mechanical ports are piezoelectric transformer secondaries. The primaries of all transformers are connected in parallel and lead to the $-C_0$ and shunt capacitor $C_0$. Each transformer has a turns ratio of

$$n_m = e_m A/2h = (C_0 A\bar{c}_m k_m^2/2h)^{1/2}. \tag{120}$$

The dot convention of Fig. 23 must be maintained for all transformer pairs; this is the manifestation of the polar nature of the piezoelectric effect. As long as the impedances terminating the mechanical ports are equal in pairs, the network may be bisected to yield a network like Fig. 24 having secondary circuits in parallel. For equal lumped masses on both surfaces, this circuit realizes the electrical port admittance Eq. (55) exactly.

Any of the analog networks described above may be used for time-domain analyses in addition to the usual frequency-domain uses. When a network is analog in nature, a solution of the circuit problem evaluated at any value of the thickness coordinate gives immediately the solution of the corresponding physics problem at that point.

## C. INTERFACE NETWORK

Figure 23 and its generalization to three modes were presented in the preceding subsection simply as realizations of the electrical port input admittance of Eq. (38). In this instance the mechanical ports at the plate surfaces were shorted to satisfy traction-free boundary conditions. Termination of the mechanical ports by inductances realized the input admittance of Eq. (55), stemming from the boundary conditions of Eq. (53). The analog networks given are however capable of greater generality than the brief derivation might lead one to expect. Because there are three components of traction and of particle displacement at each surface as well as the electrical port, the complete representation of the overall electromechanical system takes the form of a seven-port network. This extended circuit equivalent is a necessary consequence of the multimode nature of doubly rotated crystal vibrators, and must, in general, be used to characterize their behavior unless the criteria of Section III,B are met.

At each surface the three mechanical ports in the equivalent network appear with the normal coordinate variables of Eqs. (109)–(110). Conversion to components referred to the crystallographic axes $X_j$ requires that the three ports of each surface be connected to a network realizing a three-dimensional orthogonal transformation (Carlin and Giordano, 1964). This network, consisting solely of interconnected ideal transformers, is shown in Fig. 25. The secondary turns ratios are the components of the coordinate transformation; switching primary and secondary ports requires only that the transposed components be substituted in the ratios. If one network of Fig. 25 is attached to the mechanical ports on each side of the normal coordinate circuit, the result is a complete analog network that exactly realizes the seven-port impedance function of the vibrator. As drawn in Fig. 25, the primary ports would be attached to the normal mode ports, and the secondary ports would then represent the coordinates $X_j$. Then the $\beta_{mj}$ appearing in the figure would be identified with the stiffened eigenvector components $\bar{\gamma}_{mj}$. For a number of reasons, such as the stacking of plates to be described in the next subsection, it is often more convenient to refer the secondary ports of Fig. 25 to a laboratory coordinate system coinciding with the plate thickness and lateral directions, rather than to the crystallographic axes. Since, by Eq. (7), the transformation to the plate axes from the crystal axes is determined by $\alpha_{ij}$, and the transformation to normal coordinates is
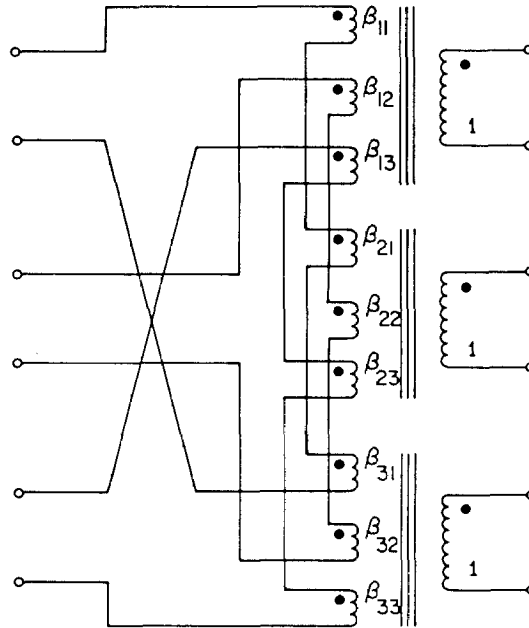
FIG. 25. Ideal transformer realization of a three-dimensional orthogonal transformation. This boundary, or interface, network converts between normal coordinates utilized within the plate and laboratory coordinates used at the surfaces for plate stacking. Turns ratios are the components of the transformation.

given by $\bar{\gamma}_{mj}$, one has

$$\beta_{mi} = \alpha_{ij}\bar{\gamma}_{mj}. \tag{121}$$

With these turns ratios the total equivalent circuit has its mechanical ports referred to the plate axes.

The network of Fig. 25 subjects immittances to similarity transformations. An impedance network, characterized by elements $Z^{\circ}_{mn}$, that is attached to the primary ports will be perceived at the secondary ports as having components

$$Z_{ij} = \beta_{mi}\beta_{nj}Z^{\circ}_{mn}. \tag{122}$$

If the impedance is of diagonal form, no transformation takes place; the inductors of Eq. (119) are thus unchanged by the boundary network, which can be discarded in this instance. The network may be simplified in other cases as well because of inherent crystal symmetry and/or propagation direction. The role of these networks for stacks of plates will be discussed in the next subsection. Boundary and interface networks for waves at nonnormal incidence in isotropic media have been determined by Oliner *et al.* (1972b). Ballato (1974) has described networks for representing the inclusion of the electromagnetic modes when the quasi-static constraint is relaxed.

## D. STACKING OF DOUBLY ROTATED PLATES

Stacking of plates is used to form composite transducers, delay lines, and filters. These devices have almost invariably been of the single mode variety (Sittig, 1972). Use of doubly rotated crystal plates in a layered configuration opens the way for an extension of these devices to include the use of more than one mode. One example of such a use is the stacked-crystal filter (SCF) which operates on the multimode principle (Ballato *et al.*, 1974). Stacking of multimode plates was described by Onoe (1972) using Mason equivalent circuits.

Use of the complete analog circuit for the multimode plate, including the interface networks, permits the description of a stack of plates in a simple manner. The interface, or boundary, networks of Fig. 25 are referred for each plate in the stack to a common laboratory reference frame. This referral amounts to, at most, an additional rotation about the common thickness direction for each network; the rotation is manifested by a change in the turns ratios $\beta_{mi}$ to account for the azimuthal angle $\psi$. Upon referring all networks to the common frame, stacking is accomplished by connecting corresponding mechanical ports together. That is, if one axis of the laboratory frame coincides with the mutual thickness coordinate of two adjacent plates, then the ports for this axis are joined, and so on. The entire stack then appears as a cascade connection of transmission line and interface networks. Simplifications arising from crystal symmetry or propagation direction that render certain of the $\beta_{mi}$ zero are directly interpretable from the circuit schematic; so too are simplifications in the piezoelectric driving terms $n_m$. All of the multimode interactions are readily traced from the analog network picture. Analytically, each plate is representable by a set of seven-port impedance relations, with stacking carried out by a matrix procedure using extended A, B, C, D parameters which are themselves matrices.

REFERENCES

Anonymous. (1949). *Proc. IRE* **37**, 1378–1395.
Auld, B. A. (1973). "Acoustic Fields and Waves in Solids," Vols. I and II. Wiley, New York.
Baldwin, C. F., and Bokovoy, S. A. (1936). U.S. Patent 2,254,866.
Ballato, A. (1960). *Proc. 14th Annu. Frequency Contr. Symp.* pp. 89–114.
Ballato, A. (1974). *Proc. Symp. Opt. & Acoust. Micro-Electron.*, pp. 599–615.
Ballato, A. (1976). *Proc. IEEE* **64**, 1449–1450.
Ballato, A., and Iafrate, G. J. (1976). *Proc. 30th Annu. Frequency Contr. Symp.* pp. 141–156.
Ballato, A., and Lukaszek, T. (1974). *IEEE Trans. Sonics Ultrason.* **21**, 269–274.
Ballato, A., and Lukaszek, T. (1975). *Proc. 29th Annu. Frequency Contr. Symp.* pp. 10–25.
Ballato, A., Bertoni, H. L., and Tamir, T. (1974). *IEEE Trans. Microwave Theory Tech.* **22**, 14–25.
Baumhauer, J. C., and Tiersten, H. F. (1973). *J. Acoust. Soc. Am.* **54**, 1017–1034.
Bechmann, R. (1951). *Arch. Elektr. Uebertr.* **5**, 89–90.

Bechmann, R. (1952). *Arch. Elektr. Uebertr.* **6**, 361–368.

Bechmann, R. (1956). *Proc. IRE* **44**, 1600–1607.

Bechmann, R. (1958). *Phys. Rev.* **110**, 1060–1061.

Bechmann, R. (1961). *Proc. IRE* **49**, 1454.

Bechmann, R., Ballato, A. D., and Lukaszek, T. J. (1962). *Proc. IRE* **50**, 1812–1822 and 2451.

Berlincourt, D. A., Curran, D. R., and Jaffe, H. (1964). *In* "Physical Acoustics: Principles and Methods" (W. P. Mason, ed.), Vol. 1, Part A, pp. 169–270. Academic Press, New York.

Besson, R. (1974). *Proc. 28th Annu. Frequency Contr. Symp.* pp. 8–13.

Birch, J., and Weston, D. A. (1976). *Proc. 30th Annu. Frequency Contr. Symp.* pp. 32–39.

Bokovoy, S. A., and Baldwin, C. F. (1935). U.K. Patent 457,342.

Bottom, V. E., and Ives, W. R. (1951). U.S. Patent 2,743,144.

Carlin, H. J., and Giordano, A. B. (1964). "Network Theory," pp. 190–207. Prentice-Hall, Englewood Cliffs, New Jersey.

Carr, P. H., and O'Connell, R. M. (1976). *Proc. 30th Annu. Frequency Contr. Symp.* pp. 129–131.

Chang, Z.-P., and Barsch, G. R. (1976). *IEEE Trans. Sonics Ultrason.* **23**, 127–135.

Christoffel, E. B. (1877). *Ann. Mat. Pura Appl.* [2] **8**, 193–243.

Détaint, J., and Lançon, R. (1976). *Proc. 30th Annu. Frequency Contr. Symp.* pp. 132–140.

Détaint, J., and Lançon, R. (1977). *Onde Electr.* **57** (in press).

EerNisse, E. P. (1975). *Proc. 29th Annu. Frequency Contr. Symp.* pp. 1–4.

EerNisse, E. P. (1976). *Proc. 30th Annu. Frequency Contr. Symp.* pp. 8–11.

Epstein, S. (1973). *Proc. 1973 Ultrason. Symp.* pp. 540–542.

Filler, R. L., and Vig, J. R. (1976). *Proc. 30th Annu. Frequency Contr. Symp.* pp. 264–268.

Franx, C. (1967). *Proc. 21st Annu. Frequency Contr. Symp.* pp. 436–454.

Fukuyo, H., Yoshie, H., and Nakazawa, M. (1967). *Bull. Tokyo Inst. Technol.* **82**, 53–64.

Gagnepain, J.-J. (1972). Doctoral Thesis, University of Besançon, France.

Gerber, E. A., and Miles, M. H. (1961). *Proc. IRE* **49**, 1650–1654.

Gerber, E. A., and Sykes, R. A. (1974). *Natl. Bur. Stand. (U.S.), Monogr.* **140**, 41–64.

Hafner, E. (1956). *Proc. 10th Annu. Frequency Contr. Symp.* pp. 182–189.

Hafner, E. (1974). *IEEE Trans. Sonics Ultrason.* **21**, 220–237.

Hammond, D. L., and Benjaminson, A. (1965). *Hewlett-Packard J.* **16**, 1–7.

Hammond, D. L., Adams, C., and Cutler, L. (1963). *Proc. 17th Annu. Frequency Contr. Symp.* pp. 215–232.

Holland, R. (1974). *Proc. 1974 Ultrason. Symp.* pp. 592–598.

Holland, R. (1976). *IEEE Trans. Sonics Ultrason.* **23**, 72–75.

Holland, R., and EerNisse, E. P. (1969). "Design of Resonant Piezoelectric Devices," MIT Press, Cambridge, Massachusetts.

Hruška, K. (1971). *IEEE Trans. Sonics Ultrason.* **18**, 1–7.

Hruška, K., and Kazda, V. (1968). *Czech. J. Phys.* **b18**, 500–503.

Jhunjhunwala, A., Vetelino, J. F., and Field, J. C. (1976). *Proc. 1976 Ultrason. Symp.* pp. 523–527.

Juretschke, H. J. (1974). "Crystal Physics." Benjamin, Reading, Massachusetts.

Koga, I. (1969). *Proc. 23rd Annu. Frequency Contr. Symp.* pp. 128–131.

Koga, I., Aruga, M., and Yoshinaka, Y. (1958). *Phys. Rev.* **109**, 1467–1473.

Kusters, J. A. (1970). *Proc. 24th Annu. Frequency Contr. Symp.* pp. 46–54.

Kusters, J. A. (1976). *IEEE Trans. Sonics Ultrason.* **23**, 273–276.

Kusters, J. A., and Leach, J. G. (1977). *Proc. IEEE* **65**, 282–284.

Lagasse, G., Ho, J., and Bloch, M. (1972). *Proc. 26th Annu. Frequency Contr. Symp.* pp. 148–151.

Lamb, J., and Richter, J. (1966). *Proc. R. Soc. London, Ser. A* **293**, 479–492.

Landolt-Börnstein (1966). "Numerical Data and Functional Relationships in Science and Technology," New Ser., Vol. III/1, pp. 40–123. Springer-Verlag, Berlin and New York.

Landolt-Börnstein (1969). "Numerical Data and Functional Relationships in Science and Technology," New Ser., Vol. III/2, pp. 40–101. Springer-Verlag, Berlin and New York.

Lawson, A. W. (1941). *Phys. Rev.* **59**, 838–839.

Lee, P. C. Y., and Haines, D. W. (1974). *In* "R. D. Mindlin and Applied Mechanics" (G. Herrmann, ed.), pp. 227–253. Pergamon, Oxford.

Lee, P. C. Y., and Syngellakis, S. (1975). *Proc. 29th Annu. Frequency Contr. Symp.* pp. 65–70.

Lee, P. C. Y., and Wu, K.-M. (1976). *Proc. 30th Annu. Frequency Contr. Symp.* pp. 1–7.

Lee, P. C. Y., Wang, Y. S., and Markenscoff, X. (1975). *J. Acoust. Soc. Am.* **57**, 95–105.

McSkimin, H. J., Andreatch, P., Jr., and Thurston, R. N. (1965). *J. Appl. Phys.* **36**, 1624–1632.

Mason, W. P. (1948). "Electromechanical Transducers and Wave Filters," 2nd ed., pp. 200–209 and 399–404. Van Nostrand-Reinhold, Princeton, New Jersey.

Mason, W. P. (1950). "Piezoelectric Crystals and Their Application to Ultrasonics," pp. 208–209. Van Nostrand-Reinhold, Princeton, New Jersey.

Mason, W. P. (1964). *In* "Physical Acoustics: Principles and Methods" (W. P. Mason, ed.), Vol. 1, Part A, pp. 335–416. Academic Press, New York.

Mindlin, R. D. (1968). *J. Acoust. Soc. Am.* **43**, 1329–1331.

Nye, J. F. (1957). "Physical Properties of Crystals." Oxford Univ. Press, London and New York.

Oliner, A. A. (1969). *IEEE Trans. Microwave Theory Tech.* **17**, 812–826.

Oliner, A. A., Bertoni, H. L., and Li, R. C. M. (1972a). *Proc. IEEE* **60**, 1503–1512.

Oliner, A. A., Li, R. C. M., and Bertoni, H. L. (1972b). *Proc. IEEE* **60**, 1513–1518.

Onoe, M. (1969). *Proc. IEEE* **57**, 702–703.

Onoe, M. (1972). *Trans. Inst. Elec. Eng. (Jpn.)* **55A**, 239–244.

Onoe, M., and Jumonji, H. (1967). *J. Acoust. Soc. Am.* **41**, 974–980.

Schulz, M. B., Matsinger, B. J., and Holland, M. G. (1970). *J. Appl. Phys.* **41**, 2755–2765.

Shockley, W., Curran, D. R., and Koneval, D. J. (1967). *J. Acoust. Soc. Am.* **41**, 981–993.

Sittig, E. K. (1972). *In* "Physical Acoustics: Principles and Methods" (W. P. Mason and R. N. Thurston, eds.), Vol. 9, pp. 221–275. Academic Press, New York.

Smith, R. T., and Welsh, F. S. (1971). *J. Appl. Phys.* **42**, 2219–2230.

Smythe, R. C. (1974). *Proc. 28th Annu. Frequency Contr. Symp.* pp. 5–7.

Spencer, W. J. (1972). *In* "Physical Acoustics: Principles and Methods" (W. P. Mason and R. N. Thurston, eds.), Vol. 9, pp. 167–220. Academic Press, New York.

Stanley, J. M. (1954). *Ind. Eng. Chem.* **32**, 1684–1689.

Syngellakis, S., and Lee, P. C. Y. (1976). *Proc. 30th Annu. Frequency Contr. Symp.* pp. 184–190.

Thurston, R. N. (1964). *In* "Physical Acoustics: Principles and Methods" (W. P. Mason, ed.), Vol. 1, Part A, pp. 1–110. Academic Press, New York.

Thurston, R. N., McSkimin, H. J., and Andreatch, P., Jr. (1966). *J. Appl. Phys.* **37**, 267–275.

Tiersten, H. F. (1963). *J. Acoust. Soc. Am.* **35**, 53–58.

Tiersten, H. F. (1969). "Linear Piezoelectric Plate Vibrations." Plenum, New York.

Tiersten, H. F. (1975a). *J. Acoust. Soc. Am.* **57**, 660–666.

Tiersten, H. F. (1975b). *J. Acoust. Soc. Am.* **57**, 667–681.

Tiersten, H. F. (1976). *J. Acoust. Soc. Am.* **59**, 866–878.

Valdois, M., Besson, J., and Gagnepain, J.-J. (1974). *Proc. 28th Annu. Frequency Contr. Symp.* pp. 19–32.

Warner, A. W. (1963). *Proc. 17th Annu. Frequency Contr. Symp.* pp. 248–266.

Warner, A. W., Onoe, M., and Coquin, G. A. (1967). *J. Acoust. Soc. Am.* **42**, 1223–1231.

Weinert, R. W., and Isaacs, T. J. (1975). *Proc. 29th Annu. Frequency Contr. Symp.* pp. 139–142.

Wood, A. F. B., and Seed, A. (1967). *Proc. 21st Annu. Frequency Contr. Symp.* pp. 420–435.

Yamada, T., and Niizeki, N. (1970). *Proc. IEEE* **58**, 941–942.

Zelenka, J., and Lee, P. C. Y. (1971). *IEEE Trans. Sonics Ultrason.* **18**, 79–80.